Atomic Layer Deposition of Platinum Particles, Titanium Oxide Films, and Alkoxysilane Surface Layers

by

Virginia Rose Anderson

B.A., Willamette University, Oregon, 2003

M.S., Dartmouth University, New Hampshire, 2007

A thesis submitted to the

Faculty of the Graduate School of the

University of Colorado in partial fulfillment

of the requirements for the degree of

Doctor of Philosophy

Department of Chemistry and Biochemistry

2014

This thesis entitled:
Atomic Layer Deposition of Platinum Particles, Titanium Oxide Films, and Alkoxysilane Surface Layers
written by Virginia Rose Anderson
has been approved for the Department of Chemistry and Biochemistry

_____

Prof. Steven M George

_____

Prof. Cortlandt Pierpont

Date _____

The final copy of this thesis has been examined by the signatories, and we find that both the content and the form meet acceptable presentation standards of scholarly work in the above mentioned discipline.

Virginia Rose Anderson, (Ph.D., Chemistry)

Atomic Layer Deposition of Platinum Particles, Titanium Oxide Films, and Alkoxysilane Surface Layers

Thesis directed by Prof. Steven M George

Atomic Layer Deposition (ALD) is a an excellent technique for depositing conformal thin films on complex geometries in layer by layer fashion. The mechanisms of depositing TiO_2, platinum, and ethoxysilane molecules were probed with *in situ* Fourier transform infrared (FTIR) in order to better understand and improve the process. Each of these studies involves TiO_2.

There are many uses for thin films of titanium dioxide, a semiconductor and high dielectric material. Current Atomic Layer Deposition (ALD) of TiO_2 generally involves water or ozone, which can oxidize and corrode some substrates of interest. Ritala et al. successfully deposited an assortment of metal oxides using no water, but instead, metal alkoxides and metal halides as precursors.[1] Presented is a study of ALD of titanium dioxide using titanium tetrachloride ($TiCl_4$) and titanium tetraisopropoxide (TTIP). In situ Fourier transform infrared (FTIR) studies revealed that the mechanism for TiO_2 ALD using titanium tetrachloride and titanium tetraisopropoxide changed with temperature. At temperatures between 250 and 300 °C, the isopropoxide species after TTIP exposures quickly underwent β-hydride elimination to produce TiOH species on the surface. The observation of propene by quadrupole mass spectrometry supported the β-hydride elimination reaction pathway. Deposition was investigated between 150 and 300 °C on substrates including zirconia, alumina, and silica. Quartz crystal microbalance results and X-ray reflectivity showed that the system grew 0.5-0.6 Å/cycle at 250 °C. X-Ray photoelectron studies also confirmed TiO_2 film growth.

In another aspect of ALD use, self-limiting chemistry assisted with terminating a surface with alkoxysilanes. Tire rubber contains additives such as carbon black or silica particles to provide strength. Although in theory Kevlar fibers would provide strength while lowering the density and

increasing car fuel efficiency, in practice Kevlar fibers disperse only very poorly in the rubber, leading to inhomogeneity. In order the increase the mixing likelihood between rubber and Kevlar, the reactions of some sulfurous siloxanes were examined on both aluminum oxide and titanium oxide. The titanium oxide adhesion layer allowed the deposition of molecules on the surface that looked promising for improving mixing with rubber and decreasing the weight of tires.

Atomic layer deposition offers the possibility of more precision in platinum deposition. In a platinum deposition study, the nucleation and growth of non-conformal platinum on TiO_2 and WO_x powder using $Pt(hfac)_2$ and formalin was examined with in-situ FTIR and transmission electron microscopy (TEM). Interest in substitution of Pt/C as the oxidation reduction reaction catalyst in polymer electrolyte membrane fuel cells (PEMFCs) led to the ALD synthesis of Pt/WO_x and Pt/TiO_2. A nucleation period on the order of 100 cycles was observed, after which, platinum loading and particle size measurably increased with increasing cycle number. The adsorption of the hfac ligand on the metal oxide substrate effectively inhibits nanoparticle coalescence during the growth phase, which led to further investigation of its use as a site-blocking agent. The results showed that Pt particle distance could be increased with the use of hfacH.

Dedication

To inspiring teachers, especially Michael Russell, Casey Hynes, and Raymond Mitchell

Acknowledgements

The George group, family and friends

Contents

Chapter

Tables

Table

Figures

Figure

Chapter 1

Introduction

Curiosity is one of the enduring motives for carrying out research of any kind, and is also one of the enduring forces of human nature. With the necessities of life mostly taken care of in modern, industrialized locations, most of us have a lot of time to ponder why we do what we do. The unsustainable way we are using chemicals will lead to a change in how we live, and some thought is going into how to decrease rare and finite resource consumption.

The current ease of publishing, among other things, means that ideas are being shared among acquaintances and strangers, with the usual problems in comprehension and persuasion between people. Data collection and interpretation remain as important as they have ever been, and recording and giving context to the information are still done with the hope that, given accurate information, someone will put together a more complete picture of the universe. In each of these studies we sought to modify current technology to use less precious mineral, or less fuel oil, and to learn something about the nature of reactions between certain molecules so that we better use them.

The three experimental systems described here encompass a fuel cell catalyst motivated study of platinum, a modification of polymer surface chemistry using sulfurous molecules for changing polymer-rubber interaction, and a look at surface chemical species during a waterless thin film deposition of titanium dioxide. All of them used a technique, atomic layer deposition, that has been relying on the expansion in understanding of low pressure technology. As we have learned ways to probe smaller materials, we have been finding ways to control the size and purity of many of them. It is well known that properties are determined by composition and structure, and by shape

and dimensions once below a threshold size. Metal conductivity, for example, stays constant over a wide range of sizes, but there is a lower limit below which that is no longer true. Light absorptivity, for another example, remains a material constant until some lower size limit is reached.

Vacuum techniques allow control of material composition, because their handling or formation can take place under chemically clean conditions. High vacuum surface studies have helped along the understanding of fundamental atomic and molecular interaction, and led to knowledge of how best to deposit films with the desired properties for their given application. Solution methods, such as electrodeposition and dip-coating, can also produce highly pure thin films, although for some systems the dense solution bath of interacting species sometimes causes contamination.

Physical vapor deposition is frequently used to deposit nanometer to micron thick films, and is usually done at medium vacuum pressures. Often done using plasma excited ions, sputtering involves striking a target material and causing it to leave the surface and coat the desired substrate (and whatever else is in the deposition range, which depends on ion energy). The background pressure is the primary determinant of deposition purity because the target material is typically very high grade. Although any ion transfer of kinetic energy to the target is considered sputtering, argon ions from plasma are the common source. The process conditions and their affect on the film thickness and quality are well understood, and the rate of material growth is rapid, but the line of sight propensity of the technique typically excludes applications with complex geometries.

A number of thin film growth methods in vacuum exist, including the already mentioned sputtering procedure. In addition, vacuum capability makes it practical to carry out evaporation, chemical vapor deposition, molecular beam epitaxy, and atomic layer deposition. Atomic Layer Deposition as an outgrowth of molecular beam epitaxy was published in the 1970s and was called atomic layer evaporation or epitaxy.[3] Finnish researchers led by Suntola in the 1970s, and Russian researchers led by Aleskovskii in the 1960s are the earliest known ALD developers. Atomic layer deposition (ALD) is a step-by-step process whereby chemicals in the gas phase are introduced one at a time to a substrate, and designed so that each species reacts to completion with the surface leading to a self-limiting process, in contrast to Chemical Vapor Deposition (CVD), which does not use

reactant separation. The purging step between each precursor sweeps by-products and unused reactants from the sample so they do not influence the next reaction. Though the process is typically slower than chemical vapor deposition, the advantages include very fine control of film thickness, conformal coverage, and the ability to coat rough, trenched topographies, and other high aspect ratio surfaces smoothly. The sequence can be seen to happen via cycles. After one two-step, AB cycle, the surface has returned to its initial coverage state. The gas phase technique uses self-limiting surface reactions to deposit a material onto a substrate with angstrom level precision and with little post-processing. ALD can coat 3D substrate geometries, like powders, that are otherwise challenging with other methods.[4]

At the present state of this technique, efforts are underway to lower the price of fabrication tool production and operation, and the semiconductor industry relies on ALD. For some products, it is the only known way to achieve the necessary material quality and dimensions. Central processing units and micro and nanoelectronic devices incorporate ALD. Because it can provide an invisible barrier to tarnishing, some jewelry makers now coat their silver with ALD layers, and much work is ongoing to improve packaging for corrosion sensitive material by making very thin but efficient barrier layers. Efforts are also ongoing to both extend the materials options by finding new recipes, and to make the technology easy to integrate with other processes.

The focus of this thesis is on the materials side, and especially in terms of optimizing deposition conditions for recipes by understanding the mechanism. During the deposition, the bond formation and breaking was probed with transmission FTIR. Previous and current groups carrying out IR studies for *in situ* film deposition include Agarwal, Chabal, and others, and encompass transmission FTIR as in this thesis, as well as attenuated total internal reflectance ATR.[5, 6, 7]

Findings for each system include a temperature window for controlled deposition, and knowledge of the exposures needed for saturation. For many ALD chemistries, the lower temperature limit of controlled growth is dictated by the condensation of the precursors, which leads to uncontrolled growth, or by a bond breaking kinetic barrier that requires some thermal energy to happen in a reasonable time. The cause of the upper temperature bound typically comes from either precursor

breakdown, and therefore non-self-limiting reaction behavior, or surface residence time, since in several surface reactions the gas phase reactant is weakly attached (physisorbed) to the surface, moves around, finds the reaction site, and reacts. Too high a temperature can cause low reaction rates since there are not enough molecules on the surface, as the equilibrium is skewed too heavily towards desorption. Looking carefully for the saturation exposure accomplishes both a check on the self-limiting nature of the chemistry, and informs the efficient use of precursor. A characteristic saturation curve shows the greatest gains in surface reactions when the open sites are the most numerous, since as sites are filled the ease of reaction with nearby sites is almost always reduced. In some cases the changing environment encourages nearby reactions, but the steric effect of having any obstruction interfering with reaching the space is usually the dominant influence. As the number of sites decrease, there is also a smaller chance for the incoming flux of reactants to find them, and when almost all sites are already reacted, the returns on dosing diminish appreciably.

The previously cited Puurunen review[4] noted that the current trend shows increasing ALD journal article publications with year. Atomic layer deposition becomes a better and more useful tool as the chemistry and engineering understanding of the options grows.

Chapter 2

Experimental methods

2.1 Fourier transform infrared

Infrared absorption occurs during transitions between molecular vibrational levels. The nuclei of two or more atoms moving relative to each other with no net translation creates a moving dipole, and the interaction of the moving dipole with electromagnetic radiation takes place in the infrared region. The frequency of the vibration depends on the force between the nuclei, as well as the mass of each. The potential curve between two nuclei must be asymmetric, because there is a limit to how close the nuclei may get, but they may get an infinite distance apart. Although the exact mathematical solution of the forces in molecules with more than two bodies are beyond current achievable exact solutions, the approximate solutions allow relatively uncomplicated theoretical predictive treatments. In the majority of cases, based on the relative velocity of each, the Born-Oppenheimer approximation holds, in which the electrons adjust rapidly to fixed nuclear positions and can be solved for separately. Morse potential approximations of the internuclear distance versus the potential energy curve reproduces the general shape of the potential well, and the resulting frequency expressions can be truncated at the desired level of corrective terms. For a potential between two nuclei, the general potential energy expression in terms of potential well depth De, the bond force constant k, the internuclear distance R, and the equilibrium internuclear distance Re:

$$E(R) = D_e[1 - e^{-\sqrt{\frac{k}{2D_e}}(R-R_e)}]^2 \tag{2.1}$$

giving solutions similar to the harmonic oscillator at the lower energy levels, and decreasing the separation between levels as the quanta increase. Above the energy height of the tailing edge of the well, any energy is permissible, and the equation no longer is needed because by then the nuclei are not bound to each other. The fundamental vibration frequencies are of interest in these studies, the transition primarily being from level zero to one, and not involving overtones or transitions from higher levels. The overtone transition frequencies in most cases require higher sensitivity than a standard set-up gives, and are not reported in the following spectra in this research.

The Fourier Transform method saves time, and in our instrument leads to replacing a monochrometer with a Michelson interferometer. The broadband infrared source is split, with one half of the beam reflected off of a fixed position mirror, and other half reflected off of a moving mirror whose position is known precisely. The beams are recombined and sent to the infrared detector. The interferogram produced can be deconvoluted into each frequency involved using a Fourier transform, with the needed time and distance information provided by the moving mirror. When passed through a sample, any absorbance is then detectable. By making use of high surface area samples, the transmission mode FTIR beam would encounter a lot of surface, and even sub monolayer amounts of precursor saturation could be seen with reasonable signal to noise (depending, of course, on the absorbing cross-section of the functionality).

2.2 Transmission electron microscopy

Transmission electron microscope images taken in the platinum chapter were of nanopowder samples with and without deposition. Energetic electrons transmitted through a material show contrast depending on the electron density and therefore the scatter. For standard TEM accelerating voltages of 50-200 kV, samples above 100 nm thick are typically opaque, and the denser the sample is, the thinner it needs to be to transmit appreciable numbers of electrons. In the following experiments, examinations of substrate powder with ALD material on the surface gave information on the results of the deposition process. In the highest resolution pictures, with the highest accelerating volages, the platinum looks very dark unless it is very thin.

2.3 X-ray reflectivity

X-ray reflectivity gives information on smooth thin film density, thickness, and roughness. Film thickness is often determined ex situ with XRR on flat samples when determining growth rates. Whether light reflects at an interface, or light reflects and absorbs, depends on the index of refraction, (n), of the materials at the interface, and on the angle of incidence (θ) according to Snell-Descartes law

$$\frac{\sin\theta_1}{\sin\theta_2} = \frac{n_2}{n_1} \tag{2.2}$$

. The angle at which the reflection goes from total to partial therefore depends on the electron density. Checking the intensity of reflected light at small angles gives therefore the mass density, if the composition of the film is known, since then electron density can be converted to mass density. The index of refraction at X-ray frequencies for metal oxides are lower than one, and the critical angles stay below one degree. Once past the critical angle, the X-rays reflect and absorb at each interface where the refractive index changes, and the reflections interfere depending on the film thickness according to Bragg's law. Film surface roughness causes X-ray scattering, and lowers the reflectance. In addition, roughness means that the film is not a single thickness, and with too high a roughness, the interference pattern cannot be read as corresponding to any thickness. Most films become difficult to model with confidence if the root-mean-square of the roughness exceeds 5 nm because the XRR used in the studies in the subsequent chapters had a 0.154 nm wavelength.

2.4 Quadrupole mass spectrometry

Oftentimes the identity of gas phase chemical species can be inferred from the data collected by a mass spectrometer. Once molecules are ionized and sometimes fragmented, they are separated in the quadrupole region according to their mass to charge ratios. When the fragments of molecules of interest overlapped, the ratios of characteristic fragments assisted in distinguishing each species.

Chapter 3

The Atomic Layer Deposition of Titanium Dioxide using Titanium Tetrachloride and Titanium Tetraisopropoxide

3.1 Introduction

Many applications require protection layers, and in some cases from mechanical wearing, and in others from atmospheric exposure.[8, 9, 10] A current magnetic memory material under study, for example, is a CoPtCr system with SiO_2 added to refine the grain boundaries and shrink disk space.[11] Magnetic materials tend to damage easily, both through oxidative and reductive degradation, and currently memory protection comes from a layer of amorphous carbon, deposited using sputtering or an ion beam.[12] This protective overcoat, however, limits the amount of size reduction that can take place in magnetic memory devices; below 5 nm the corrosion protection becomes ineffective, and this restricts the readability of dense grained devices. The smaller the grain size, the closer the magnetic reader needs to approach the grains to access their stored information. Here the examination of atomic layer deposition of a metal oxide, TiO_2, with non-corrosive chemistry is undertaken with aim towards replacing the amorphous carbon. Since the work was carried out, recent research on silicon oxynitrides look promising, being able to reduce the layer size to less than 3 nm.

Typically, metal oxides deposit easily using ALD, but in some cases there is a constraint: the use of strong oxidants would cause the destruction of the sensitive substrate material we are trying to coat. Because many surfaces degrade upon exposure to water, including many industrially useful metal nitrides and pure metals, a water free method to grow titanium dioxide would widen the

potential applicability of TiO_2 ALD. In this paper the mechanism of a water-free titanium dioxide deposition is explored.

Water is usually the oxygen source of choice, being inexpensive and non-toxic, but it can degrade surfaces sensitive to oxidation and corrosion, and increase defects at the interface.[13] The first reported TiO_2 ALD chemistry utilized $TiCl_4$ and H_2O.[14] Other titanium precursors can be used together with H_2O, including titanium-tetraisopropoxide (TTIP) and tetrakis-dimethyl-amido titanium (TDMAT).[15, 16] Alternatives such as ozone and oxygen plasma react even more strongly.[17, 6] These other oxidants have been used in systems such as TTIP and hydrogen peroxide,[18] ozone and TTIP,[6, 19] and TDMAT[20] and Cp*Ti$(OMe)_3$, making up some of the successful TiO_2 chemistries.[21] Plasma-enhanced TiO_2 ALD has also been accomplished using an O_2 plasma together with a variety of titanium precursors.[22] Other TiO_2 ALD processes have avoided forming hydroxyl groups by employing $TiCI_4$ and O_2.[23] As stated, these typical precursors used during TiO_2 ALD can also oxidize the starting substrate. This oxidation can degrade the performance of the device fabricated using the TiO_2 ALD film. For example, oxygen precursors can oxidize and corrode cobalt in magnetic media.[8, 9] Overcoats that are continuous, pinhole-free and highly resistive are required to protect cobalt from corrosion by O_2 and H_2O. Oxygen precursors can also oxidize semiconductor substrates and form a native oxide.[24, 25] This can be detrimental to the performance of the substrate. Inspired by sol-gel chemistry as a guide to possible atomic layer deposition (ALD) systems, Ritala et al. deposited several metal oxide systems using metal halides and metal alkoxides as precursors, with the alkoxides serving as the oxygen source.[1] These are expected to be less corrosive to substrates than the aforementioned ALD oxygen sources.[13]

One approach to avoid using H_2O or other strongly oxidative precursors employs a metal halide together with a metal alkoxide.[26] The oxygen is derived from the metal alkoxide, and alkyl halide elimination produces metal oxide growth. This strategy was originally developed in sol-gel chemistry.[27] This chemistry was then applied for thin film growth using ALD.[28] Waterless processes using this strategy have been developed for the ALD of a variety of oxides including Al_2O_3,[28, 1] Ta_2O_5,[28, 1, 29] hafnium silicate,[30] zirconium silicate[28, 31] and zirconium

titanate.[28, 32, 1, 33] Alkyl halide elimination from the reaction of $TiCl_4$ and TTIP has been previously used to deposit TiO_2. The sol-gel reaction between TiCl4 and TTIP in anhydrous chloroform has been employed to deposit TiO_2 thin films.[33] This chemistry has been used to modify powdered mesoporous silica materials.[34] There have also been reports of using $TiCl_4$ and TTIP for TiO_2 ALD. We discussed the use of $TiCl_4$ and TTIP for TiO_2 ALD at the AVS International Symposium in 2010.[35] A recent study has also demonstrated TiO_2 ALD using $TiCl_4$ and TTIP.[36] In this paper, in situ transmission Fourier transform infrared (FTIR) was employed to investigate the details of TiO_2 ALD using $TiCl_4$ and TTIP. The transmission FTIR experiments were performed on high surface area particle samples that yielded vibrational spectrum with high signal-to-noise. The transmission FTIR experiments were able to distinguish the reaction regimes for waterless TiO_2 ALD at low and high temperature. In addition, the TiO_2 ALD growth rates were determined using quartz crystal microbalance (QCM) measurements and x-ray reflectivity (XRR) studies. The level of chlorine impurities in the TiO_2 ALD films was also determined using x-ray photoelectron spectroscopy (XPS) depth-profiling measurements. Using atomic layer deposition (ALD), it is possible to deposit material in a smooth, thin, defect free manner, making the technique useful for many applications.[37, 38, 39, 40] Titanium dioxide makes sense as a candidate for serving as a protecting layer, since it is stable and inexpensive.[41, 42, 43, 44, 45] The tendency of pure TiO2 to crystallize when heated could be suppressed, depending on the application. Polycrystalline films could allow leakage current in dielectric situations, but could serve well as catalytic materal. Ritala looked at the deposition of titanium zirconium oxide using zirconium chloride and titanium tetraisopropoxide as precursors, with mass spectrometry and quartz crystal microbalance (QCM).[33]

3.2 Experimental Methods

Fourier Transform Infrared spectroscopy (FTIR) and mass spectrometry experiments were conducted in a viscous flow, warm wall reactor chamber that has been described previously.[46] Precursors were entrained in a flow of nitrogen gas (Airgas UHP grade) and dosed into the re-

actor holding the reactive surface, nanoparticles, in a sample grid. Using two URS-40 mass flow controllers, the nitrogen flow was kept at 1.25 Torr, a flow of 210 sccm. The sample grid was made using a tungsten mesh with 100 holes per inch, and the zirconium oxide (Sigma-Aldrich less than 50 nm diameter) or silicon oxide (Aldrich 7 nm diameter) powders were mechanically pressed in. Using powder gives high surface area, 37.7 meter^2/gram for the zirconia, increasing the FTIR signal to noise considerably compared to a flat sample.

The walls of the reactor were kept at 130 °C, and the grid could be heated to 600 °C using a Love Controls 16A temperature controller. A type K thermocouple was used to sense the temperature, and the resistive heating current was supplied by a Hewlett-Packard 6268B Power supply.

The TiO_2 was grown on silica, zirconia, and ALD alumina on zirconia. The results shown for the FTIR and mass spectrometry sections were done on ALD alumina, for the sake of consistency. The exception is that the TiO_2 in figure 11 was deposited on a silica substrate, since the silica substrate modes interfere less with the lower TiO_2 vibrational modes than either zirconia or alumina. The substrate particles were loaded into the reactor, allowed equilibration time, and flashed briefly to high temperature (500 °C for zirconia, 350 °C for silica) to remove adventitious carbon. Water was then dosed into the reactor to rehydroxylate the surface. The ALD of alumina has been very well characterized, and therefore pre-coating the experimental substrates with alumina should produce very reproducible surfaces. In these experiments, alumina was grown at 175 °C using trimethyl aluminum (97 % pure TMA Sigma-Aldrich) and water (deionized and freeze pump thawed). From previous work, it has been seen that the procedure used here gives a growth rate of 1.2 ångstroms per cycle. The reactor was constantly pumped with an Alcatel 2010 C1 mechanical pump, with the exception of static dosing periods involving mass spectrometry. The waste stream gas was monitored with an MKS baratron. A leak valve could be opened to bleed waste gases into a chamber below the reactor where a quadrupole mass spectrometer system (Stanford Research System Residual Gas Analyzer 200) was used to detect the gases flowing out of the reactor. A Pfeiffer turbo pump maintained the lower chamber at pressures below 5 x 10^{-6} Torr and was backed with a mechanical Alcatel 2005 pump.

The FTIR used was the Nicolet model Magna IR 560. The beam passed through CsI windows that were protected from chemical exposure within the reactor by MDC gate valves during dosing. That way deposition/condensation on the windows was avoided. Precursors were dosed using Labview, allowing consistently timed openings of pneumatic valves. The detector was a mercury cadmium telluride (MCT-B) Nicolet semiconductor that was cooled to 77 K with liquid nitrogen before experimentation began. The experimental FTIR set-up has been described previously (Goldstein)[46], and a schematic of the reactor is shown below in Figure 3.1.

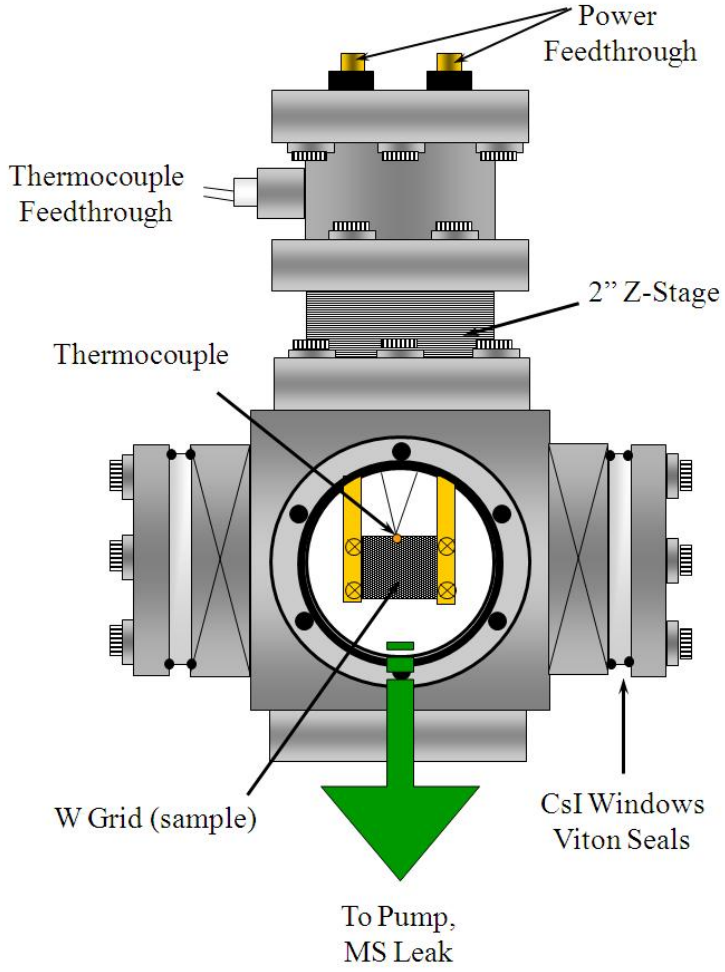

Figure 3.1: Schematic of the FTIR reactor, showing that the IR beam passes through the reactor, allowing sample scans while maintaining vacuum. This figure is modified from a Goldstein et al. paper.[2]

The precursors used for the TiO_2 deposition were titanium tetrachloride (99.8 % $TiCl_4$ from Strem Chemicals Inc.), and titanium tetraisopropoxide (99.999 % ttip from Sigma-Aldrich). Both were transferred to dosing vessels under nitrogen flow, and before the quartz crystal microbalance experiments they were freeze-pump-thawed. In order to ensure appreciable vapor pressure, titanium (IV) isopropoxide was heated to 50-70 °C during the experiments, while $TiCl_4$ was maintained at room temperature. The quartz crystal microbalance (QCM) experiments were performed in a seperate viscous flow reactor using similar dosing principles. The quartz crystal microbalance (QCM) is a technique for measuring relative mass changes in real time during ALD. In this work, QCM measurements were performed in hot walled flow type reactor described previously.[47] The stainless steel reactor tube held either the QCM or silicon wafer samples. The reactor and samples were all maintained at the reaction temperature (hot-wall reactor) with a Eurotherm control. The TM-400 thin film deposition monitor (Inficon/Maxtek, U.S.A.) was used to convert the frequency signal (Hz) from quartz crystal to mass units (ng/cm^2). The TM-400 has a mass resolution of 0.375 ng/cm^2. The gold sputtered, polished, QCM crystals supplied by Colorado Crystal Corp. (U.S.A.) were used in the experiments to minimize the effect of surface roughness. Base pressure in the reactor was maintained at 0.870 Torr using UHP nitrogen gas. Titanium oxide films were deposited on 1x1 inch precut silicon wafers. Prior to deposition substrates were cleaned in a sonicator using acetone and isopropanol. The substrates were allowed to degas in the chamber for at least 30 minutes before deposition. As with the FTIR samples, clean deposition surface substrates were ensured by coating the silicon with cycles of alumina using trimethylaluminum and water chemistry prior to TTIP/$TiCl_4$ deposition. X-ray reflectivity (XRR) measurements were taken with a Bede Scientific D1 X-ray diffractometer with a Cu X-ray source. The Cu $K\alpha$ beam was monochromated to allow only the $K\alpha 1$ radiation at 1.540 Å. The filament current was 40 mA and 40 kV. X-ray photoelectron spectra (XPS) were taken with a PHI 5600 X-ray photoelectron spectrometer using a monochromatic Al $K\alpha$ source. The depth profile was carried out using argon sputtering. Atomic force microscopy (AFM) images were taken with a Park Thermo system in non-contact mode.

3.3 Results and Discussion

3.3.1 *in situ* FTIR characterization of surface changes

The TiO_2 ALD cycles were carried out on thin film ALD Al_2O_3 on ZrO_2 particles.[48] The expected surface species for the reactions guide the interpretation of the resulting spectra, and include titanium chloride bonds after the $TiCl_4$ exposure, and isopropoxide bonds after TTIP exposure, and both exposures together make up the two halves of the ALD cycle. There exists a possibility of chlorine and carbon impurities if the reactions did not go as expected, or did not go to completion. Figures 3.2 and 3.3 show expected the expected chemistry. When $TiCl_4$ encounters a TTIP terminated surface, as in Figure 3.2, the oxygen of the isopropoxide group could attach to the incoming titanium center of the $TiCl_4$, and start the transfer of the chloride to the carbon on the isopropoxide as an oxygen replacement, forming the volatile 2-chloropropane.

In Figure 3.3, the TTIP exposure to the chloride terminated surface would be expected to lead to incoming isopropoxide oxygen attraction to the surface titanium centers, and the formation of 2-chloropropane as a gaseous by-product, which would be pumped away. The FTIR examination revealed that temperature changes caused changes in the species detected on the surface. Deposition temperatures ranged from 125 to 300 °C, and we start here by examining the reaction at 150 °C. An FTIR examination of the vibrational modes on the surface before and after reaction at 150 °C is shown in figure 3.4. The starting surface was hydroxylated alumina, and the reaction of $TiCl_4$ with hydroxyls produces a $TiCl_x$ terminated surface, with HCl as a reaction by-product, shown in Reaction 1. Figures 3.4, and 3.5 show the FTIR scans taken at 150 °C, presented in different ways to emphasize certain features. The spectrum is shown as absorbance, and the peaks between 3400 and 3750 cm-1 are due to the hydroxyl groups.[49] In the difference spectra negative features illustrate chemical features that were removed. There are groups of hydroxyls that are hydrogen bonded with one another, and these are at 3400-3600 cm^{-1}, whereas free hydroxyl groups show up at a narrower frequency range and are in the 3700 cm^{-1} region. As expected, surface hydroxyls (3730 cm^{-1}) on aluminum oxide were removed upon exposure to $TiCl_4$. The $TiCl_4$ spectra

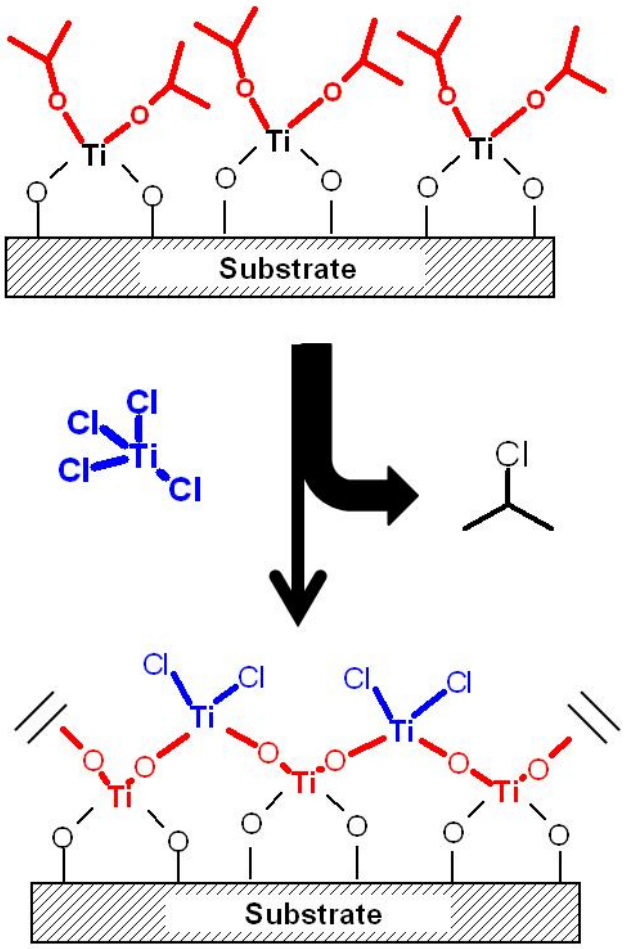

Figure 3.2: Starting with a TTIP terminated surface, $TiCl_4$ reacts to leave Ti-Cl bonds, replacing the Ti-$OCH(CH_3)_2$ bonds.

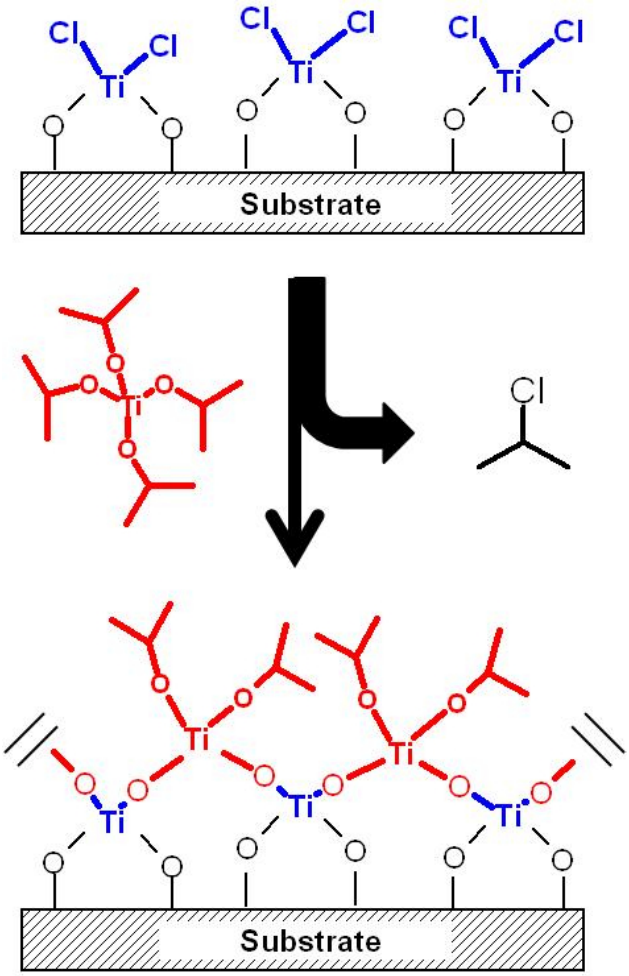

Figure 3.3: Starting with a $TiCl_x$ terminated surface, TTIP reacts to leave Ti-$OCH(CH_3)_2$ bonds, and again producing 2-chloropropane as the by-product.

shown in Figure 3.4 is otherwise relatively free of features. This would be the case if the titanium is bonded to the surface oxygen, since Ti-Cl vibrational modes are lower in frequency than observable in this experiment. A small amount of chlorines are expected to remain bonded to the titanium, with the rest leaving in the form of the reaction byproduct, hydrochloric acid. The loss of the primarily free hydroxyls indicates that a chemical change is occurring, presumably according to reaction 1, shown below.

$$\text{-OH} + TiCl_4(g) \rightarrow \text{-OTi}Cl_3 + HCl(g)$$

Reaction 1. The asterisks mark the species attached to the surface. The $TiCl_4$ was dosed onto a hydroxyl terminated surface, so the hydroxyl groups are available for reaction. One titanium atom could bond to one or more oxygens, and the number of chlorides still attached to the titanium would be four minus the newly attached oxygen(s), since titanium would still have four bonds total. The byproduct, hydrochloric acid, is volatile and easily pumped out of the reactor.

In the TTIP spectra, the TiClx terminated surface was exposed to TTIP, and new features appear that are assigned to C-H stretches (2850-3000 cm^{-1}) CH_X bend (1300-1480 cm^{-1}), and C-O stretching (strong peaks at 1020 and 1130 cm^{-1} for symmetric and antisymmetric modes). Peak assignments are based on the work of Rai and Moran.[50, 51] These features are consistent with isopropoxide groups, which are expected to be on the surface, as can be seen in reaction 2.

$$\text{-OTiCl} + Ti(OCH(CH_3)_2)_4 \rightarrow \text{-OTiOTi}((OCH(CH_3)_2)_3 + ClCH(CH_3)_2$$

Reaction 2. The asterisks mark the species attached to the surface. The $Ti(OCH(CH_3)_2)_4$ (TTIP) was dosed onto a $TiCl_4$ terminated surface, so titanium chloride groups are available for reaction. The oxygen of the isopropoxide ligand could replace the chloride of the surface species, leaving a titanium-oxygen-titanium series terminated by isopropoxide group(s). The replacement

of titanium chloride with titanium oxygen bonds is an enthalpically favorable process. The volatile byproduct, 2-chloropropane, is also easily pumped out of the reactor.

$$\text{-OTiO(CH(CH}_3)_2 + \text{TiCl}_4 \rightarrow \text{-OTiOTiCl} + \text{ClCH(CH}_3)_2$$

Reaction 3. The asterisks mark the species attached to the surface. The $TiCl_4$ was dosed onto a $Ti(OCH(CH_3)_2)_4$ (TTIP) terminated surface. The oxygen of the isopropoxide ligand could replace the chloride of the incoming precursor, leaving a titanium-oxygen-titanium series terminated by chloride(s). The volatile byproduct, 2-chloropropane, is again easily pumped out of the reactor.

It appears that the $TiCl_4$ does not completely remove the C-H and C-O features of TTIP, which could mean that some surface isoproxide remains unreacted. The reaction efficiency could be low at 150 °C, since there is expected to be a reaction barrier, and there could also be some sites that are sterically hindered from nearby isopropoxide surface species. Difference spectra of the half cycles at 150 °C are used to make the peaks more obvious.

The spectra in Figure 3.4 were taken after alumina had been exposed to 2 cycles of $TiCl_4$ and TTIP at 150 °C. The ALD alumina surface spectrum (a) is referenced back to the zirconia substrate, so that the bulk zirconium oxide stretches are not visible. Difference spectra here highlight changes, since the spectrum subtracted off allows only the chemical bonds added afterwards to be seen, showing any gains as positive absorbance features, and losses as negative absorbance features.

Figure 3.4 displays the FTIR spectra after the $TiCl_4$ and TTIP exposures for the first two TiO_2 ALD cycles on the Al_2O_3 ALD-coated ZrO_2 particles at 150 °C. Other than spectrum (a), each FTIR spectra was referenced to the starting Al_2O_3 ALD surface. Clear differences can be seen between the $TiCl_4$ saturated surface, and the TTIP saturated surface. Spectrum (b) shows the loss of hydroxyl species at 3750 cm^{-1} after the first $TiCl_4$ exposure. This loss is consistent with the reaction of $TiCl_4$ with the Al-OH species on the initial Al_2O_3 ALD surface. These Al-OH species

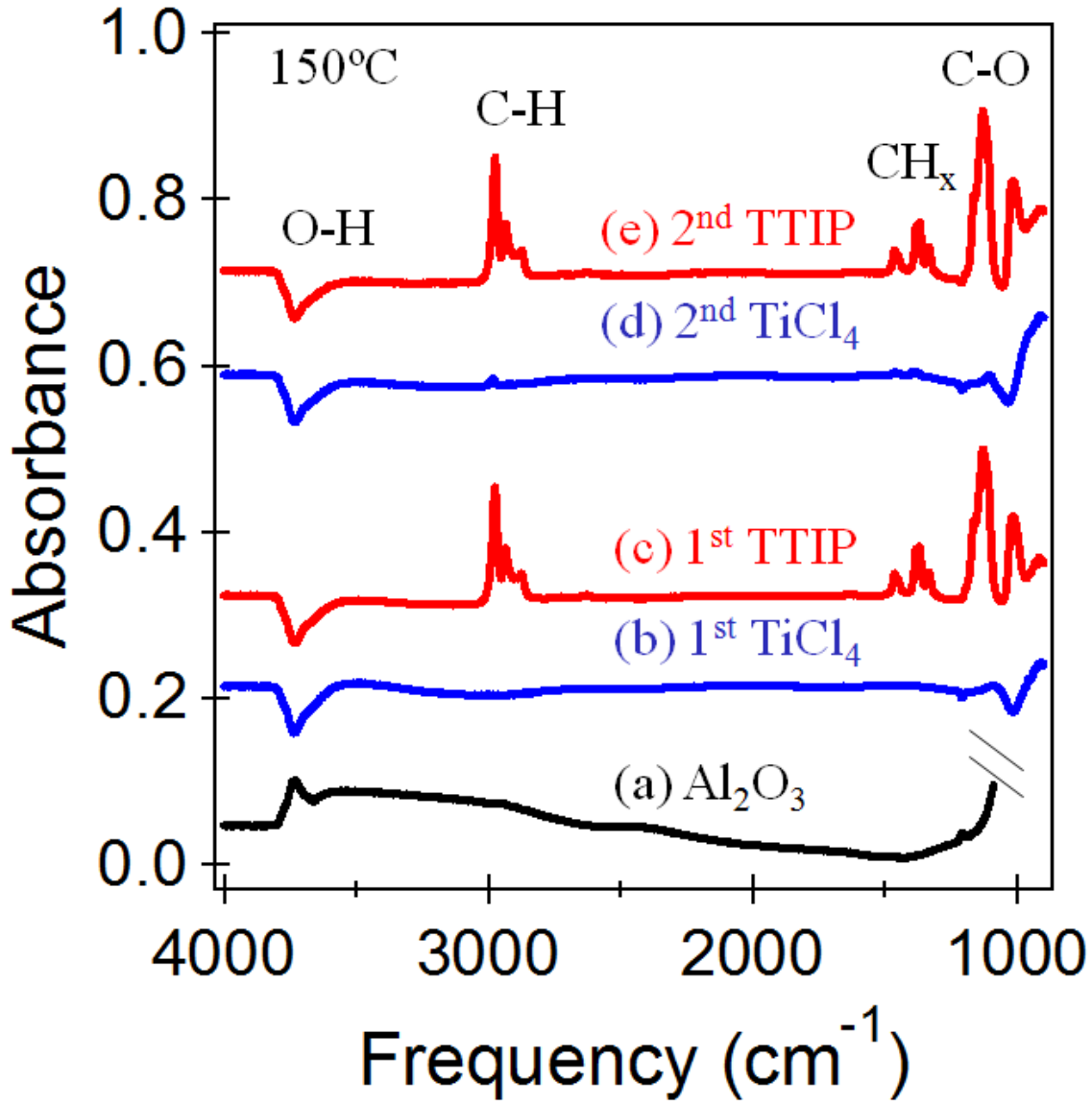

Figure 3.4: FTIR difference spectra for the the initial ALD aluminun oxide surface and subsequent two cycles of ALD TiO_2 cycle on that alumina surface. The ALD alumina spectrum is referenced to the starting zirconia substrate powder spectrum (a), and each half-cycle ALD TiO_2 spectra is referenced to the ALD alumina on zirconia spectrum, which includes the first $TiCl_4$ (b), the first TTIP (c), the second $TiCl_4$ (d), and the second TTIP (e). The substrate temperature during dosing was 150 °C.

at 3750 cm^{-1} are the free hydroxyl groups that are not hydrogen-bonded to each other. Similar results were observed in a previous FTIR study of TiO_2 ALD on ZrO_2 particles using $TiCl_4$ and H_2O.[52] Spectrum (b) also shows that the hydrogen-bonded Al-OH species are not lost between 3400-3700 cm^{-1}. This lack of a negative absorbance after referencing to the initial Al_2O_3 ALD surface indicates that these hydrogen-bonded hydroxyl groups do not react readily with $TiCl_4$. The growth of Ti-Cl vibrational features is not observed in spectrum (b) because the frequency of the Ti-Cl vibrational modes are below the cutoff frequency of the detector. The Ti-Cl stretching vibrational frequency is between 400-450 cm^{-1} in various titanium chloride complexes.[53] The Ti-Cl stretching vibrational frequency is 500 cm^{-1} in $TiCl_4$.[54] The FTIR spectrum after the 1st TTIP exposure is shown in spectrum (c). This spectrum is also referenced to the initial Al_2O_3 ALD surface. Consequently, the loss of Al-OH species at 3750 cm^{-1} remains in the FTIR spectrum. In addition, prominent new absorbance features appear at 2850-3000 cm^{-1} that are assigned to C-H stretches. Additional absorbance features also are present at 1300-1480 cm^{-1} that are assigned to CH_X bends. Strong absorbance features at 1020 and 1130 cm^{-1} are also assigned to CO symmetric and antisymmetric stretching modes. These peak identifications are based on earlier assignments in the literature.[6, 50] These absorbance features are consistent with isopropoxide groups on the surface. The FTIR spectra after the 2nd $TiCl_4$ and TTIP exposures is shown in spectra (d) and (e). These spectra are very similar to the spectra in spectra (b) and (c). These similar spectra indicate that the TiO_2 ALD reactions occurring during the sequential $TiCl_4$ and TTIP exposures are very consistent. This consistency suggests that the nucleation of the TiO_2 ALD on the Al_2O_3 ALD surface occurs without difficulty.

The difference spectrum shows that most of the surface species are reacted. The methyl stretching region shows four clear peaks, as expected for the in-phase and out-of-phase symmetric and antisymmetric stretching modes of the -CH_3 groups. The peak at 2630 cm^{-1} is tentatively assigned to the stretch of the -CH group attached to the oxygen and two carbons. The peaks at 1375 and 1385 cm^{-1} are associated with the gem-dimethyl structure of an intact isopropyl group, a promising sign that the TTIP reacts as proposed.

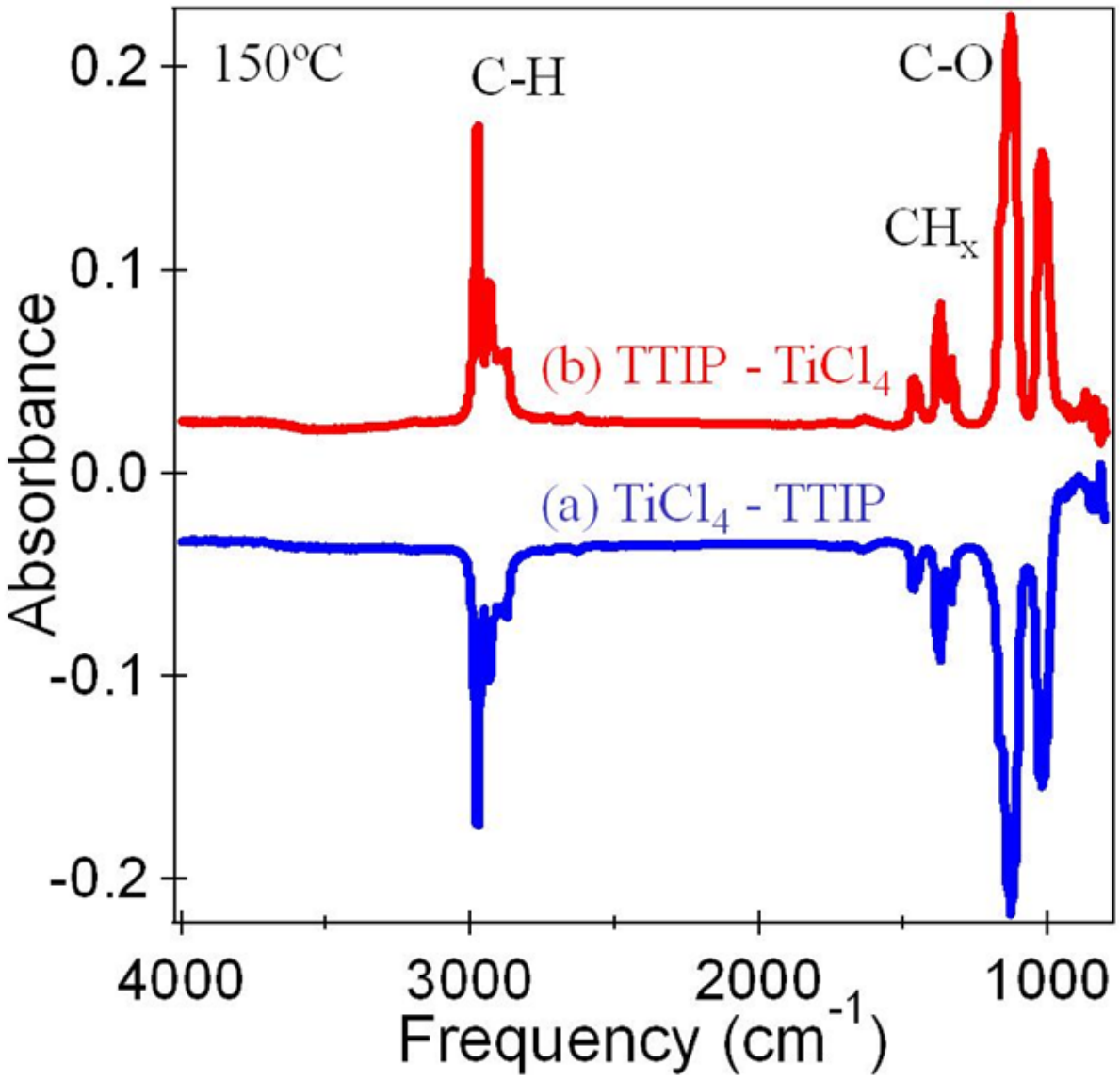

Figure 3.5: FTIR difference spectra of a $TiCl_4$ terminated surface referenced back to a TTIP terminated one, and a TTIP-terminated surface with the previous $TiCl_4$ terminated surface subtracted to show only the most recent changes. This shows dosing at 150 °C, and the half-reactions are from cycle 2.

A similar pair of difference spectra to Figure 3.5 is shown in Figure 3.7. As mentioned, the system showed reactivity from 150 to 300 °C, and it was interesting to see that O-H stretching features are visible on scans of the TTIP half of the cycles at and above 250 °C. Spectrum (a) in Figure 3.7 after the 2nd $TiCl_4$ exposure shows the loss of hydroxyl species at 3750 cm^{-1}. This loss is similar to the loss observed in Figure 3.5 and is consistent with the reaction of $TiCl_4$ with free hydroxyl groups that are not hydrogen-bonded to each other. Also, some of the hydrogen-bonded hydroxyl species are lost between 3400-3700 cm^{-1}. The hydrogen-bonded hydroxyl species are more likely to react with $TiCl_4$ at the higher temperature of 275 °C. The FTIR spectrum after the 2nd TTIP exposure is shown in Figure 3.7 spectrum (b). This spectrum is referenced to the previous $TiCl_x$ surface and there is a change in the observed absorbances for C-H stretching and bending vibrational modes that would be associated with isopropoxide species. The comparison between the FTIR spectra at 150 °C in Figure 3.5 (b) and 275 °C in Figure 3.7 (b) is dramatic. The absence of the C-H stretching and bending vibrational modes features indicates that the isopropoxide species are not stable at 275 °C. Additions in the hydroxyl region are apparent in the TTIP - $TiCl_4$ FTIR spectrum at 275 °C.

Regardless, the TiO_2 film growth continues, as $TiCl_4$ removes the O-H and isopropoxide features. Hydroxyls are known to be good reactive sites for $TiCl_4$, and are one of the reasons that water is used as a TiO_2 precursor. Without water, hydroxyls were not expected to be added at any time during the reaction.

The reaction mechanism is of great interest since it dictates the optimal deposition conditions. The (b) spectrum of Figure 3.7 shows that the surface products of reaction 2 cannot be the complete reaction mechanism during deposition at high temperatures. The reaction of $TiCl_4$ with the surface species is more complete than it was at 150 °C. To check that there was no appreciable water vapor leaking into the reactor, multiple $TiCl_4$ saturated surfaces were observed with FTIR. After two hours, no changes were apparent in the spectrum, and especially noteworthy is that no hydroxyls appeared in the spectrum. Because $TiCl_4$ is more reactive to water than TTIP, an appreciable amount of water should have been obvious during this experiment.

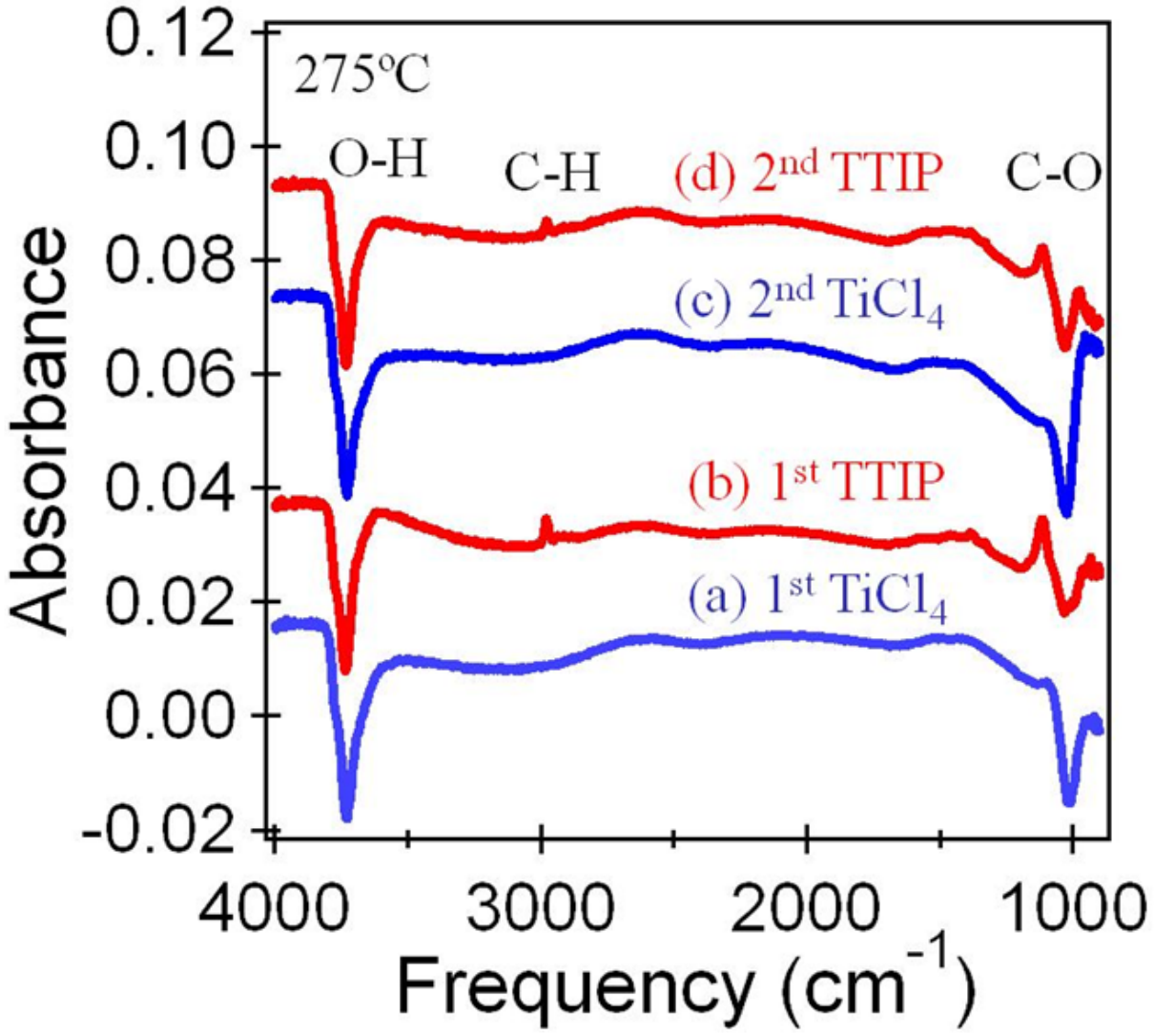

Figure 3.6: These are difference spectra taken at 275 °C. The bottom spectrum shows the change in features when a TiO_2 surface was reacted with $TiCl_4$. There is a loss of the hydroxyl stretch, C-H and C-O stretch, and H-C-H and O-Al-OH bend. The (b) was taken after reacting the $TiCl_4$-terminated surface with TTIP. The (c) and (d) half-reactions are from cycle 2. All of the spectra are subtracted by TiO_2.

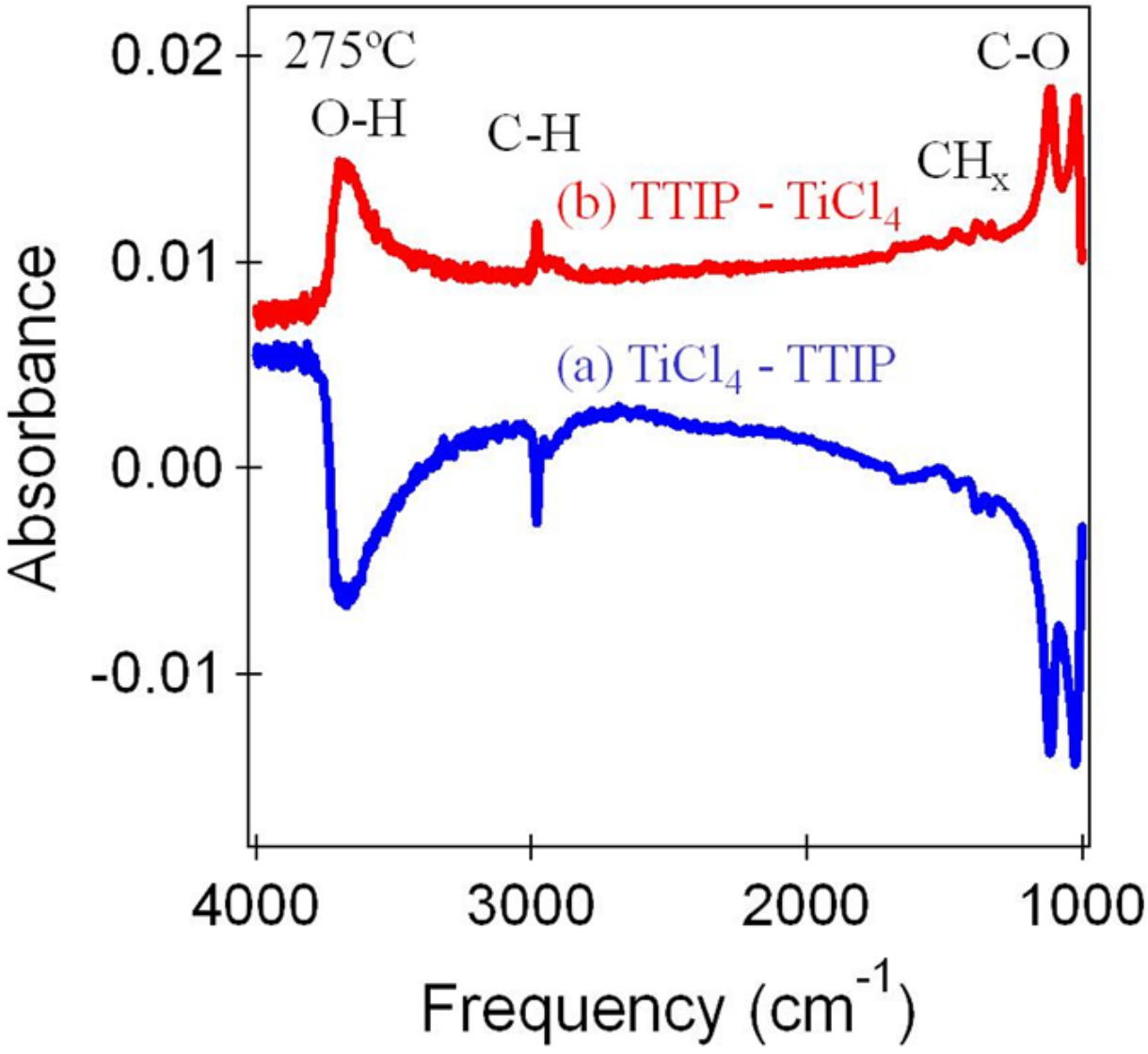

Figure 3.7: These are difference spectra taken at 275 °C. The bottom spectrum shows the change in features when a TTIP-terminated surface was reacted with $TiCl_4$. There is a loss of the hydroxyl stretch, C-H and C-O stretch, and H-C-H and O-Al-OH bend. The top spectrum was taken after reacting the $TiCl_4$-terminated surface with TTIP, and then subtracting the spectrum taken of the $TiCl_4$-terminated surface so that again, it is the differences that are apparent. The half-reactions are from cycle 2.

To explain the surfaces seen with the FTIR, it is helpful to recognize that isopropoxide groups are capable of elimination reactions. With siloxane and alkoxide groups that include β-hydrogens, there is a possibility of β-hydride elimination, as seen previously.[55] A TTIP-terminated surface has β-hydrogens, making the reaction a possiblity. A simple electron-pushing picture is shown to illustrate the process in Figure 3.8.

The addition of hydroxyl groups in Figure 3.7 following the TTIP exposure is consistent with the isopropoxide species undergoing β-hydride elimination to yield propene and surface hydroxyl groups at 275 °C. Figure 3.8 walks through a posited reaction mechanism for TiO_2 ALD at 275 °C, and includes the reaction of TTIP with $TiCl_x$ surface species. The isopropoxide species then undergo β-hydride elimination to produce surface hydroxyl groups as shown in Figure 3.8. These hydroxyl groups can then easily react with $TiCl_4$ to reform the $TiCl_x$ surface species and HCl as the gaseous reaction product. If this reaction were happening once titanium isopropoxide was populating the surface, we would expect to see both hydroxyl stretches and intact isopropoxide groups, and that is what is seen at the higher temperature range examined. Further, the progress of this surface reaction was observable on a timescale accessible to FTIR studies, since a reaction proceeding more quickly would give us significant amounts of hydroxyls at any temperature.
The features typical of the isopropyl groups were comparatively small, increased slightly on the first three or four mini-doses at a much slower rate than they had at lower temperatures, and remained very similar through most of the dosing. If hydroxyl formation was due to a secondary reaction, then these results support our hypothesis. Isopropoxide groups would be attached to the titanium bonded to the surface, and then convert themselves to hydroxyl groups bound to titanium as well as propene molecules that would be pumped away. There is a possibility that TTIP will react with hydroxide groups, making the reaction close to but not necessarily completely self-limiting.

In order to further explore the expected surface reactions taking place after dosing, the alumina surface was saturated with $TiCl_4$ and then TTIP at a range of temperatures. Scans of the surface were taken as the TTIP saturated surface remained under nitrogen gas flow. With no

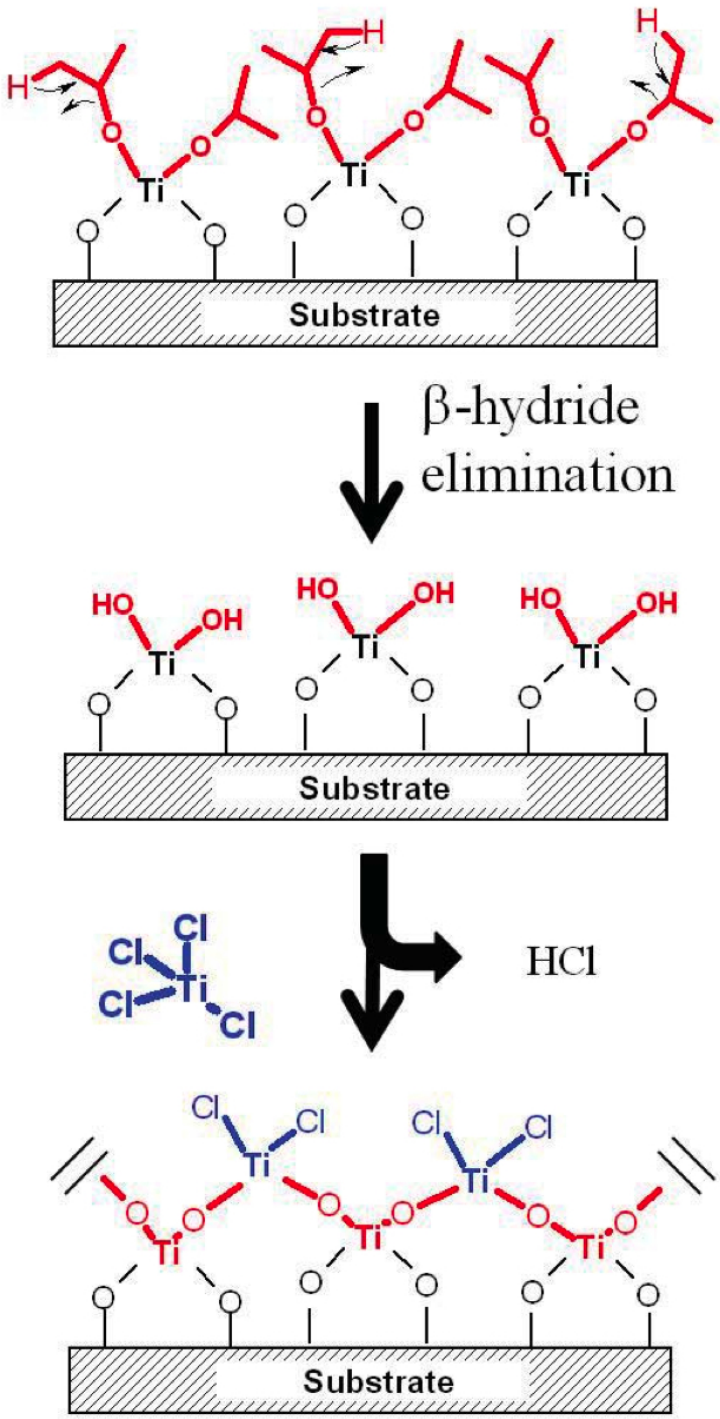

Figure 3.8: Electron pushing is shown to illustrate the β-hydride elimination reaction mechanism. The reaction breaks the oxygen-carbon and hydrogen-carbon bonds while forming the oxygen-hydrogen and carbon-carbon pi bond, turning the isopropoxide group into hydroxide and a propene molecule.

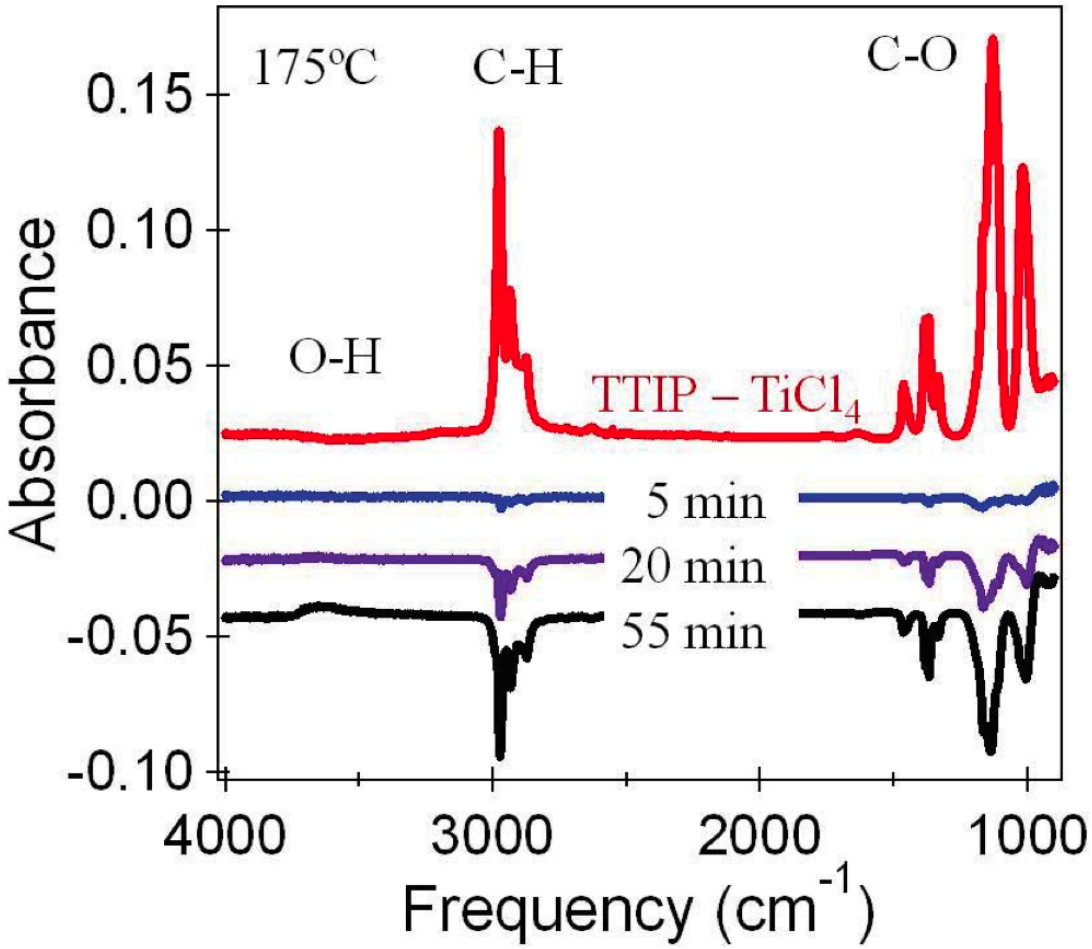

Figure 3.9: The top is a difference spectrum showing features added during the TTIP half of the cycle, with the previous $TiCl_4$ spectrum subtracted. The three scans underneath are difference spectra, with the TTIP spectrum subtracted, showing the change in the surface over time with no dosing occurring, and show scans at 5, 20, and 55 minutes after the initial top scan, considered time zero. This experiment was done at 175 °C.

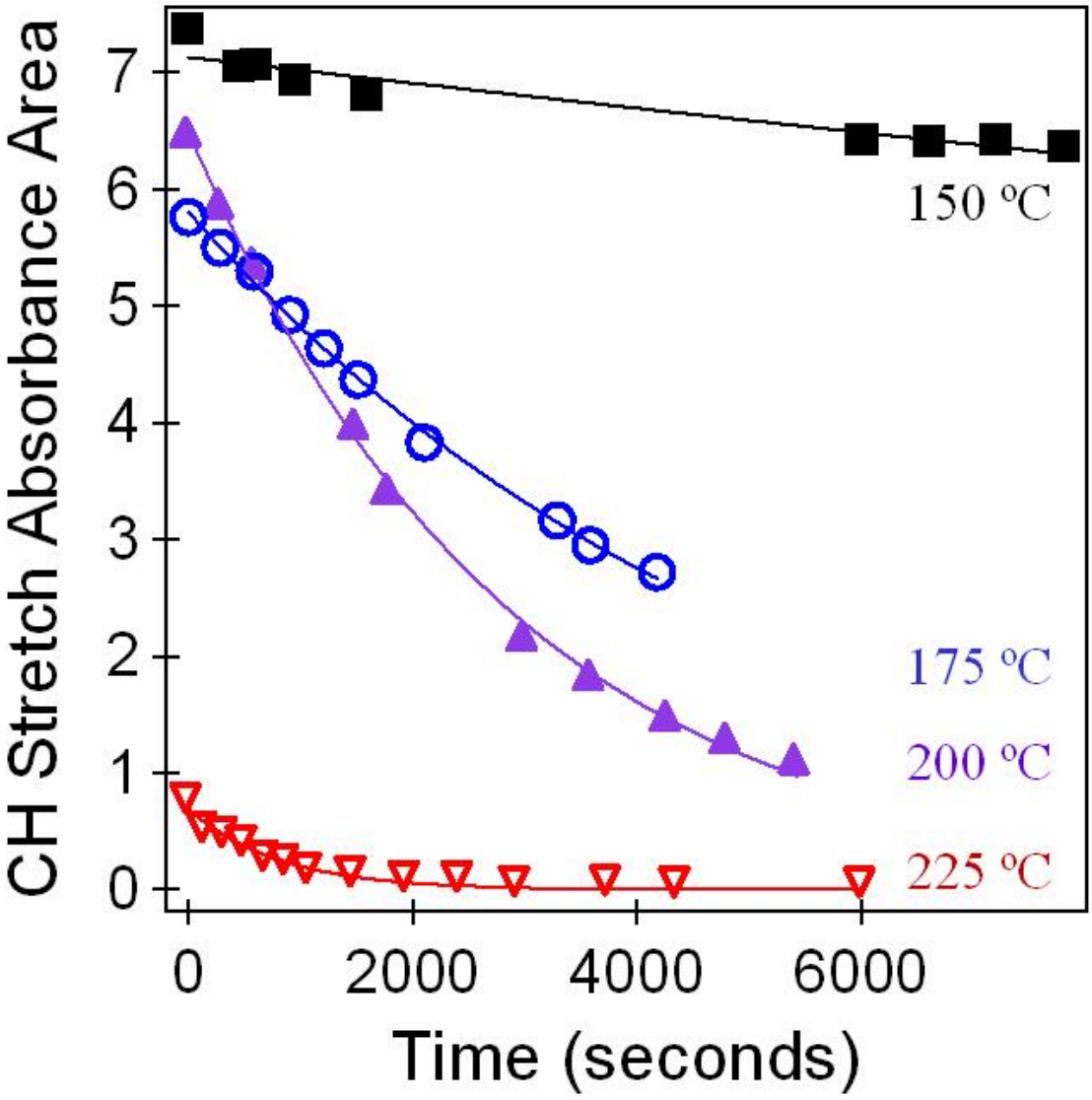

Figure 3.10: This shows the disappearance of C-H stretch over time for four temperatures. From top to bottom, the data series are for 150, 175, 200, and 225 °C. The Starting C-H stretch peak area was slightly different for each experiment, showing both dependence on surface saturation and the surface area in the FTIR beam. The data are shown as points, and the lines are included to guide the eye.

dosing, changes to the spectra became apparent over time. Figure 3.9 shows the changes to an isopropyl-terminated surface over time at 175 °C. The top scan is a difference spectrum of a TTIP saturated surface referenced back to a $TiCl_4$ saturated surface, showing the same features seen in the scan of a TTIP saturated surface in Figure 3.5.

The spectra shown below at subsequent times show the decrease in the carbon-hydrogen and carbon-oxygen bonds, and the increase in the hydrogen-oxygen bonds. Hydroxyl features appeared and increased, while isopropoxide features decreased. The hydroxyl peak appearance supports the β-hydride elimination reaction, since the possibility of a leak had been ruled out. The visible additions of O-H and subtractions of C-O and C-H vibrations are consistent with the proposed elimination, and the propene formed would be gaseous and therefore not visible on the surface, since it would be evacuated by the pump. In order to see if it actually was present, mass spectrometry analysis was performed on the waste stream of the reactor and that experiment is described in Figure 3.12. The same experiment shown in Figure 3.9, carried out at three other temperatures, showed similar behavior, with hydroxyl groups apparent sooner at higher temperatures. The data in Figure 3.10 show the results of following the C-H stretch area at 150, 175, 200, and 225 °C under inert nitrogen gas flow. Each starting surface had a different amount of starting C-H stretch in the beam, since scanned surface area is dependent on particle number in the beam of the FTIR and is changeable by moving the sample within the reactor. The initial integrated absorbances tend to start smaller at higher temperatures because some species were lost before the collection of the FTIR spectra, and the higher the temperature, the faster the loss.

Using initial slopes and assuming first order kinetics, the rate constants were determined for each temperature. An Arrhenius plot gives the activation energy for the beta-hydride elimination. The reaction involves bond-breaking, and the energy barrier of 15 +/- 2 kcal/mol gives information about the expected speed of reaction at temperatures not attempted. Slightly different behavior would be expected at the start of the reaction, since the environment of the initial surface would have some influence, and that means that nucleation behavior could vary. This was not explored quantitavely, but qualitatively, minor differences were noted when the reaction took place on alu-

minum oxide, zirconium oxide, or silicon oxide.

In order to determine if the reactions demonstrate the self-limiting behavior characteristic of ALD, small doses of precursor were introduced to the surface, an FTIR scan was taken after each dose, and the area of a selected surface vibration, in this case O-H stretch, was followed. The saturation behavior of $TiCl_4$ is well studied, and shows expected behavior in Figure 3.11. The TTIP side of the cycle does not make it easy to claim self-limiting behavior. At low temperatures the reaction appeared self-limiting, but at higher temperatures the reaction seemed to slow down, but not completely stop. The hydroxyl stretch was one of the more prominent features to follow, but because of the expected secondary β-hydride reaction and the probable desorption of hydroxyls from the surface, there were no ideal stable vibrational modes to track during dosing. Therefore, this experiment mainly gave a sense of soft self-limiting behavior, and the authors note that consistency in dosing could be more important than normal for this system.

3.3.2 Quadrupole Mass Spectrometry

Since FTIR data suggests that TTIP undergoes a secondary β-hydride reaction in which propene is a by-product, the gas waste stream was monitored using mass spectrometry. Finding propene in the reaction waste gases would provide strong support for the β-hydride elimination reaction. Test gases were flowed through the empty reactor while the leak valve into the lower turbo pump chamber was open, diverting a fraction of the stream into the turbo pumped quadrupole mass spectrometry region. Cracking patterns of the gases tested accorded with the patterns found in the database of the National Institute of Standards and Technology. Examined were isopropanol, 2-chloropropane, titanium tetrachloride, and titanium tetraisopropoxide.

Propenes most intense mass-to-charge ratio, m/z at 41. This m/z is one less than the parent mass of 42. Fragmentation of TTIP, isopropanol, and 2-chloropropane all produce a peak at 41, so attention to other peaks in each fragmentation spectra is required. TTIP, for example, has its most intense peak at 45, which is suspected to be the CH_3CHOH^+ fragment. The cracking pattern of

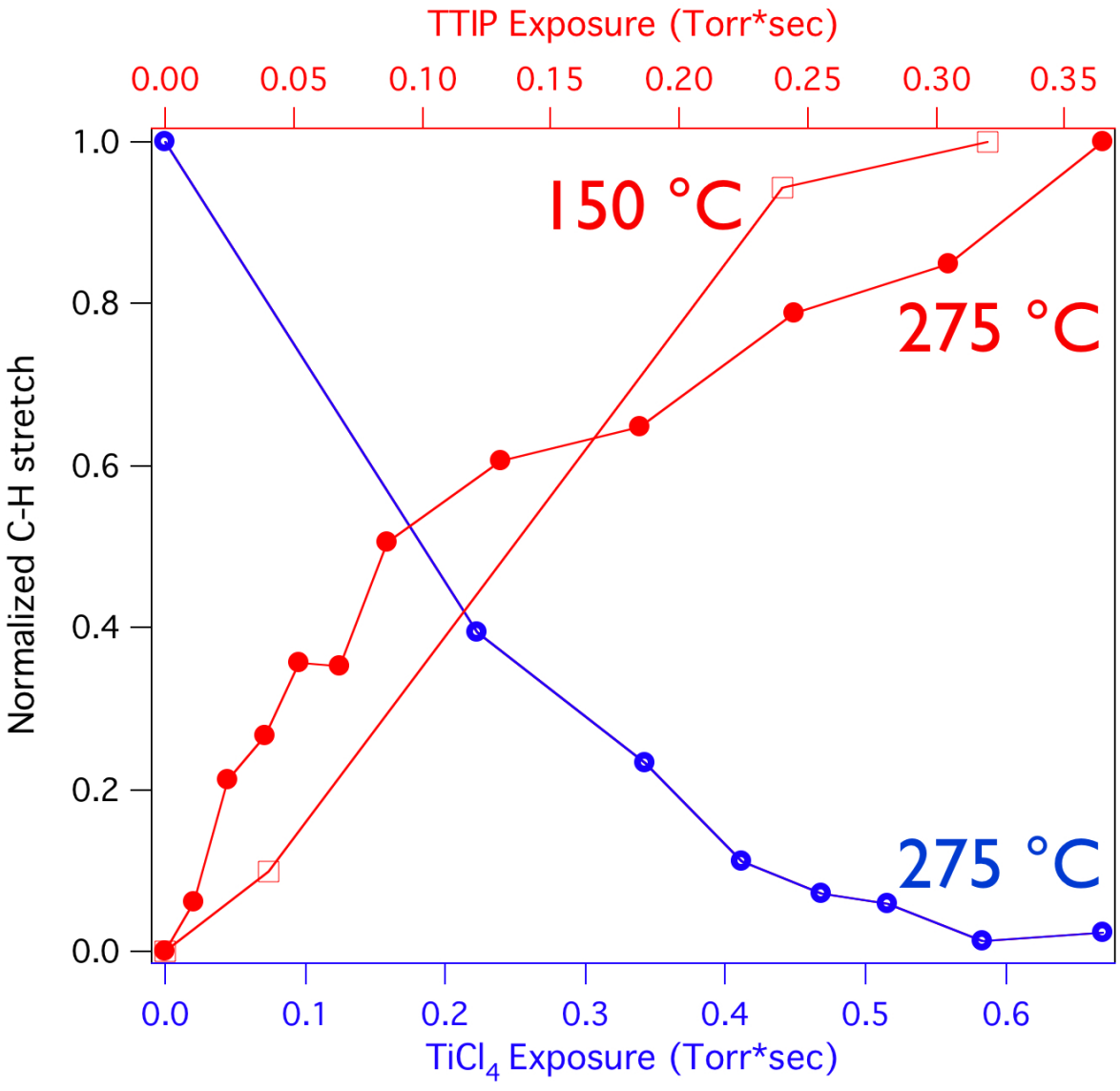

Figure 3.11: Uptakes of $TiCl_4$ and TTIP at 275 °C are given together here. The $TiCl_4$ process was self limiting at any temperature checked. The TTIP, on the other hand, showed only soft self-limiting behavior at high temperature. A few data points of TTIP addition at 150 °C are included to show that though a full data set was not collected, TTIP behavior was repeatedly observed to be closer to self-limiting at lower temperatures.

TTIP shares much similarity with 2-propanol, as the ligands are relatively easily fragmented from titanium. Therefore, if the m/z 41 and 45 signals were followed during a dosing experiment, and 41 increased but not 45, the chemical observed could not be TTIP. The other expected product, 2-chloropropane (Reaction 2), also has a peak at 41, but the dominant peak is at 43, which is most likely $CH_3CHCH_3^+$ after chlorine breaks off.

With the likely by-products characterized, certain mass to charge signals were followed during the reaction. The use of static dosing allowed the reactants and products to be observed clearly. Three small doses of precursor were introduced to the surface while the valve to the mechanical pump was closed, so gases were forced through the leak valve via the turbo pump in the mass spectrometry chamber. The mechanical pump was then used to evacuate the reactor chamber before the next precursor exposure.

Dosing of $TiCl_4$ onto a hydroxyl-terminated surface gave a strong HCl signal (m/z of 36 and 38 in the expected chlorine isotope proportion), and is the expected volatile by-product in reaction 1. When TTIP was dosed onto a $TiCl_4$ terminated surface the signal at 41 and 43 climbed, and then 41 continued to rise while 43 leveled off. Even after purging, the signal at 41 continued rising. Initial dosing showed substantial gain of 41 with less 43 and very little 45, meaning that almost none of the signal at 41 is due to TTIP precursor and cannot be solely due to 2-chloropropane. As the dosing continued, the signal at 45 started to increase relative to 41 and 43, starting from background. Presumably, the majority of the TTIP reacted with the surface, producing 2-chloropropane and then propene. Further dosing caused the surface to become saturated, the -hydride elimination reaction slowed as the conversion neared completion, and more TTIP precursor and less reaction products flowed out of the reactor. Figure 3.12 shows one of these experiments. For simplicity, only m/z signals of 41 and 45 are included for the three doses displayed. This result strongly suggests that propene was being generated for a time after the surface had been in contact with the TTIP reactant, supporting the proposed mechanism.

Further TTIP dosing will eventually lead to the saturation of the TTIP reaction. At the point of

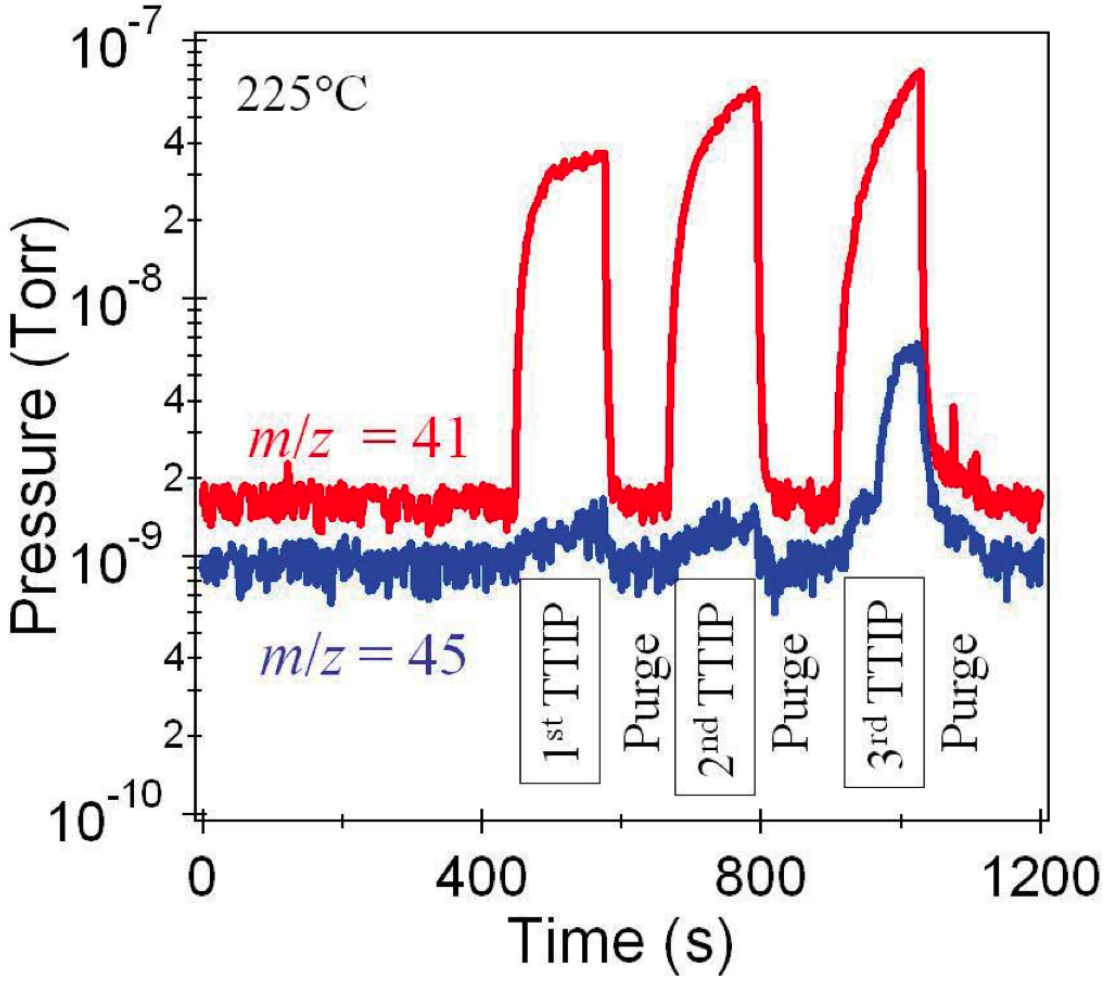

Figure 3.12: Mass spectrometry results for static dosing at 225 °C. The top data show the mass to charge signal of 41 for four doses of ttip onto a $TiCl_X$ terminated surface. The bottom data are for the mass to charge of 45. The parent, TTIP, would show more signal at 45 than 41, so this is due to reaction product.

saturation, TTIP should be observed in the mass spectrum. Figure 3.12 shows the results for m/z= 41 and m/z= 45 for sequential TTIP exposures at 225 °C. The signals for m/z= 45 have been offset slightly to avoid overlap with the signals at m/z= 41. The 1st TTIP produces mostly mass signal at m/z= 41 that corresponds to 2-chloropropane and possibly some propene. The negligible signal at m/z= 45 indicates that all of the TTIP is consumed to produce reaction products. The results are very similar for the 2nd sequential TTIP exposure. These results are expected if the TTIP reaction has not reached saturation. The signal at m/z= 41 again corresponds to 2-chloropropane and possibly some propene. The 3rd TTIP leads to the appearance of mass signal at m/z= 45. This signal results from TTIP and indicates that the TTIP reaction has reached completion. Additional TTIP exposures now all produce signal at m/z= 45 because the reaction is self-limiting and TTIP can reach the mass spectrometer.

3.3.3 ALD TiO_2 Film Growth

An examination of the character of the growing TiO_2 films includes FTIR spectra over many cycles. In Figure 3.13, the bulk modes of TiO_2 are examined by scanning after multiple cycle deposition on silica powders, allowing a look at the lower area of the spectrum where the in the other experiments, the zirconia bulk modes interfered with analysis.

Figure 3.13 shows the FTIR spectra in the frequency region between 500-1000 cm^{-1}. One absorbance peak is observed between 850-950 cm^{-1}. Another broad absorbance peak is observed at 500-750 cm^{-1}. This peak may be a shoulder of an absorbance peak with its maximum absorbance at ¡500 cm^{-1} because the infrared detector employed in these experiments does not respond below 500 cm^{-1}. The breadth of these peaks suggests the partial amorphous nature of the TiO_2 film.[56] The absorbance spectra in Figure 3.13 appears similar to the absorbance of TiO_2 films deposited using plasma-enhanced chemical vapor deposition (PE-CVD) with $TiCl_4$ and O_2.[56] These PECVD TiO_2 films were amorphous and displayed no XRD peaks after deposition at ¡65 °CC. The PECVD films began to display crystallinity consistent with anatase TiO_2 after annealing at 600 °C. The absorbance in the region of 700-950 cm^{-1} has been assigned to longitudinal optical (LO) vibration

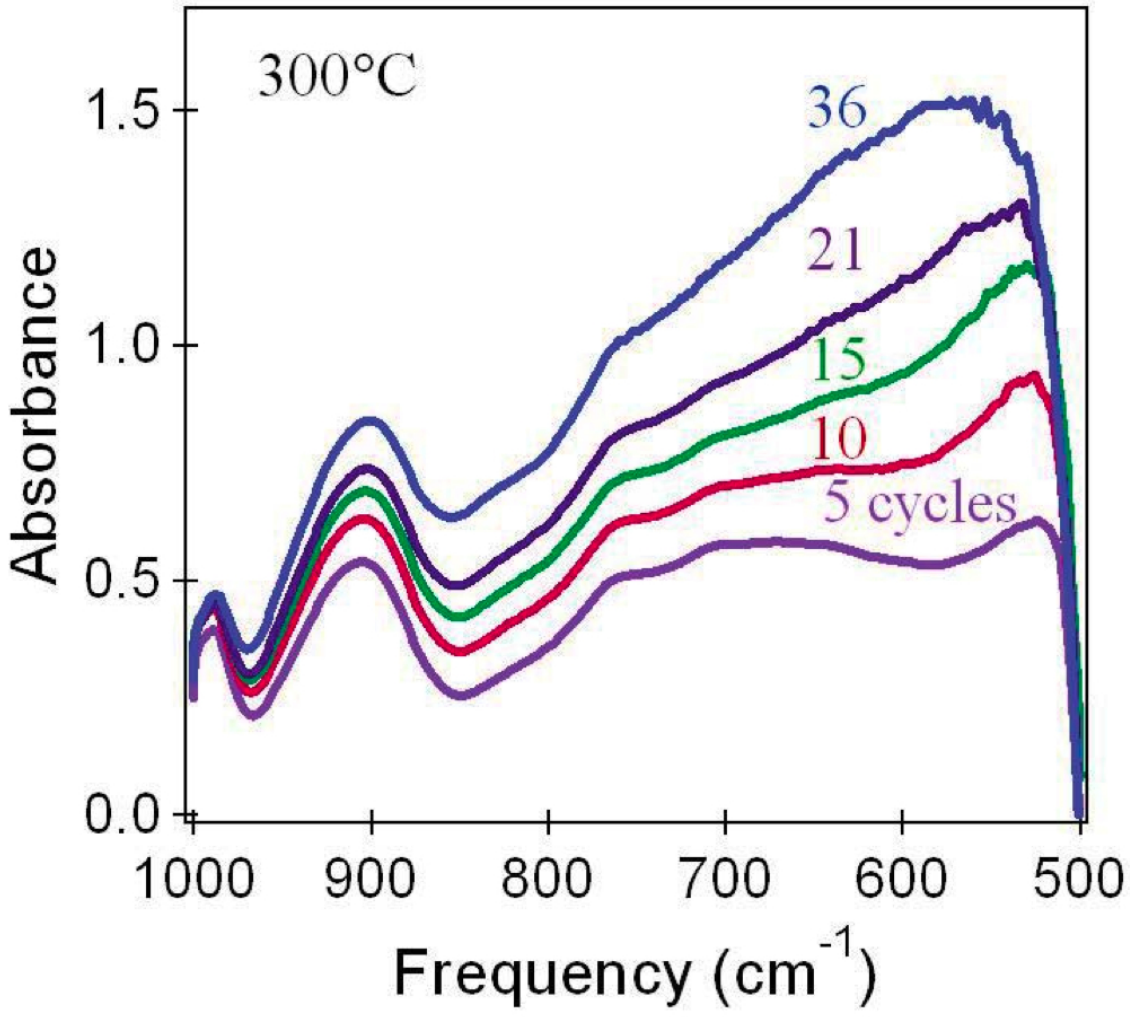

Figure 3.13: Growth of TiO_2 bulk modes on SiO_2 at 300 °C. The peaks at 540 and 780 cm^{-1} indicate increasing TiO_2.

of the Ti-O bonds in the TiO_2 film.[56] The absorbance in the region of 400-600 cm^{-1} has been assigned to transverse optical (TO) vibration of the Ti-O bonds.[56]

Because the two absorbance features grow progressively with number of TiO_2 ALD cycles, these peaks are believed to be due to the TiO_2 ALD film. In addition, the absorption peak between 850-950 cm^{-1} may be influenced by the formation of an aluminum titanate. A previous infrared study of TiO_2/SiO_2 multilayers observed a peak at 930 cm^{-1} that was assigned to Si-OTi species.[57] This absorbance peak was observed only in the composite TiO_2/SiO_2 films.

In a separate reactor another *in situ* technique took place, where quartz crystal microbalance analysis allowed measurements of the mass gained over multiple cycles of the TiO_2 ALD films. Results for QCM experiments at 150 °C and 250 °C under the same reaction conditions are shown in Figure 3.14.

The mass gained with each TiO_2 ALD cycle growth rate changes with temperature. For low temperature growth, 3 ng/cm^2 was seen at 150 °C, and for high temperature growth, 15 ng/cm^2 at 250 °C. This large difference in growth rate at 150 °C and 250 C is attributed to the difference in reaction mechanism. At 150 °C, the isopropoxide species does not undergo β-hydride elimination. The $TiCl_4$ is forced to react with the isopropoxide species on the surface. At 250 °C, the isopropoxide species can undergo β-hydride elimination and produce hydroxyl surface species. The larger growth rate at 250 °C suggests that the $TiCl_4$ can react more easily with these hydroxyl species. For TiO_2 ALD films grown on Al_2O_3 ALD-coated silicon wafer, the growth rate was 0.55 0.05 Å/cycle at 250 °C. In comparison, using the density of 3.3 g/cm^3 for the TiO_2 ALD film determined by XRR, the mass gain of 15 ng/cm2 at 250 °C was consistent with a growth rate of 0.5 Å/cycle. This growth rate is also somewhat lower than the growth rate of 0.7 Å/cycle measured by recent ellipsometry studies.[36]

The quartz crystal microbalance shows added mass throughout the dosing sequence, and the FTIR agrees by showing that gains of the TiO_2 film modes, and the surface species are not just replacing each other during reaction, but forming layers of film. The bulk modes are consistent with the exclusion of the ligands on the precursors in the main film. That is not to say there is not

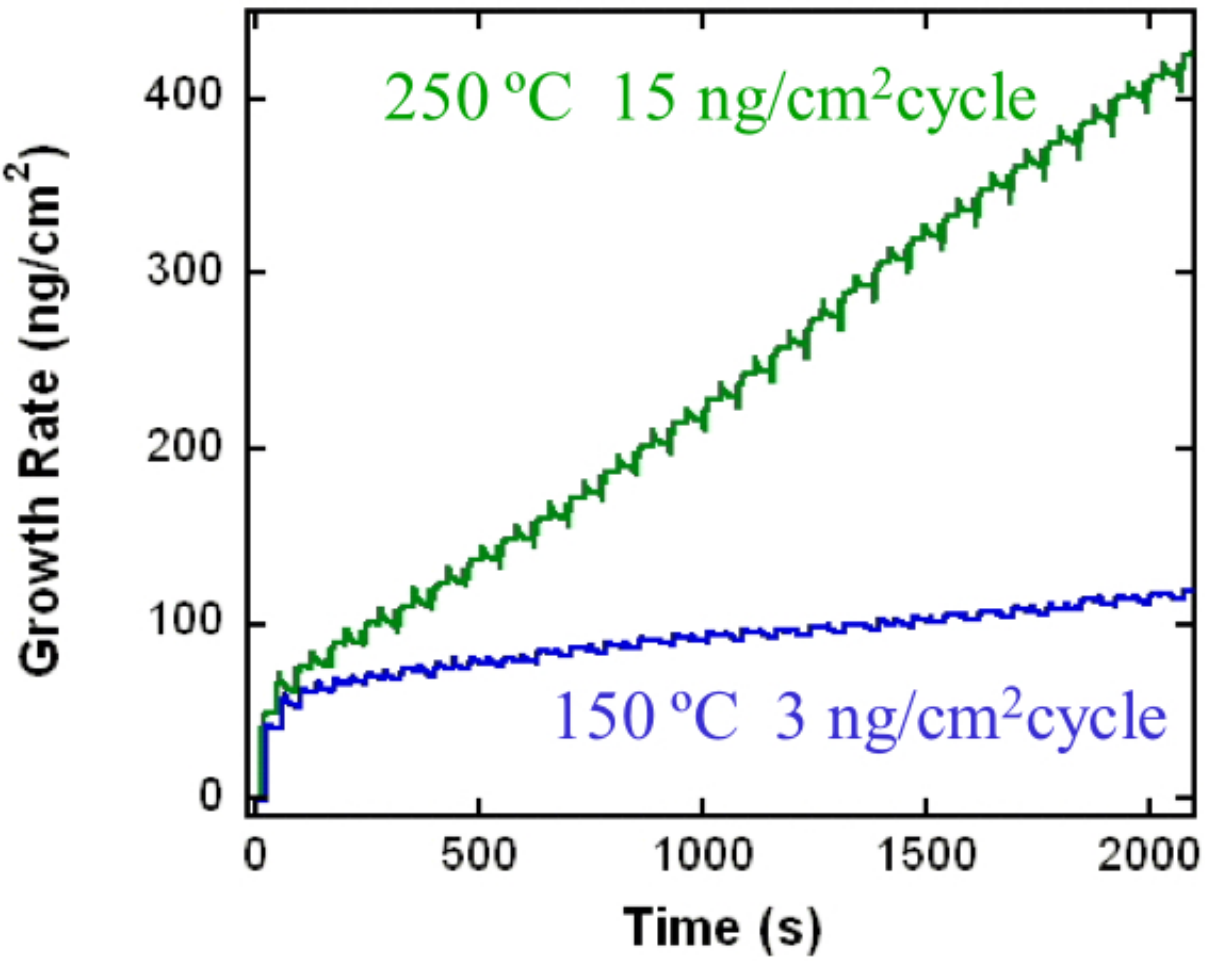

Figure 3.14: This quartz crystal microbalance plot shows the mass added with dosing of precursor. The higher (top) growth rate was recorded at 250 °C, and the lower growth rate line grew at 150 °C.

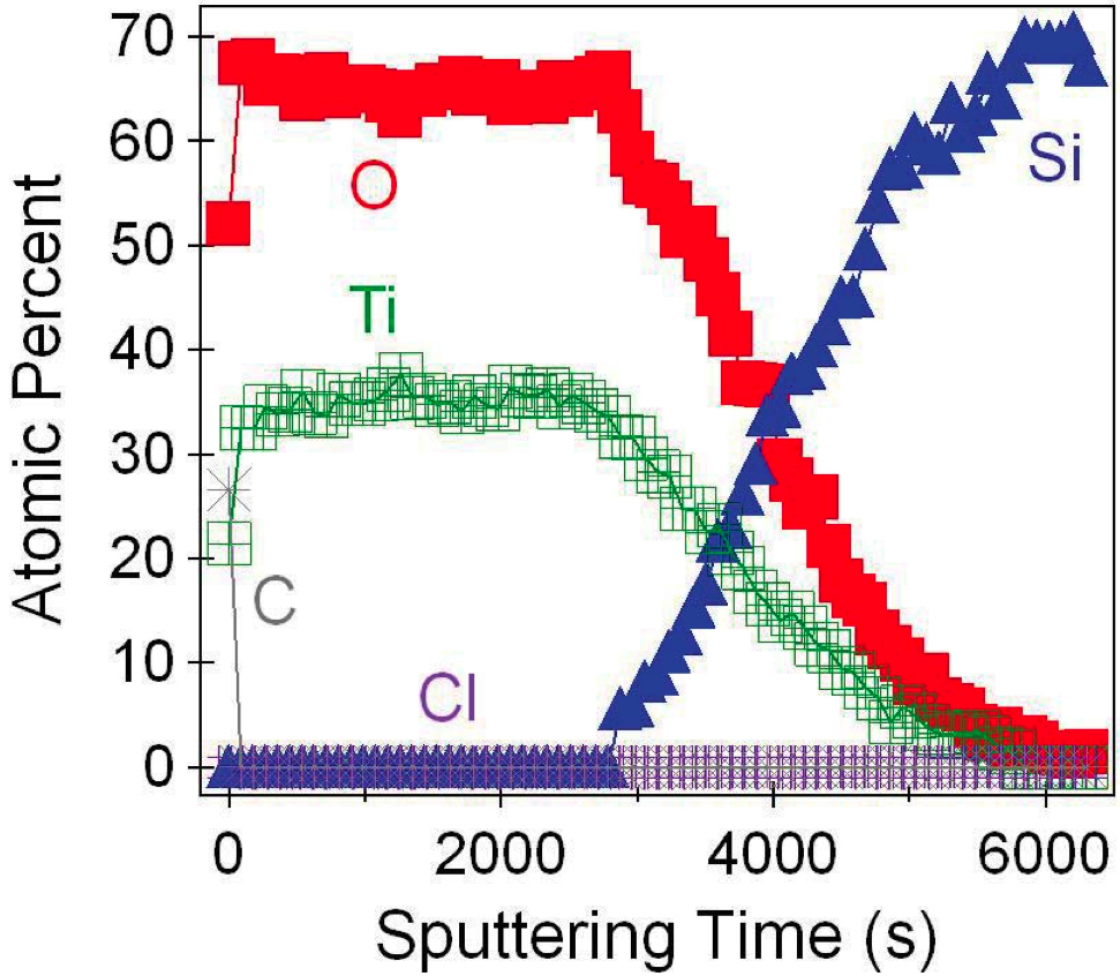

Figure 3.15: This is an elemental depth profile using X-ray photoelectron spectroscopy of TiO_2 deposited at 250 °C. The proportions of the elements titanium, oxygen, carbon, chlorine, and silicon in the film were detected during sputtering. The longer the etch time, the deeper the film has been sputtered. The surface carbon from air exposure is quickly removed, and titanium oxide has lower than detectable amounts of carbon and chlorine impurities. The silicon substrate is eventually exposed.

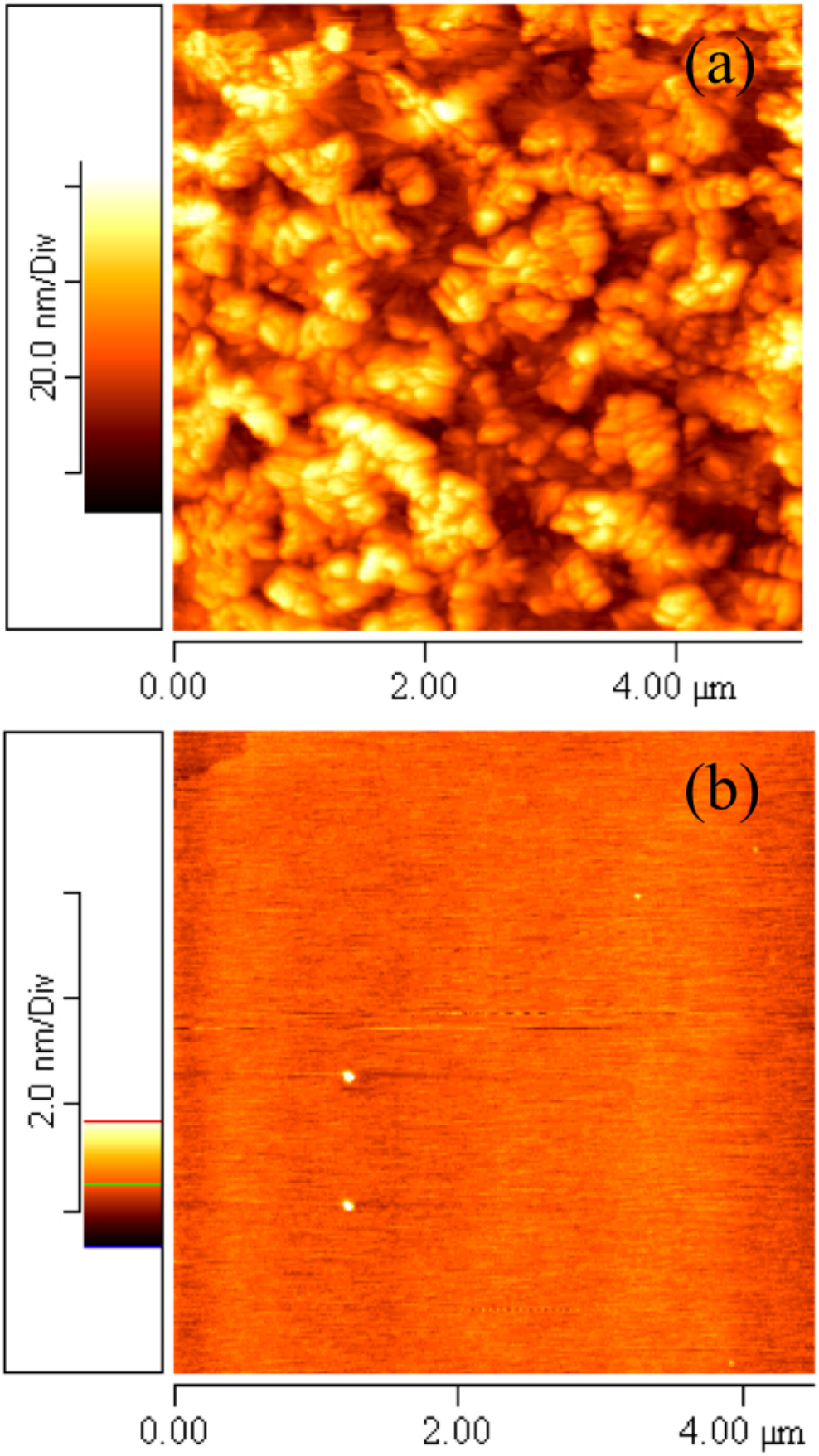

Figure 3.16: The AFM image a) is of a 26 ångstrom thick TiO_2 film with an RMS roughness of 2 ångstrom, and the image b) is of a 200 ångstrom thick TiO_2 film with RMS roughness of 90 ångstroms. Films were deposited at 250 °C.

contamination but these quantities are of much lower total atomic percentage. To quantify this, an elemental analysis was performed using X-ray photoelectron spectroscopy (XPS), during a depth profile via argon sputtering (Figure 3.15).

To confirm that the deposition proceeds as expected, ex situ X-ray photoelectron spectroscopy (XPS) scanning of film grown at 250 °C was used to determine the elemental composition. Figure 3.15 shows the depth profile of a 100-cycle sample (approximately 55 Å), and includes likely contaminants. The carbon was of interest, since any *ex situ* technique involves atmospheric exposure leading to adventitious carbon on the surface. That there was surface carbon is clear from Figure 3.15, as it was also apparent that both carbon and chlorine are below the detection limit of 1% in this film. Both carbon and chlorine are possible contaminants in the film if there were incomplete ligand removal. Titanium and oxygen are in the 2:1 ratio of TiO_2, and as the sputtering penetrated the film deeper, the silicon signal began growing in.

The XRR showed that film thicknesses less than 70 ångstroms were quite smooth as shown by an RMS roughness of approximately 5 ångstroms or less. For films over 100 ångstroms thickness the roughness increased sharply, and for 110 ångstroms film the roughness was on the order of 30 ångstroms. Looking at a range of thicknesses using atomic force microscopy (AFM), it appeared possible that the thicker films displayed a crystalline character, while the thin films are amorphous. Using XRD on a sample grown at 250 °C, the peak for anatase crystal phase was seen. Figure 3.16 shows examples of a 26 ångstrom film and a 200 ångstrom film examined with AFM.

3.4 Conclusion

The atomic layer deposition of titanium dioxide using titanium tetraisopropoxide (TTIP) as the oxygen source happens at a range of temperatures with titanium tetrachloride $TiCl_4$, growing 0.55 Å/cycle at 250 °C, and having lower growth per cycle at lower temperatures. The surface species and reactions were studied using an *in situ* transmission FTIR system. A secondary reaction on TTIP exposed surfaces explained the change in growth per cycle with temperature. The

mechanism includes the formation of surface hydroxyl groups during the TTIP half cycle, and this becomes a very significant influence at 250-300 °C. This was indicated by FTIR and mass spectrometry to be due to the side reaction of β-hydride elimination. The hotter the surface, the faster the presumed β-hydride elimination can take place, leaving hydroxyls rather than isopropoxide groups for the $TiCl_4$ to react with. At 150-225 °C, the β-hydride reaction was slower, with the isoproxide groups' reaction with $TiCl_4$ resulting in a lower growth rate. Quartz crystal microbalance gave a contrasting 3 ng/cm^2 per cycle mass addition at 150 °C, and a 15 ng/cm^2 per cycle mass addition at 250 °C. The films grown at 250 °C contained less than one atomic percent of impurities of carbon and chlorine from unreacted ligands on the precursors.

3.5 Acknowledgments

Andrew S Cavanagh took the XPS data, Aziz I Abdulagatov recorded the QCM, and Zachary M Gibbs took the AFM images. Useful discussions with David Goldstein improved the the project. The research was funded by the Information Storage Industry Consortium (INSIC).

Chapter 4

Control of ALD Platinum Particle Size and Coverage on Metal Oxide Powders

4.1 Introduction

The recent advances in the atomic layer deposition (ALD) of metals opens up interesting possibilities.[58, 43] Typically, ALD, a variant on chemical vapor deposition, is the best choice when solution based methods do not allow enough control over film thickness, and techniques such as chemical vapor deposition and sputtering will not evenly coat complex or high surface area substrates.[3] Stepping aside from the usual conformal film growth of ALD, the deposition of platinum was here deliberately designed to encourage particle growth. Other researchers have likewise grown particulate platinum with ALD, usually for catalytic purposes, and this study attempts some understanding of a method for fine tuning of the control of particle size and spacing.[59, 60, 61] Many studies of platinum and noble metal ALD have been reported.[62, 63, 64, 65, 66, 67, 68] The affinities between the substrate and deposited platinum varied, changing how strongly the platinum preferred binding to itself over the substrate. In situations with large surface energy mismatch, the initial stages of platinum deposition showed formation of islands of platinum, and it took several cycles for the islands to grow together into a conformal film. The match between substrate and platinum contributes to the thickness at which coalescence occurs. The choice of precursors can also make a difference in the length of the nucleation period. As the platinum molecules need to be reasonably volatile, the options include platinum II acetylacetonate ($Pt(acac)_2$)[69], which has a small window between reasonable vapor pressure and decomposition, leading to the more common use of platinum II hexaflouroacetylacetonate ($Pt(hfac)_2$)8[59], and the current most

commonly used and most volatile of the three, (methylcyclopentadienyl) trimethylplatinum (IV) (Me_3PtMeCp).[70, 37, 71, 72, 73] The platinum deposition using platinum (II) acetylacetonate and platinum (II) hexafluoroacetylacetonate (Pt(hfac)$_2$) has been done with reducers, or occasionally with oxidizers, while the deposition using trimethyl platinum (IV) methylcyclopentadienyl (Me_3PtMeCp) with oxidizers, in what appears to be a combustion process, and less often with reducers.[74, 61, 75, 76] Pt(hfac)$_2$ and formalin was expected to show similarity to the Pd(hfac)$_2$ and formalin reaction.[63, 77, 78] In addition, because platinum catalyzes hydrocarbon breakdown, the mechanism of ligand removal could include increasing influence from the deposited platinum over the course of the reactions.[79, 80] Other researchers have examined the mechanism of the oxygen and Me_3Pt(MeCp) ALD process, Aaltonen, Elam, and Kessels among them.[81]

In order to discourage conformal films, this work is done with the Pt(hfac)$_2$ precursor, as well as the reducer formalin, a mixture of formaldehyde, methanol, and water. Since we stayed in what would be considered the nucleation regime, we chose the relatively strong reducing ability of formalin.

This studys aims included understanding of the available control of the surface dispersion of platinum and was guided by considerations in replacing platinum particles on carbon as a fuel cell cathode material. Polymer electrolyte membrane fuel cells (PEMFCs) powered by hydrogen and oxygen could become a more efficient alternative to existing fossil fuel-based engines for automobiles due to their high energy conversion efficiency and sometimes non-polluting emissions. However, in order to be commercially viable, current PEMFC designs must meet difficult challenges for low cost, durability, and performance.[82, 83, 84, 85] Currently hindering progress in commercialization, the cathode catalyst for the oxygen reduction reaction (ORR), demonstrates insufficient durability and activity. The most common available cathode catalysts consist of Pt or Pt-alloy nanoparticles evenly distributed on high surface area carbon black.[86] High loadings of Pt are required to overcome the slow reduction kinetics, which increases the overall fuel cell cost. Platinum is currently the best of the electrode materials, making it worth the large effort to extract and refine. Using as little as possible is the current goal, and further understanding the atomic layer deposition of platinum could cause improvement in the activity and lifetime of the cathode of PEMFCs. Atomic

layer deposition includes the possibility of alloying the platinum, as has been done with iridium and other metals.[81]

Additionally, oxidative corrosion of the carbon black in the operating voltage and pH regime decreases the fuel cell durability leading to a shorter operating lifetime. Metal oxides from Ti, Zr, Ta, and W, however, resist corrosion more than carbon in this operating regime and are therefore strong candidates to replace carbon black as the cathode catalyst support.[87] Of these metal oxides, tungsten oxide may be among the most desirable due to its ability to catalyze the oxygen reduction process in the cathode.[88, 89, 90] Tungsten oxide is an electrochromic material, and the tungsten relatively easily changes its oxidative state. When tungsten is at a +6 charge, the tungsten oxide is green-yellow in color, and when tungsten is +2, the tungsten oxide is dark blue. Between those two states are a range of colors, mostly blue. In this work, the tungsten oxide was a range of oxidation states, and will be referred to as WO_X in general. Most of the mentioned experiments were done on dark blue tungsten oxide, meaning the tungsten was less oxidized than experiments done on light blue (probably having the widest range of states of any of our samples), or green-yellow. The gas phase ALD method of approach might improve the cathode catalyst performance by allowing the controlled deposition of uniformly distributed Pt nanoparticles on a WO_X nanopowder support. Solution-based methods for depositing platinum particles yield cathode materials that have so far not demonstrated long term stability because the platinum agglomerates during cycling, another aspect needing improvement.[91, 92] Because typical metal oxides do not closely match platinum surface free energy, there is an expected period during the initial cycling in which platinum forms clusters or islands on the metal oxide surface, and then as the islands grow they eventually merge into conformal film, with many examples supporting particle formation rather than conformal films.[93, 70, 94, 95]

There are also signs that conformally deposited platinum may a good option, using core-shell structures to make the most use of the platinum catalyst, and there are other studies examining platinum alloys as efficient catalysts. In all of these cases, using as little platinum as possible to achieve high catalytic activity calls for the best use of the platinum surface, and in fuel cells, stability will be

important.

In this study, TiO_2 nanopowder serves as a model substrate material for studying the nucleation and growth of ALD Pt through in-situ FTIR. The analysis is expected to give information to optimize the growth of ALD Pt on WO_X nanopowder. Tungsten oxide easily reduces during the Pt ALD reaction, which causes absorption of the IR beam and makes it a difficult material to study Pt nucleation and growth with in situ transmission FTIR. TiO_2 shares some acidity and stability properties with tungsten oxide, and does not reduce as easily, and was therefore chosen as a proxy substrate for FTIR studies. There is also a chance that doped titanium oxide could be used as cathode catalyst support, though this was not tested in this work.[96, 97, 98] Transmission electron microscopy (TEM) helped characterize the platinum in the Pt/WO_X samples. As mentioned, the chosen precursors of $Pt(hfac)_2$ and formaldehyde solution are expected to include a long nucleation period. The straightforward reaction between these would be the reduction of platinum II to platinum metal, per Reaction 1, as in the following could be expected from the reaction of $Pt(hfac)_2$ and formalin (formaldehyde in water, with methanol to deter polymerization).

$$Pt(hfac)_2 + H_2CO + H_2O \rightarrow Pt + 2HfacH + HCOOH$$

Reaction 1. The main focus of this reaction is the reduction of platinum II to platinum metal, and the oxidation of formaldehyde. There is the possibility that the methanol contributes to the reduction, since methanol is a mildly active reducing agent. After demonstrating similar growth of Pt ALD on WO_X, further studies in scaling up the reaction quanties of powder were carried out.

4.2 Experimental Methods

FTIR reactor. The reactor is a cold wall viscous flow reactor that holds an independently heated sample grid. Transmission FTIR is done through powder samples, using CsI windows on the reactor, which are protected by gate valves during the reaction. The powders were pressed into a

grid with 0.01 inch pores in tungsten grids from TechEtch. The powders used in these experiments were either titanium oxide or tungsten oxide, and both were loaded into the reactor and purged with gaseous nitrogen for at least an hour prior to being cleaned by heating to above 350 °C. The as received titanium dioxide nanopowder from Nanophase Technologies Corporation consisted of about 80 % anatase crystal and 20 % rutile. The as received tungsten oxide from the National Renewable Energy Laboratory, grown with hotwire chemical vapor deposition using oxygen flow in a furnace, demonstrated multiple oxidation states under even visual inspection.[99] The samples used for the results shown here did not appear fully oxidized, being a dark blue rather than WO_3 green-yellow. Therefore, this tungsten oxide of unknown oxidation state is designated WO_X.

Fourier Transform Infrared spectroscopy (FTIR) experiments were conducted in a viscous flow, warm wall reactor chamber that has been described previously.[46] Precursors were entrained in a flow of nitrogen gas (Airgas UHP grade) and dosed into the reactor holding the reactive surface, nanoparticles in a sample grid. Using two URS-40 mass flow controllers, the nitrogen flow was kept at 1.25 Torr, a flow of 200 sccm. The sample grid was made using a tungsten mesh with 100 holes per inch, and the titanium oxide or tungsten oxide powders were mechanically pressed in. Using powder gives high surface area, tens of meter^2/gram, increasing the FTIR signal to noise considerably compared to a flat sample.

The walls of the reactor were kept at about 130 °C, and the grid could go over 1100 °C K using a Love Controls 16A temperature controller. A type K thermocouple was used to sense the temperature, and the resistive heating current was supplied by a Hewlett-Packard 6268B Power supply.

The results shown for the FTIR section were deposited on substrate particles that were loaded into the reactor, allowed equilibration time, and flashed briefly to high temperature (500 °C for titanium oxide, 350 °C for tungsten oxide) to remove adventitious carbon.

The reactor was constantly pumped with an Alcatel 2010 C1 mechanical pump, and the waste stream gas was monitored with an MKS baratron. The FTIR used is a Nicolet model Magna IR 560 and the beam passed through CsI windows that were protected from chemical exposure within

Label	Vibration	Frequency (cm^{-1})	References
1	CO on oxidized Pt/TiO_2	2100	[100, 101, 102, 103, 104]
2	C=C stretch	1640	[105]
3	C=O stretch	1625	[105]
4	Pt CO stretch and CH bend	1590	[106, 107]
5	CO stretch and CH bend	1550	[108]
6	C=C stretch	1530	[108]
7	CH bend and C=C stretch	1440	[105]
8	C-C stretch and C-F stretch	1360	[105, 109]
9	CF_3 stretch	1250	[105, 109]
10	CFburrower3 stretch	1230	[105, 109]
11	CH bend	1180	[105, 109]
12	CH stretch	2942	[110]
13	CH stretch	2837	[110]
14	COO stretch of formate	1550	[110, 111, 112]
15	COO stretch of formate	1370	[110, 111, 112]
16	CO stretch	1026	[110]

Table 4.1: FTIR frequency assignments for $Pt(hfac)_2$, hfacH, and formalin on TiO_2.

the reactor by MDC gate valves during dosing. That way deposition/condensation on the windows was avoided. Precursors were dosed using Labview, allowing consistently timed openings of pneumatic valves. The detector was a mercury cadmium telluride (MCT-B) Nicolet semiconductor that was cooled to -200 °C with liquid nitrogen before experimentation began. The experimental FTIR set-up has been described previously.[2] The precursors for the platinum growth were platinum (II) hexafluoroacetylacetonate (98 % pure from Strem Chemicals Inc.), trimethylplatinum IV methylcyclopentadienyl (99 % pure Strem Chemicals Inc.), and formalin (37 % formaldehyde and 10 % methanol in water from Sigma-Aldrich). Both were transferred to dosing vessels and degassed before deposition experiments. In order to ensure appreciable vapor pressure, platinum (II) hexafluoroacetylacetonate was heated to 80 °C during the experiments, while formalin was kept at room temperature.

X-ray photoelectron spectroscopy (XPS) was used initially to confirm that the platinum in the Pt/WO_X was metallic. X-ray photoelectron spectra (XPS) were taken with a PHI 5600 X-ray photoelectron spectrometer using a monochromatic Al source. The depth profile was carried out using argon sputtering.

The TEM was performed using an FEI Tecnai ST 30 TEM instrument with standard bright field electron diffraction contrast imaging operating at 200 kV at the National Renewable Energy Laboratory.

Static rotary ALD reactor. The WO_X nanopowder substrate was grown using hotwire chemical vapor deposition (HWCVD) and supplied by the National Renewable Energy Laboratory in Golden, Colorado. The WO_X nanopowder had a BET surface area of 50 m^2/gWO_X. The as-received HWCVD WO_X nanopowder was contained in either one of two cylindrical stainless steel (SS) sample holders. The closed-porous cylinder was made of 316L SS and consisted of 10 M diameter pores. The open-ended cylinder consisted of solid 316 SS walls and had an open end. Both cylinders had dimensions of 1.7 cm x 7.1 cm. The WO_X samples were transferred to a custom static ALD reactor.[113] In all experiments, the samples were rotated using a magnetically coupled motor attached through the rear of the ALD reactor. The rotation speed was controlled using a

BK Precision DC power supply, and maintained at a 12- 14 V/0.16 A output. Rotation speed was determined by finding the maximum speed with which the sample could rotate without spilling into the reactor chamber.

Prior to Pt ALD, the WO_x samples were heated under vacuum at 180 °C for two hours. Platinum ALD was carried out using two separate chemistries. Initial experiments utilized alternating static exposures of $Pt(hfac)_2$ (98% (99.9%-Pt)) and formalin at 200 °C, with ultrahigh purity argon purge gas (Airgas). The $Pt(hfac)_2$ precursor was maintained at 80 °C in a stainless steel bubbler. Later experiments used alternating static exposures of $Me_3PtMeCp$ (STREM Chemicals, 99%) and ultrahigh purity O_2 (Airgas,) at 200 °C. The O_2 was used as a co-reactant as well as the purge gas. The Me_3Pt MeCp precursor was maintained at room temperature in a glass bubbler.

$Pt(hfac)_2$ chemistry. The Pt ALD reaction sequence is as follows: a $Pt(hfac)_2$ dose to roughly 10 mTorr, a static dose for 60 s, evacuation of excess $Pt(hfac)_2$ and reaction products, with this sequence followed for 12 minicycles. The next stage is Ar purge, with doses of 1.0 Torr held in a static dose for 10 s befor evacuation of the Ar purge. Then, formalin is introduced, increased to a 2.0 Torr level for static dosing for 120 s and followed by evacuation of excess formalin and reaction products. Lastly, purging took place with a dose of Ar to 1.0 Torr in a static dose for 10 s and then evacuation of Ar. This entire sequence constitutes one Pt ALD reaction cycle using $Pt(hfac)_2$. The Pt ALD was carried out at 200 °C.

The $Me_3PtMeCp$ and O_2 ALD took place in the static rotary reactor. One Pt ALD reaction sequence is as follows: $Me_3PtMeCp$ was dosed to roughly 10 mTorr as a static dose for 80 s, then evacuation of excess $Me_3PtMeCp$ and reaction products took place, and this initial sequence is followed for 8 mincycles. Then a purge with O_2 purge to 100 mTorr happened as a static step for 5 s, concluding with evacuation of O_2. Next, introduction of 2.0 Torr of O_2 took place as a static dose for 180 s followed by evacuation of excess O_2 and reaction products. The cycle concluded with a purge of O_2 to 100 mTorr as a static dose for 5 s with and then evacuation of O_2. This entire sequence constitutes one Pt ALD reaction cycle using $Me_3PtMeCp$. The Pt ALD was carried out at 200 °C.

The weight percent of Pt metal in each sample was determined using inductively coupled plasma optical emission spectroscopy (ICP-OES). The particle size, dispersion, and morphology were estimated using transmission electron microscopy (TEM). The Pt/WO_x samples were analyzed for mass activity in the oxygenreduction reaction (ORR) through rotating disk electrode (RDE) experiments. The mass activity was calculated from the electrochemical surface area and specific activity. Electrochemical surface area of the Pt/WO_x was calculated from the measured peaks of hydrogen underpotential deposition. The specific activity was determined from cyclic voltammograms using a RDE in perchloric acid. The product of the electrochemical surface area and the specific activity results in the mass activity in mA/ mgPt.

4.3 Results and Discussion

4.3.1 *in situ* FTIR characterization of early reactions

The chosen precursors, $Pt(hfac)_2$ and formalin are desirable because the bulky ligand is expected to impede full surface coverage during the platinum half-cycle. Then platinum binds more readily to itself than it does to most metal oxides, so wetting should be difficult and particle formation encouraged. In addition, the reaction during palladium deposition by Goldstein et al. on Al_2O_3 included evidence of dissociative chemisorption of $Pd(hfac)_2$ on aluminum oxide.[77] The fluorinated resonant diketone-enol ligand of the platinum precursor readily attaches to metal centers. Platinum theoretically will attach to the titanium and oxygen of a titanium oxide surface.[93] The reduction of platinum by formaldehyde would cause the removal of the ligands attached to platinum, but do little to remove the ligands sitting on the titanium dioxide surface, leaving sites with a combination of metallic platinum and hfac ligands.

Figure 4.1 shows the TiO_2 after near-saturation with either the platinum precursor, or with the ligand molecule sans platinum for comparison. A TiO_2 surface was coated with hfacH in Figure 4.1(a), and another TiO_2 surface coated with $Pt(hfac)_2$ in 4.1(b). In both cases the initial TiO_2

spectrum was subtracted off to show only the changes, where positive absorbance features meant addition, and negative features meant subtraction. Both spectra include the hfac ligand on TiO_2, and many of the assignments are based off of $Pt(hfac)_2$ on copper.[106]

To identify the infra-red absorption peaks associated with platinum, FTIR scans of surface bound hydrogenated ligand, and $Pt(hfac)_2$, gave the contrasting spectra seen in Figure 4.1. A spectrum of titanium oxide powder sample dosed with hexafluoroacetylacetone (hfacH) and the spectrum of a separate titanium oxide powder sample dosed with $Pt(hfac)_2$ made the identification of ligand associated with platinum clear. They look very similar, and the differences are key to identifying the presence of platinum. The assignments are summarized in Table 4.1. The difference is primarily in the carbonyl stretch region, since these frequencies are sensitive to their environment. Bonding to metals influences the electron density of the oxygen carbon bond, and can be quite distinctive between certain metals. The relatively strong peak at 1591 cm^{-1} in the platinum hfac spectrum and not the hfacH spectrum was assigned to CO stretch and CH bend according to the Crane et al. list of assignments.[107, 106] Additional support comes from the isotope substitution of oxygen in the work of Pinchas.[108, 114]. It is distinctively indicative of the platinum association with the ligand. The oxygen-carbon bonds in the ligand could be a mixture of double and single bond character, with resonance especially likely among the two oxygen and three carbon atoms. The other stretches primarily correspond with intact ligand on the surface, such as the C=C stretch at 1640 cm^{-1}, the combination band of C-H + C=C at 1440 cm^{-1}, the combination band of C-C + C-F stretch at 1360 cm^{-1}, the CF_3 stretch at 1250 cm^{-1}, and the C-H bend at 1180 cm^{-1}.[105] In addition, the stretch seen in the 2100 cm^{-1} viscinity corresponds to a triply bonded carbon with oxygen, such as carbon monoxide on platinum.[80, 100, 115, 116]. The Girolami study suggests the possibility of a related ketenylidene species from the breakdown of hfac ligand on copper. It was interesting to see carbon monoxide/ketylidene on platinum appear even before a reduction step happened. The presence of platinum presumably changes the ligand breakdown pathways, as would be expected from an effective catalyst, even at the early stage of the deposition.

For many ALD chemistries, the starting nucleation reactions take place at hydroxyl sites on the sub-

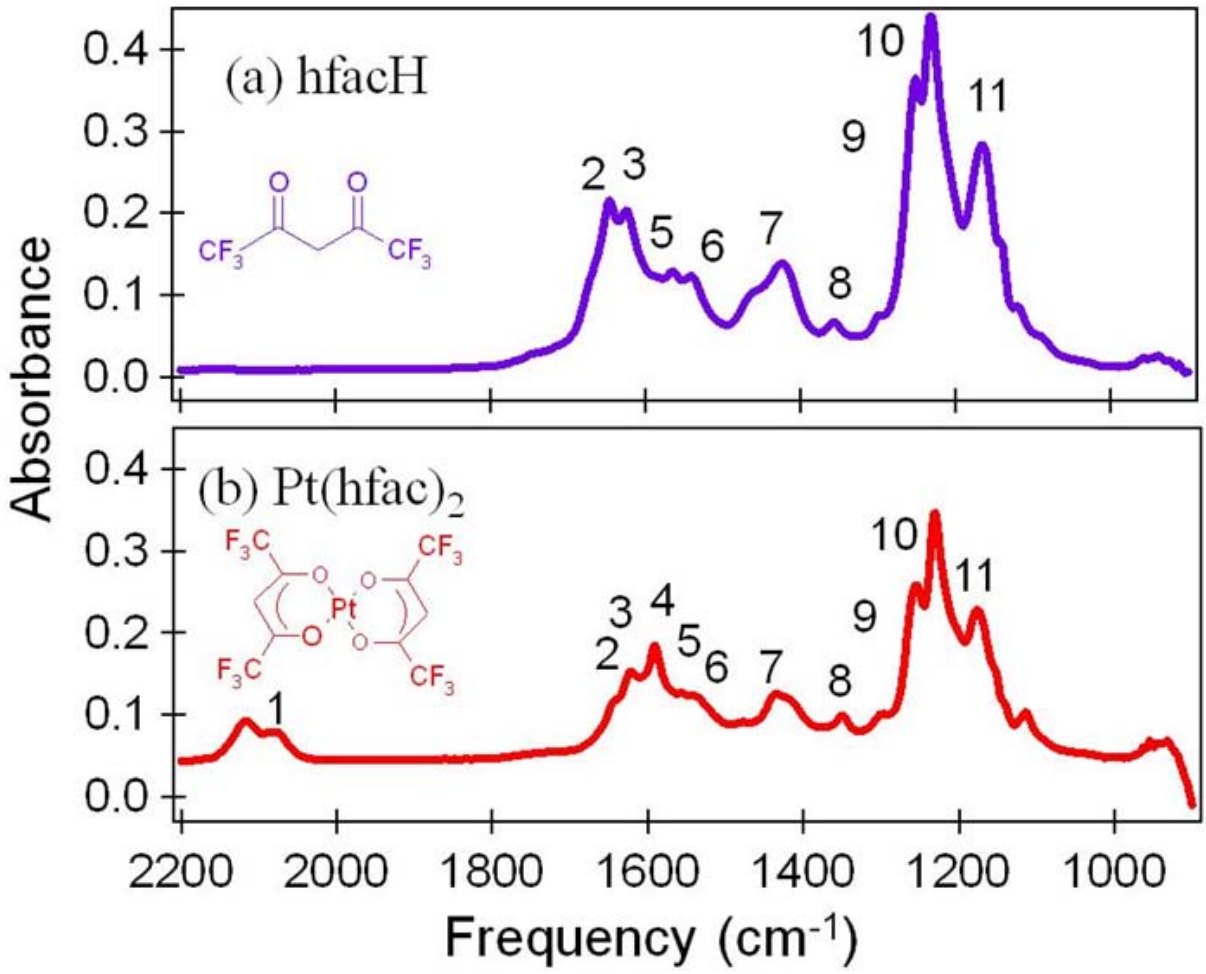

Figure 4.1: FTIR difference spectra of $Pt(hfac)_2$ (bottom) and hexafluoroacetylacetone (hfacH) (top) on TiO_2, with TiO_2 features subtracted to show only the reacting species, deposited at 200 °C. The peak assignments are listed in Table 4.1.

strate surface. Hydroxyl coverage of a starting surface therefore relates directly to initial reactive surface sites for a great many chemistries, with several consequences.[52] Increased recombination and water desorption with temperature causes fewer reactive sites on most substrates. Also, if the hydroxyl groups are close enough to one another to hydrogen bond[117], or if hydrogen bonding can occur with the surface, the hydroxyl is less likely to react, as seen by the so called "free" non hydrogen-bonded hydroxyls reacting more readily in previous FTIR studies.[48] In the case of platinum deposition, however, the presence or absence of surface hydroxyls seemed to have little influence on the precursor reaction with the surface. If hydroxyls were present, $Pt(hfac)_2$ exposure led to surface coverage, but if not, the surface coverage with $Pt(hfac)_2$ was still accomplished.

The examination of the spectra for evidence of associative or dissociative adsorption includes a close look at the hydroxyl region. If chemisorption were to take place, the reaction likely would involve the loss of a hydrogen cation from the hfacH, leading to hydroxyl formation with a surface oxygen of TiO_2, or water formation in combination with a surface hydroxyl. Seeing such a change would be easier with low starting hydroxyl coverage of the TiO_2 than high coverage. Increased recombination and water desorption with increasing temperature causes fewer reactive sites on most substrates. When hfacH was dosed onto a TiO_2 surface with very low hydroxyl coverage, almost no hydroxyl change was observed (Figure 4.2), suggesting molecular absorption of the ligand on the surface. When the TiO_2 surface started with many hydroxyls, the change upon dosing with hfacH was almost negligible, showing no discernible loss or gain, and merely showing a tiny red-shift in some. The red shift, subtle enough to be in question, does suggest the surrounding of the hydroxyl groups with dielectric molecules. In the case of platinum deposition, the presence or absence of surface hydroxyls seemed to have little influence on the precursor reaction with the surface. In examining the region of hydroxyls upon dosing $Pt(hfac)_2$ onto a TiO_2 surface with very low hydroxyl coverage (Figure 4.2), a few of the hydroxyls reacted, and the negative feature shows their loss. If more hydroxyls were present, a larger amount reacted with $Pt(hfac)_2$, but in either situation a similar surface coverage with $Pt(hfac)_2$ was accomplished, and if many hydroxyls were

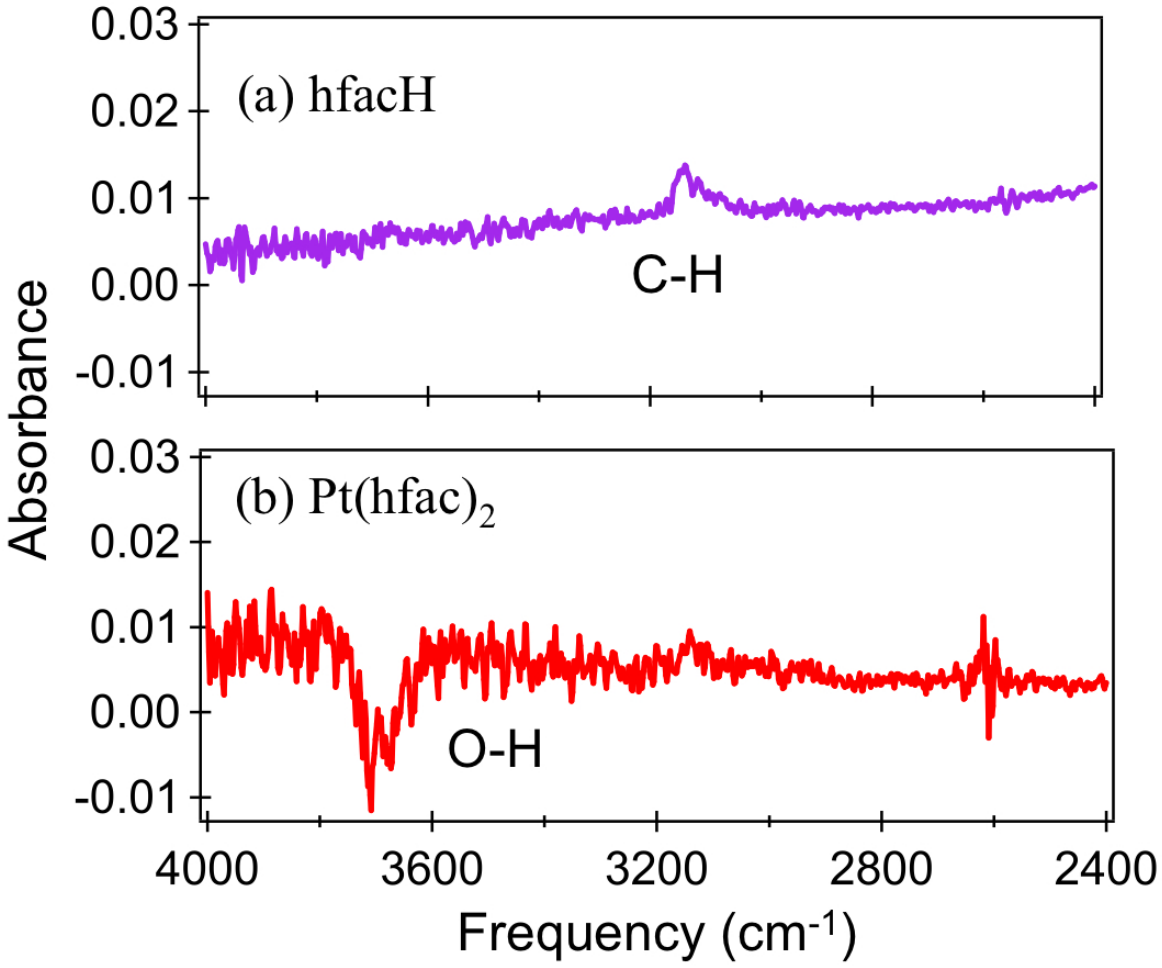

Figure 4.2: These spectra examine a higher vibrational region of reacted TiO_2 surfaces than shown in Figure 4.1. They emphasize the change in hydroxyl coverage after reaction at 200 °C of $Pt(hfac)_2$ (bottom) and hexafluoroacetylacetone (hfacH) (top) on TiO_2, with TiO_2 features subtracted.

present, not all of them reacted. This suggests more than one attachment method for the $Pt(hfac)_2$ with the surface, and the intact nature of the ligand in both cases also makes molecular adsorption a possibility.

Dosing $Pt(hfac)_2$ onto the TiO_2 powder fulfilled step one in the deposition process. During the first two cycles of ALD film growth shown in Figure 4.3, all spectra are referenced back to the initial TiO_2 surface, in order to examine the additions and removals with the precursor doses. The spectrum in Figure4.3(a) was taken after exposure to $Pt(hfac)_2$, spectrum (b) after formalin, spectrum (c) after the second exposure to $Pt(hfac)_2$, and spectrum (d) after the second exposure to formalin. Some changes become apparent after the first cycle. The first cycle involves dosing the $Pt(hfac)_2$ onto TiO_2, and from the area under the peaks, it can be seen that more is deposited on the first cycle than in the second cycle. Most of the sites are filled or blocked in the first step, and then formalin is expected to reduce the platinum to metal, and that causes some ligands to leave the surface platinum and the surface sites become a combination of platinum metal centers and hfac ligands, blocking some sites on the TiO_2 from further reaction. Also of note, on the first step, as before, there is a clear indication that platinum (II) is associated with the hfac, by the peak at 1591 cm^{-1}. In Parmeter's FTIR examination of hfacH and Cu(hfac)burrower2 on platinum (111), that peak is not present to a significant degree, meaning that hfac on metallic platinum does not appear to influence the carbonyl stretch frequency the same as the oxidized platinum.[118] After formalin dosing, the peaks appearing at 1360 and 1570 cm^{-1} indicate formation of formate on the surface, a process observed previously by Busca [111, 112]. Formalin dosing also lessens the CF_3 stretching vibrations, and increases the carbon monoxide on platinum absorbance. This suggests that some ligands are dissociating from platinum during the half-cycle.

The second cycle, Figures 4.3(c) and (d), not only shows smaller absorbance changes than the first cycle, but a significant increase in the frequency associated with carbon monoxide on platinum. The absence of the 1590 cm^{-1} feature in Figure 4.3 gives evidence that the $Pt(hfac)_2$ reaction products change after the surface has been exposed to an ALD cycle. The carbon monoxide increase in Figure 4.3(d) is the presumed result of the reduction of adsorbed $Pt(hfac)_2$. As will be further discussed,

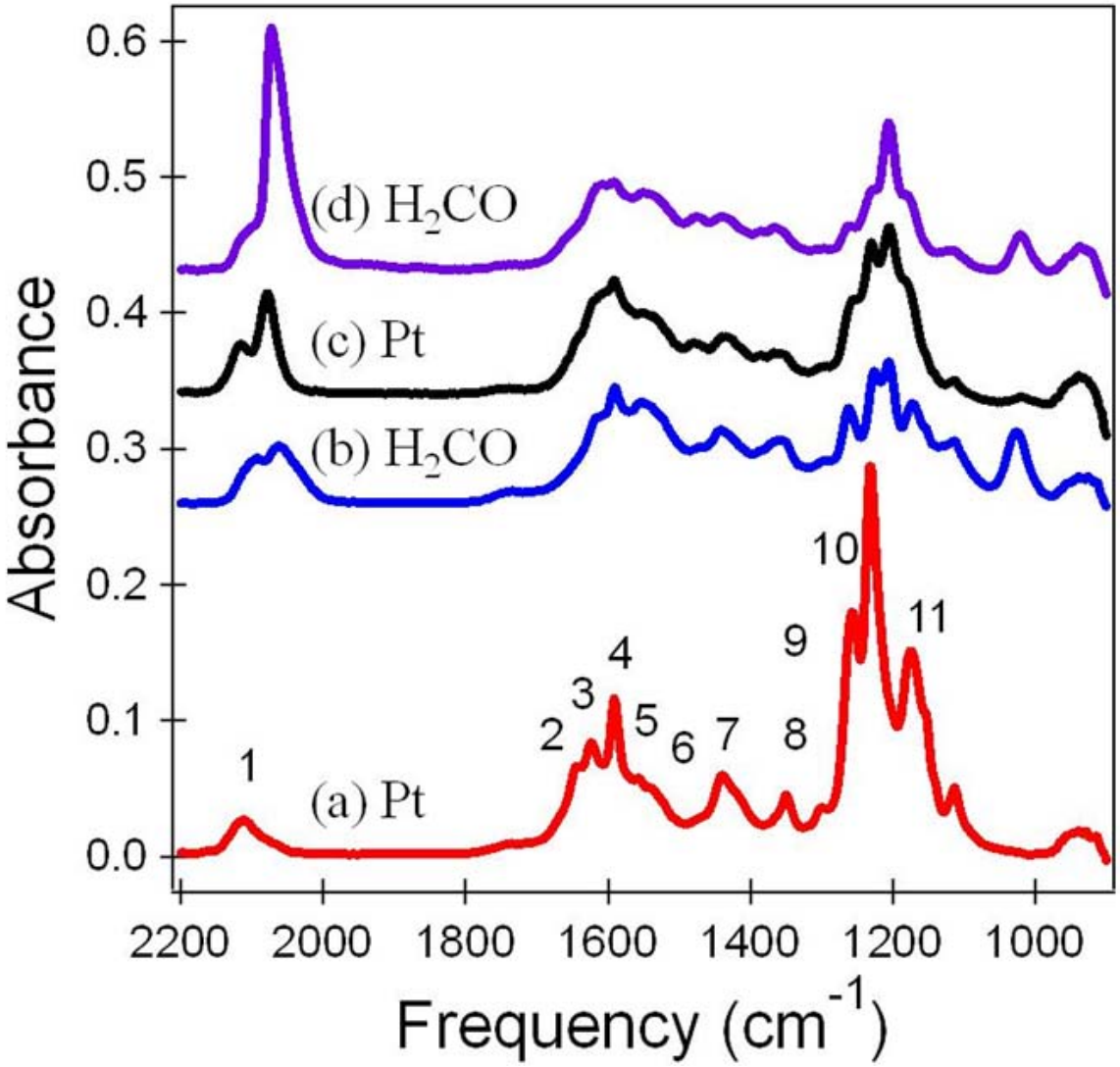

Figure 4.3: The first two cycles of $Pt(hfac)_2$ and formalin on TiO_2, deposited at 200 °C, all referenced back to the TiO_2 surface. Formalin peak assignments are in Table 4.1. The spectra are after (a) first $Pt(hfac)_2$ exposure, (b) first formalin exposure, (c) second $Pt(hfac)_2$ exposure, (d) second formalin exposure.

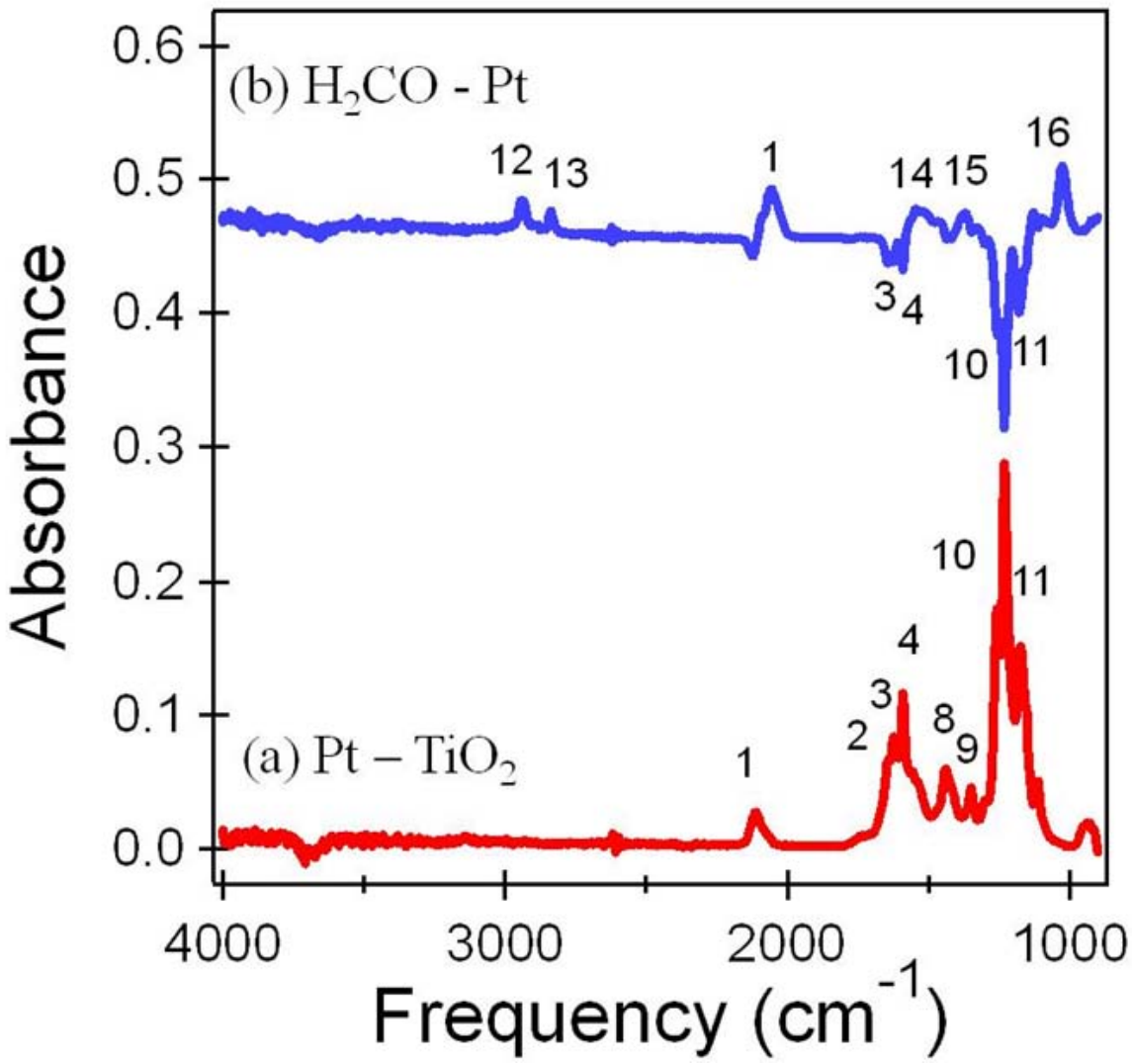

Figure 4.4: Spectra from cycle two of Pt ALD at 200 °C are shown. The platinum II hexafluoroacetylacetonate spectrum is referenced back to the TiO_2, and the formalin is referenced back to the platinum II hexafluoroacetylacetonate rather than the TiO_2. The peak assignments are listed in Table 4.1.

the FTIR evidence and previous literature suggests that hfac ligands partially decompose on the surface. Girolami observed decompostion of $Cu(hfac)_2$ on copper crystals, Leo hfacH on silicon crystals, and Zaera observed $Cu(acac)_2$ decomposition on copper and nickel crystals.[115, 114, 119] Not unexpectedly, the composition of the surface influenced the ligand breakdown. As more platinum metal forms on the TiO_2, the mechanism probably shifts slightly, since platinum assists with the breakdown of hfac bonds and could be encouraging the reduction of platinum ions. The peaks in the 2100 cm^{-1} region likely correspond with carbon monoxide attached to platinum. The changes due to the formaldehyde and methanol of the formalin solution are thrown into sharp relief by subtracting off the immediately preceding $Pt(hfac)_2$ coated TiO_2 surface from the first formalin half-cycle. Figure 4.4 includes the 4000-900 cm^{-1} range, (a) showing the first $Pt(hfac)_2$ exposure on TiO_2 with TiO_2 subtracted, and (b) the successive formalin dose with the TiO_2 $Pt(hfac)_2$ surface subtracted. The assignments in Table 4.1 include the peaks appearing at 1370 and 1550 cm^{-1} which, as mentioned, could indicate formate on the TiO_2 surface.[111, 112] In agreement with the Kiss paper [110], C-H 2942 and 2837 cm^{-1} stretches and CO stretches 1026 cm^{-1} were observed. Formaldehyde oxidizes on TiO_2 and on Pt/TiO_2 at the temperatures examined.[120, 110] With Pt/TiO_2 the formation of formic acid and formate, carbon monoxide, and H_2 have been observed with FTIR and mass spectrometry.[110, 121] The formalin acts as a reducer by becoming oxidized in the presence of TiO_2 and platinum.

The platinum II hexafluoroacetylacetonate reaction was carried out at substrate temperatures ranging from 150-250 °C. At the high end, there was concern that platinum atom mobility on the surface would encourage agglomeration and Ostwald ripening[122], while at the low end, the slow growth rate of the platinum was a problem. To balance between deposition speed and control, 200 °C was the chosen temperature for the ALD samples grown for characterization.

In Figure 4.5, the sample examined with transmission electron microscopy shows the result of 150 cycles of Pt ALD on TiO_2 powder at 200 °C. The contrast and magnification show that the denser platinum particles dispersed over the surface of the lighter TiO_2 powder. The magnification level is sufficient to show crystalline lattice fringes for the titanium dioxide. The appearance of the

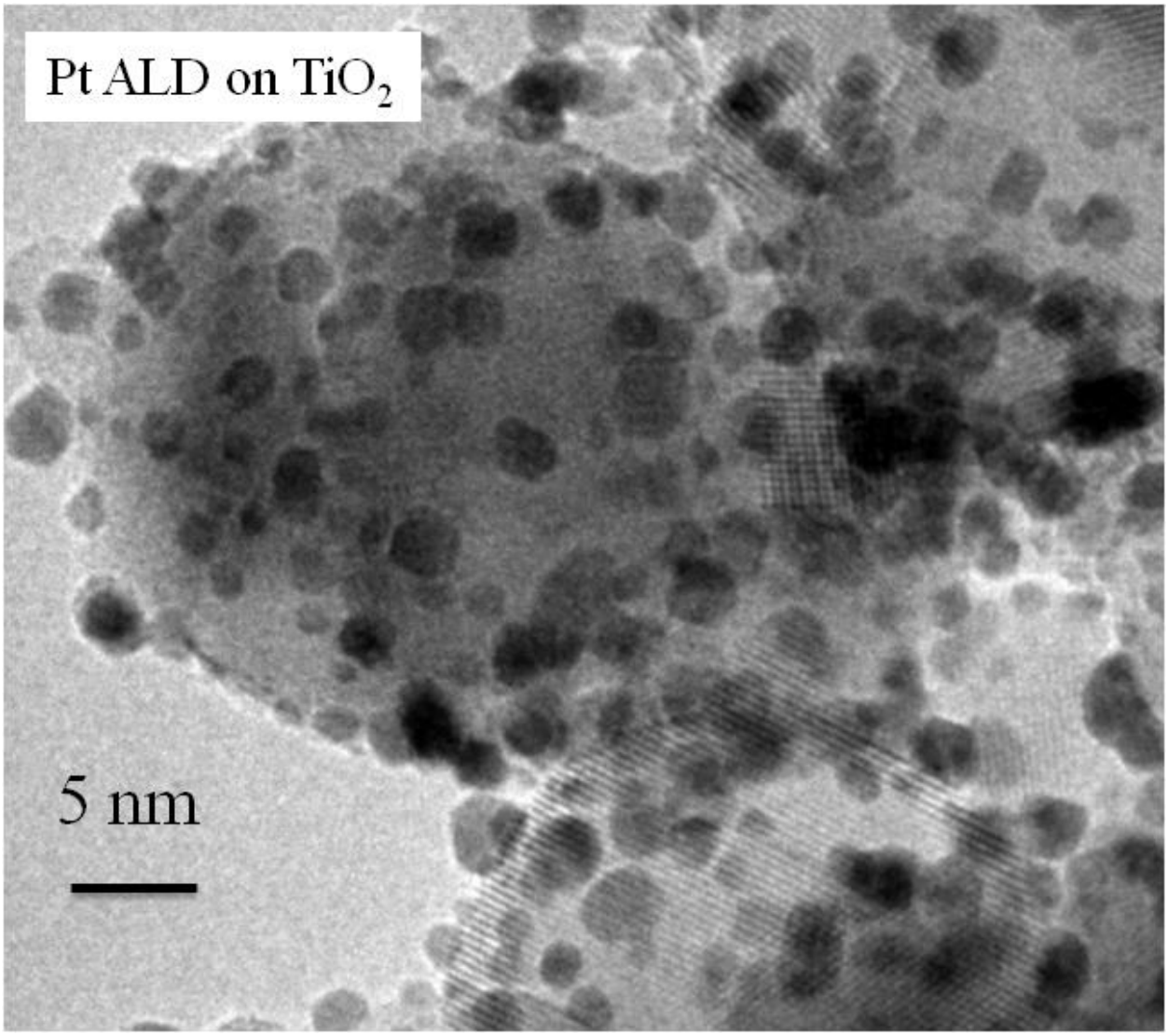

Figure 4.5: The TEM shows TiO_2 treated with 150 cycles of Pt ALD at 200 °C. The denser platinum particles are in contrast to the less dense TiO_2 powder.

platinum particles supports but does not confirm a regular structure, since there are vertices where the directionality abruptly changes, which is suggestive of crystal facets. At diameters around two and three nanometers, the number of platinum atoms is not very high per particle, but a two nm diameter particle has on the order of 280 atoms, and a 3 nm particle on the order of 940 atoms. It is feasible that a mixture of amorphous and crystalline character is present, and expected that the substrate-platinum interface is playing a role in determining the platinum structure. A sample of Pt grown on TiO_2 for over 400 cycles was analyzed using XPS, and showed 95 wt% Pt present after sputtering through the adventiteous carbon surface, leading to the belief that the platinum is metallic.

Figure 4.6 provides the results of probing whether or not the half-reactions self limit. The second cycle of platinum deposition on a TiO_2 substrate provided data on whether the reactants would keep reacting with themselves. After each small dose of $Pt(hfac)_2$, the area of the added peaks calculated in the resulting FTIR spectrum tracked the change or lack thereof. The graph shows the normalized change in the peak area of the added surface species, and as expected, the early doses add relatively large amounts, while the later doses added far less. Initially the surface displays many open sites, and then once reacted with the precursor, they become inert to further reaction, and even the remaining open sites become more difficult to react with since they are both scarcer and more obscured by nearby precursor. Once most sites fill up, the addition of further precursor produces diminishing returns, and a typical platinum process involves dosing almost to saturation but not 100 percent. The formalin reaction could be watched either by following removed hfac ligand peaks, or by the added peaks of the formaldehyde and methanol and water. In Figure 4.6 the CF_3 stretches and CH bend are followed (modes 9-11 in 4.1).

Figure 4.3 reveals that there is a large increase in the absorbance for the CO stretching vibrations on the Pt nanoparticles during the 2nd formalin exposure. Figure 4.7 shows the evolution of the integrated absorbance for the CO stretching vibrations between 1990 and 2190 cm^{-1} during the 2nd formalin exposure during Pt ALD. The integrated absorbance for the CO stretching vibrations

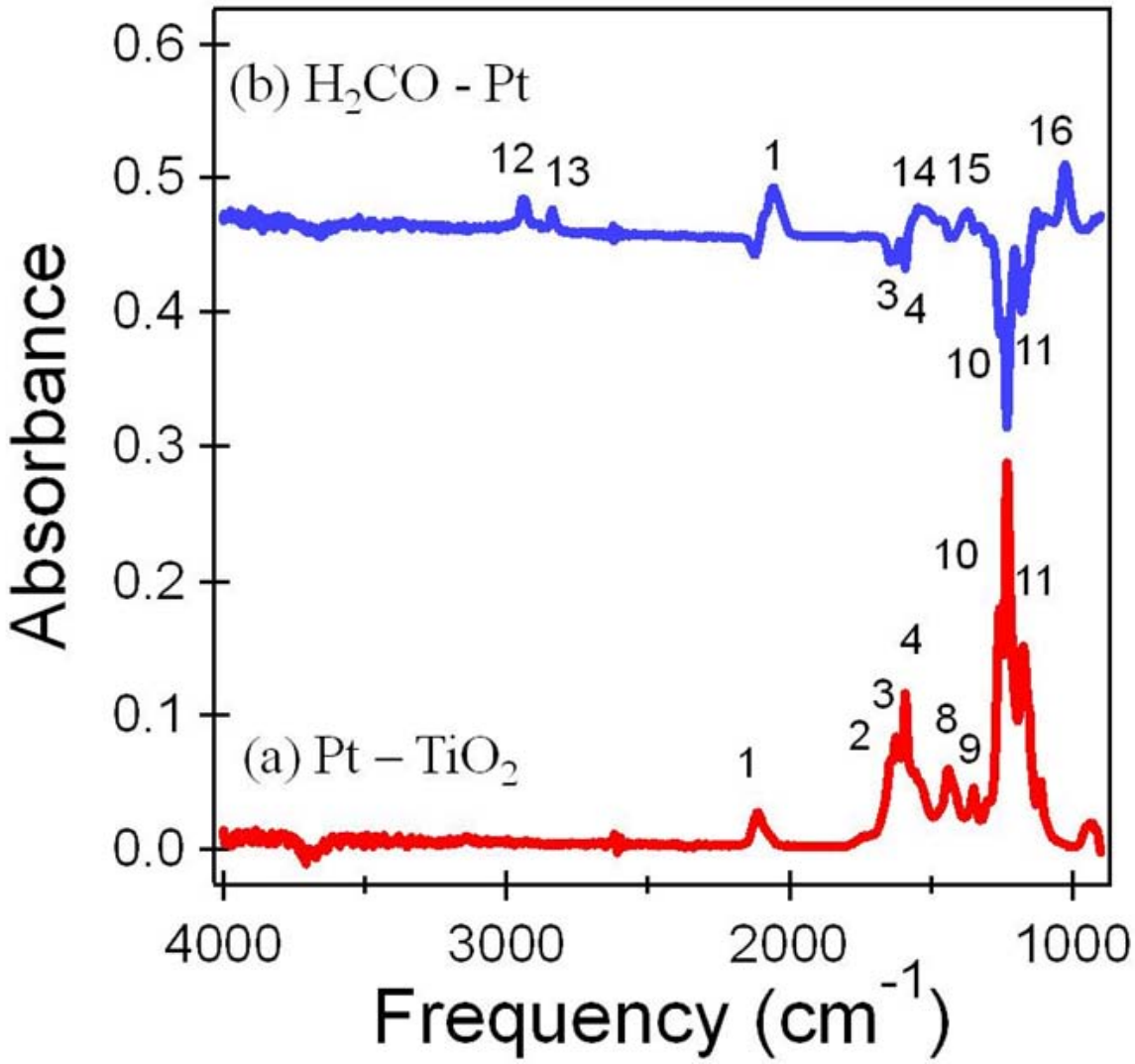

Figure 4.6: Check of self-limiting behavior of each half of the Pt ALD cycle. The FTIR spectra were recorded after each minidose of the precursor during the second reaction cycle on a TiO_2 surface at 200 °C. Most of the surface reactions happen on the initial dosing, and as more $Pt(hfac)_2$ is added, the addition to the surface decreases, though does not completely stop. The formalin reaction is also followed by taking the integrated absorbance of the CF_3 stretch and CH bend (modes 9, 10, and 11 in Table 4.1), and those leave with time as well as formalin exposure, as shown in Figures 4.11 and 4.12.

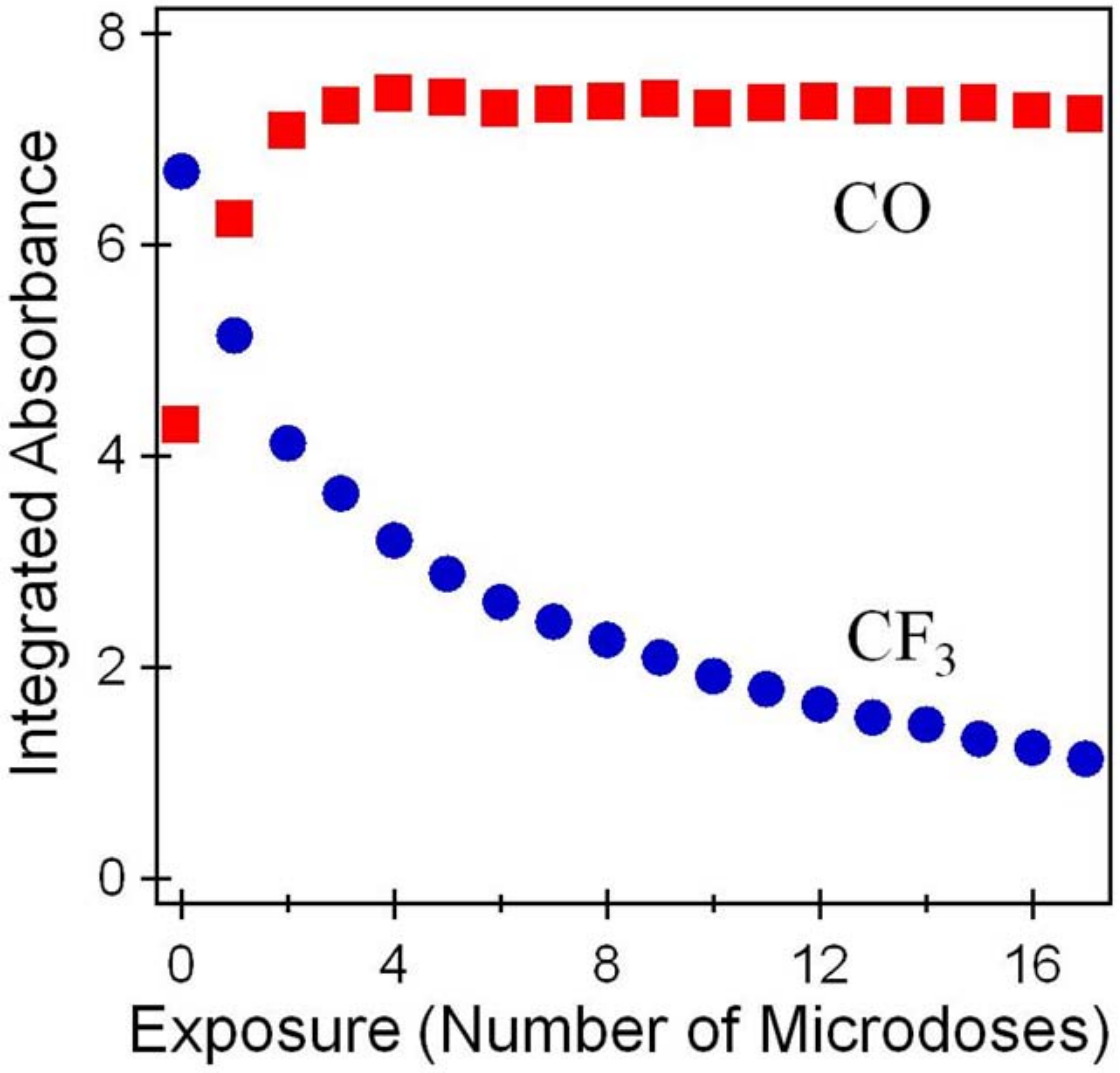

Figure 4.7: Same formalin uptake as Figure 4.6, while also examining the integrated absorbance of carbon monoxide (mode 1 in Table 4.1) during the 200 °C experiment. The rise in carbon monoxide suggests reduction of positive platinum, as otherwise the hfac ligand instead of carbon monoxide would probably be associated with the platinum centers.

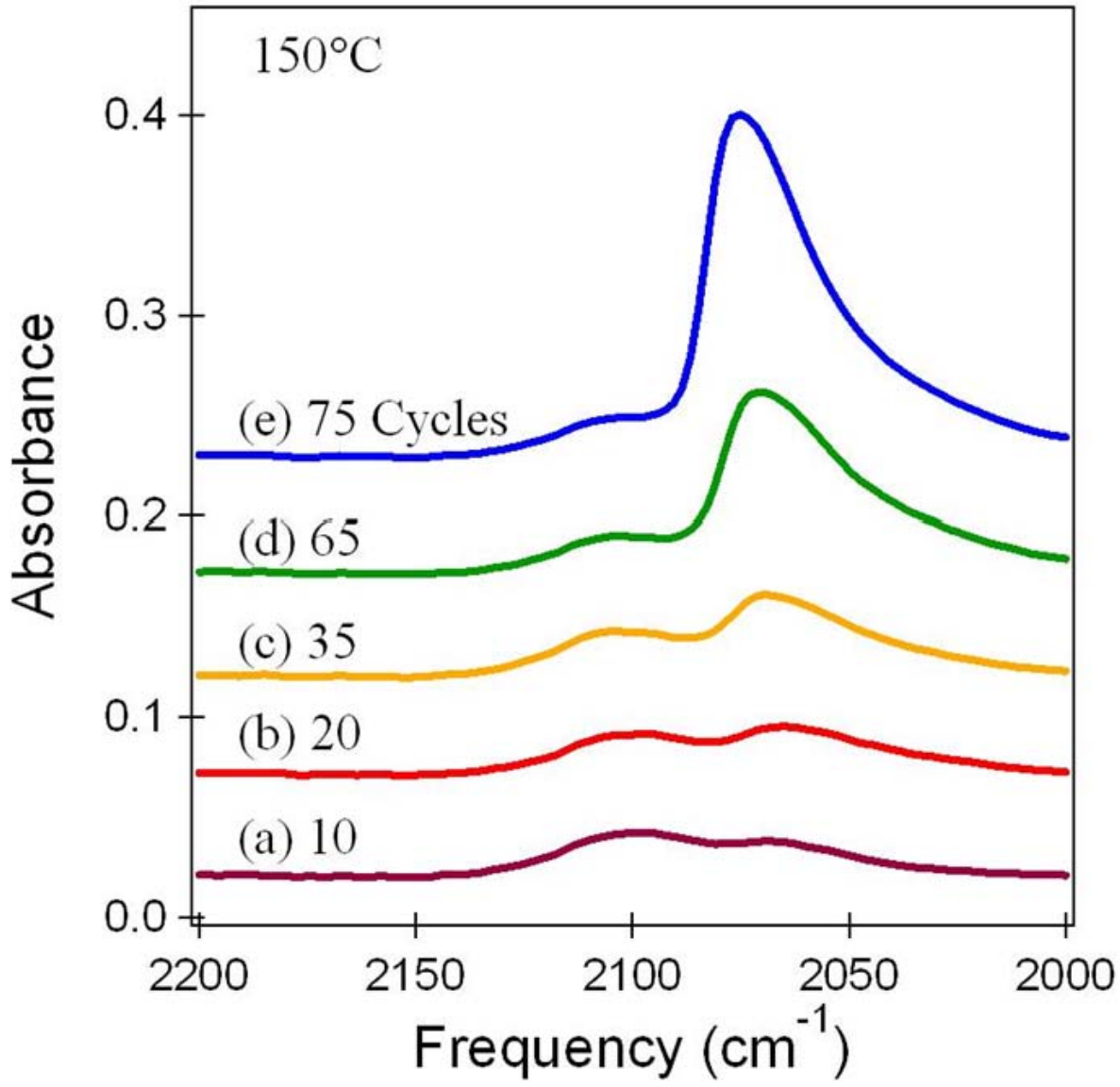

Figure 4.8: FTIR difference spectra in the carbon monoxide stretching region after (a) 10, (b) 20, (c) 35, (d) 65, and (e) 75 Pt ALD cycles on TiO_2 powders at 150 °C.

increases dramatically during the early stages of the formalin exposure. The integrated absorbance for the CO stretching vibrations is then relatively constant while the integrated absorbance of the CF_3 stretching vibrations is still reducing versus formalin exposure.

The results in Figure 4.7 suggest that Pt atoms are released quickly from $Pt(hfac)_2$ adsorbed species during formalin reduction. These Pt atoms are presumably adding to existing Pt nanoparticles or forming new Pt nanoparticles. The formalin exposure, and perhaps time, continue to remove hfac species on the TiO_2 substrate that contain CF_3 stretching vibrations. These hfac species on the TiO_2 substrate, however, are not associated with additional Pt atoms. Figure 4.8 shows the absorbance for the carbon monoxide stretching vibrations on the Pt nanoparticles versus larger numbers of Pt ALD cycles at 150 °CC. The temperature was reduced to 150 °C to avoid desorption and decomposition of hfac ligands on the surface. Figure 4.8(a) reveals two broad peaks centered at 2097 cm^{-1} and 2065 cm^{-1} after 10 Pt ALD cycles. The peak at 2065 cm^{-1} then grows progressively after 20, 35, 65 and 75 Pt ALD cycles as displayed in Figures 4.8(b), 4.8(c), 4.8(d) and 4.8(e), respectively. For this set of Pt ALD cycles at 150 °C, TMA exposures were applied after 10, 20, 35, 45 and 70 Pt ALD cycles to remove the hfac species from the surface.[77] When spectra were recorded, they were collected prior to the TMA exposures. The CO stretching vibration at 2065 cm^{-1} after 10 Pt ALD cycles shifts slightly to higher frequencies as this absorbance feature grows versus Pt ALD cycles. The CO stretching vibration is observed at 2070 cm^{-1} after 35 Pt ALD cycles and 2073 cm^{-1} after 75 Pt ALD cycles. This CO stretching frequency corresponds closely with the frequency of CO on on-top sites on stepped or defective Pt(111) surfaces.[123, 124] This assignment is reasonable because small Pt nanoparticles can not maintain large Pt(111) terraces. In contrast, CO stretching vibrations on on-top sites on Pt(111) single-crystal surfaces are observed at 2100 cm^{-1}.[102, 103]

The CO stretching vibration at 2097 cm^{-1} after 10 Pt ALD cycles shifts very slightly versus Pt ALD cycles. The CO stretching vibration is observed at 2100 cm^{-1} after 65 Pt ALD cycles. Although this CO stretching vibration frequency is consistent with the CO stretching frequency on on-top sites on Pt(111) single-crystal surfaces,[102, 103] small Pt nanoparticles could not have

extensive Pt(111) surface area. Consequently, this CO stretching frequency is assigned to CO on more electropositive Pt clusters or surfaces.[125, 126, 104] These more electropositive Pt clusters or surfaces may be associated with Pt that still retains some hfac coordination. This ALD reaction involves a large and difficult to remove ligand, some of which remained attached to the surface and promoted island growth through the course of the deposition. In this study, that is to our advantage, and is used specifically to discourage conformally deposited platinum. In fact, moving a step further, the knowledge of this site-blocking mechanism led to using the pure diketone as a site-blocking agent to control the amount of sites available on the surface.

Figure 4.9 has the FTIR spectrum of a 150 °C TiO_2 surface dosed with hexafluoracetylacetone to near saturation, making the surface have many less available reactive sites, and then dosed with $Pt(hfac)_2$. This, compared with a TiO_2 surface dosed with the same amount of $Pt(hfac)_2$, had less attached platinum. The ligand stretches were very similar, showing that the total amount of diketone bound to the powders was about the same. Figure 4.9(a) displays the spectrum of $Pt(hfac)_2$ on TiO_2, similar to Figure 4.1 though at a different temperature. In Figure 4.9(b) the spectrum illustrates the expected site-blocked surface after a pre-treatment step with the pure diketone, hfacH. Figure 4.9(c) and (d) show TiO_2 treated with hfacH and then $Pt(hfac)_2$, but in Figure (d), the hfacH/TiO_2 surface was subtracted to show only the added $Pt(hfac)_2$. Without pre-treatment, there is much more area under the feature at 1590 cm^{-1} associated with platinum. On the pre-treated surface, there is far less carbonyl stretch associated with platinum. Less platinum hfac reacted with the pre-treated surface, because already attached ligand successfully occupied sites and prevented it.

In Figure 4.10, major differences in the spacing of the platinum particles on the TiO_2 powder surface arose as the result of growing two batches, one pre-treated as in Figure 4.9, and one grown with exactly the same conditions except excluding the pre-treatment. The particles stayed much further apart, leading to far fewer particles overall, and the diameters of the particles were slightly smaller in the site-blocked sample. The slight difference in probably follows from the expected

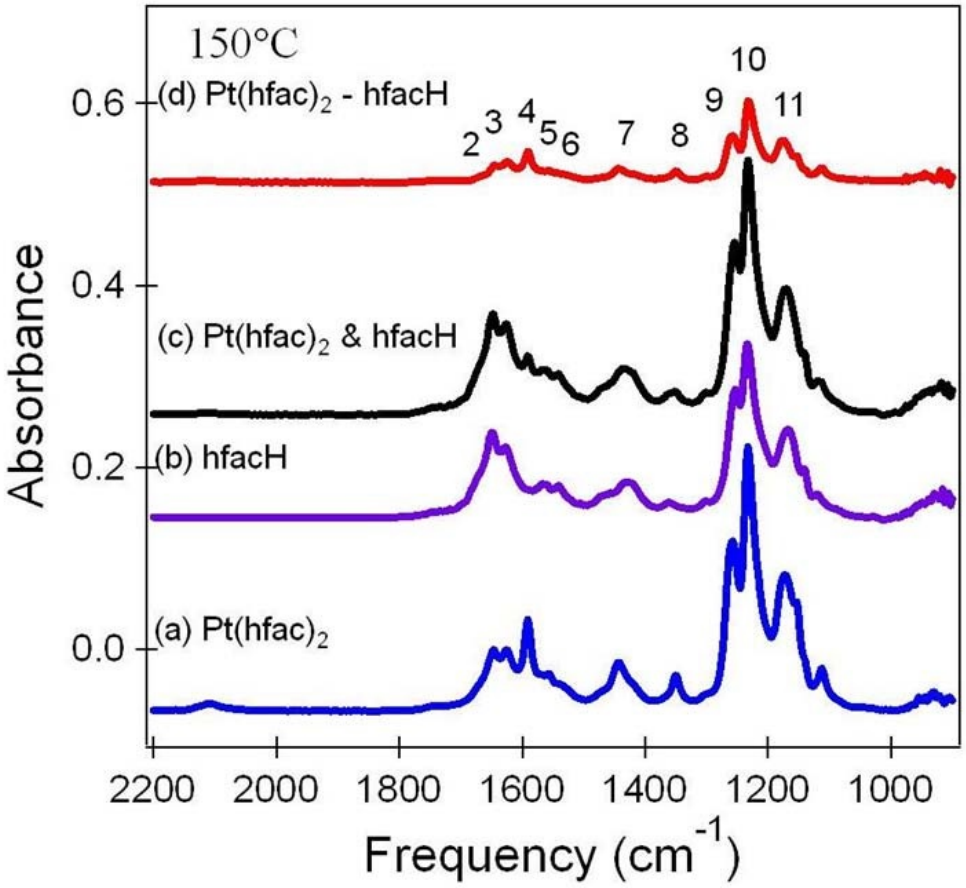

Figure 4.9: Example of site-blocking using hexafluoroacetylacetone (hfacH). Several FTIR spectra illustrate that site-blocking of the TiO_2 with hexafluoroacetylacetone (hfacH) at 150 °C prevents full addition of $Pt(hfac)_2$ to the surface. Spectra (a) adsorption of $Pt(hfac)_2$. (b) Adsorption of hexafluoroacetylacetone (hfacH). (c) Adsorption of $Pt(hfac)_2$ after preadsorption of hfacH. (d) Difference spectra $Pt(hfac)_2$ hfacH showing absorbance gain after adsorbing $Pt(hfac)_2$ on surface covered with hfacH.

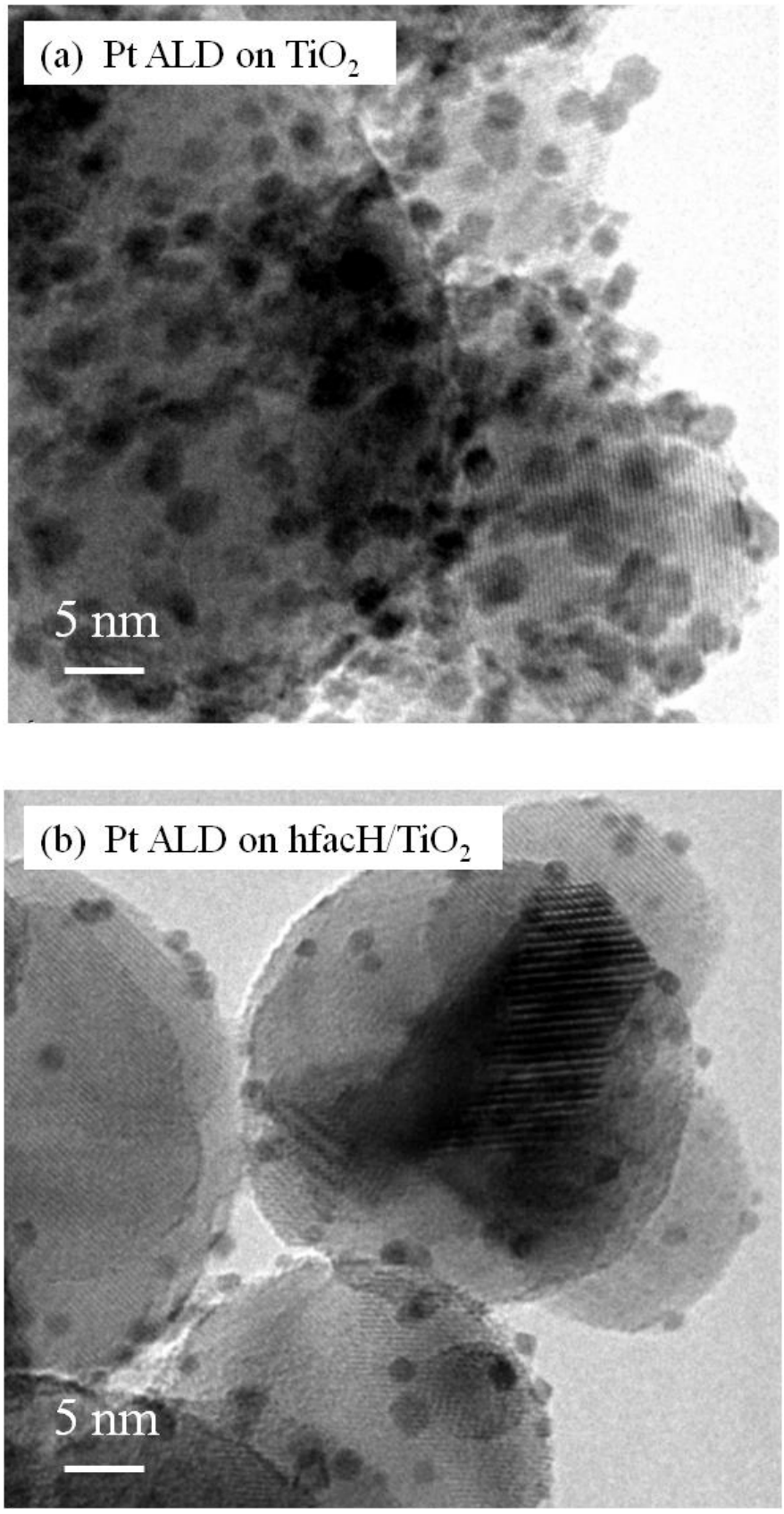

Figure 4.10: Transmission electron microscope image comparing site-blocked sample with a non-site-blocked sample. Each sample of Pt nanoparticles had 150 cycles Pt ALD deposited at 200 °C. The (b) image shows what happened when the TiO_2 powders were initially exposed to hfacH.

growth mechanism, which could include some platinum atom mobility. Within a small radius, the platinum probably finds and binds to itself, causing the atoms in a certain area to gather, and with less platinum on the surface, this influence on growth would be reduced.

The platinum nanoparticle coverage in Figure 4.10(a) is 6-7 nanoparticles/100 nm^2 without the preadsorbed hfacH. The Pt nanoparticle coverage in Figure 4.10(b) is 1-3 nanoparticles/100 nm^2 with the preadsorbed hfacH. The Pt nanoparticle diameter is also reduced by the preadsorbed hfacH on the TiO_2 powders. The Pt nanoparticle diameter is 2.5 nm without the preadsorbed hfacH in Figure 4.10(a). The Pt nanoparticle diameter is 1.5 nm with the preadsorbed hfacH in Figure 4.10(b). The lower Pt nanoparticle coverages and smaller Pt nanoparticle diameters are consistent with fewer Pt atoms deposited by $Pt(hfac)_2$ on the TiO_2 surface with preadsorbed hfacH.

In addition, the hexafluoracetylacetone coverage could be tuned through knowledge of the desorption from the surface. In Figure 4.11, the top spectrum examined a TiO_2 surface dosed with hexafluoracetylacetone, and then the desorption was examined by taking FTIR spectra at various time points. The initial difference spectra at time zero shows a saturated surface, and then the following spectra are taken at 5, 42, and 118 minutes following. The mechanism of desorption likely involves the transfer of a proton from a surface hydroxyl group, and could also involve some breakdown mechanism, with some dependance on how much platinum is available to mediate reactions on the surface. TiO_2 itself has some mobile oxygen and could account for some carbonate species forming on the surface by supplying the oxidative force to the ligands.

Figure 4.12 shows the results of desorption from TiO_2 at four temperatures, 175, 200, 225, and 250 °C. An estimate of the activation energy of desorption from the surface came from taking initial slopes, and using first order kinetics to find rate constants, but it looks like the system involves more than a single loss pathway. Based off of the appearance of presumed carbon monoxide and surface CF_3 groups over time, and from work by Girolami et al. of hfac breakdown and desorption from crystalline copper surfaces, the hfac undergoes both desorption and breakdown on the surface. First order mechanism rate constants could come from presuming that the disappearing

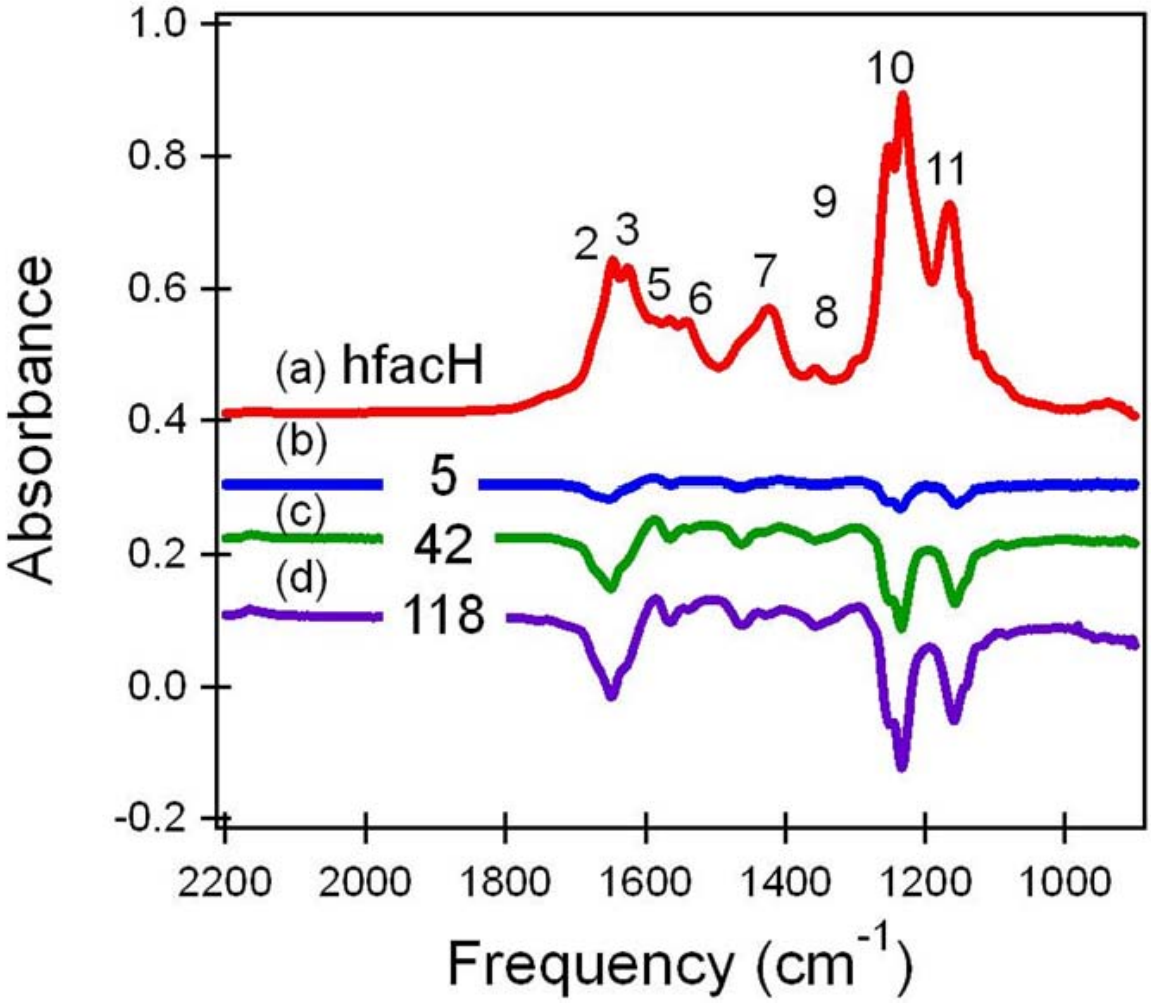

Figure 4.11: FTIR difference spectra of initial hfacH on TiO_2 and after time lapses at 200 °C. The spectra taken after 5, 42, and 118 minutes were referenced back to the (a) hfacH exposed TiO_2 surface. Decomposition and desorption of hfacH appear at this temperature.

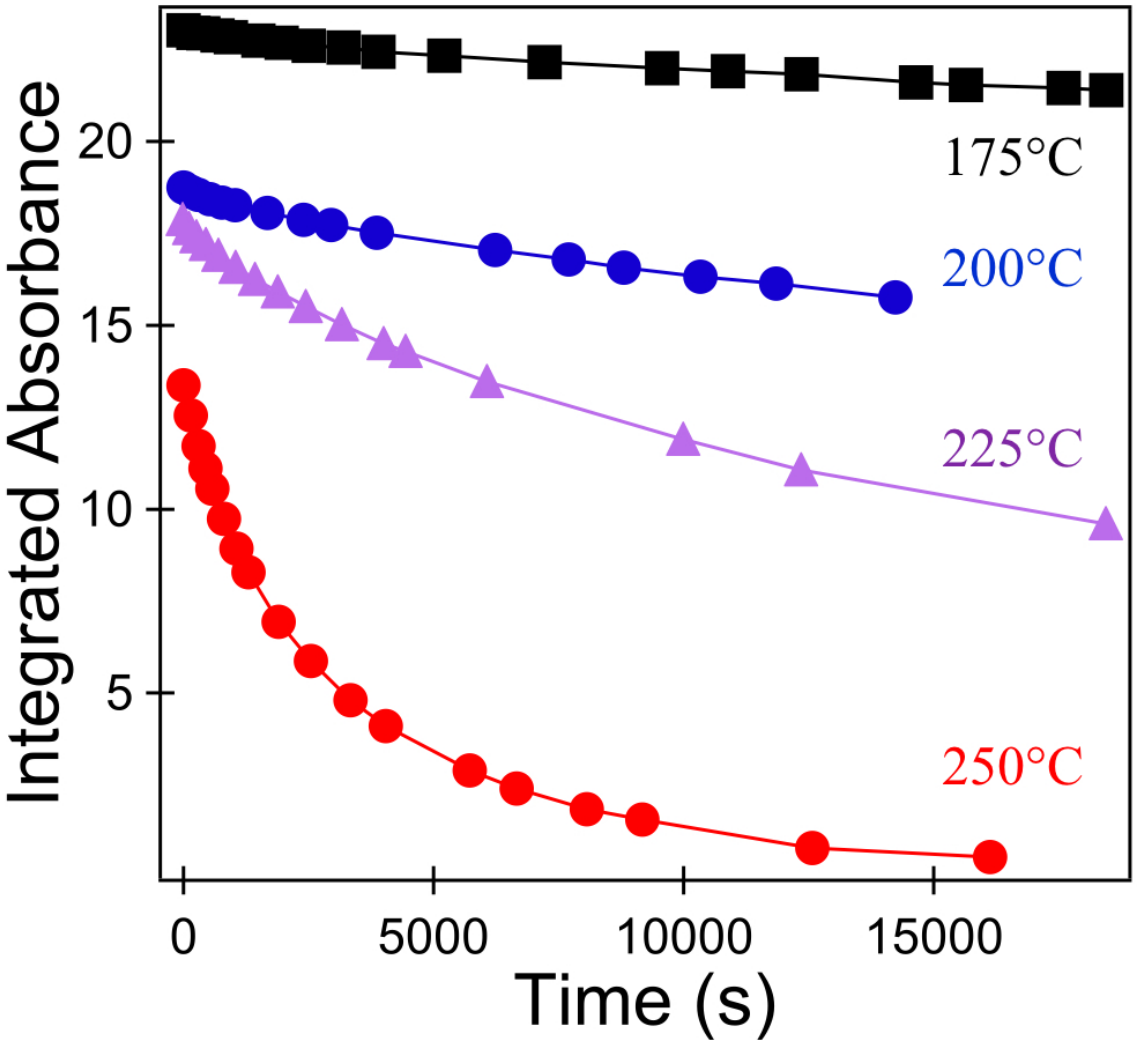

Figure 4.12: Following hfacH at 175, 200, 225, and 250 °C over time. The integrated absorbance changes of modes 3-7 in Table 4.1 were of loss with time at the four temperatures.

carbonyl species depends on the only the TiO_2 surface and the hfac coverage density. From the rate constants, an estimate of the activation energy for leaving the surface was obtained using the Arrhenius equation. The value of 96 ± 9 kJ/mol was more than the activation energy of desorption observed by Goldstein of hfacH from an alumina surface, and was expected to follow not only the desorption path, but a breakdown path.

TiO_2 powders provided a convenient substrate for the FTIR studies of Pt ALD and Pt nanoparticle formation because the they are insulators and are not conducting. Consequently, the TiO_2 powders did not display background infrared absorption. Pt nanoparticles on doped TiO_2, and other oxide substrates, such as tungsten oxide, are relevant for PEM fuel cells. Tungsten oxide is electrochemically stable under the PEM fuel cell environment.[127] Tungsten oxide can also be electrically conductive. Electrical conductivity is needed for electron transport in PEM fuel cells. However, the electrical conductivity of WO_x nanorods precludes their use for FTIR studies because of background infrared absorption according to Drude-Zener theory.[128, 129] In order to compare growth on titanium oxide with growth on tungsten oxide, the same Pt ALD procedure took place under the same conditions on the two different powders, and it can be seen in figure 4.13 that the results show similar outcomes. The shapes of the substrates are different, with the titanium oxide being spheroid and the tungsten oxide being rods[99], but both appear crystalline, which is reasonable since both had been heated to or above 350 °C. The average Pt nanoparticle diameters are 2.0 and 4.5 nm on the TiO_2 and WO_x surfaces, respectively. The average Pt nanoparticle coverages are 6-7 and 2-3 nanoparticles/100 nm^2 on the TiO_2 and WO_x surfaces, respectively. These contrasting Pt nanoparticle coverages and sizes indicate that the growth mechanisms are slightly different on the two substrates.

The TEM of Figure 4.14 shows 170 Pt ALD cycles deposited at 200 °C. The $Pt(hfac)_2$ and formalin exposures were sufficient to yield near saturation coverages on TiO_2 powders after 20-30 Pt ALD cycles. The first twenty ALD cycles were performed with a TMA exposure after the formalin exposure to remove the $Pt(hfac)_2$ and formalin adsorption products.[130] This TEM image

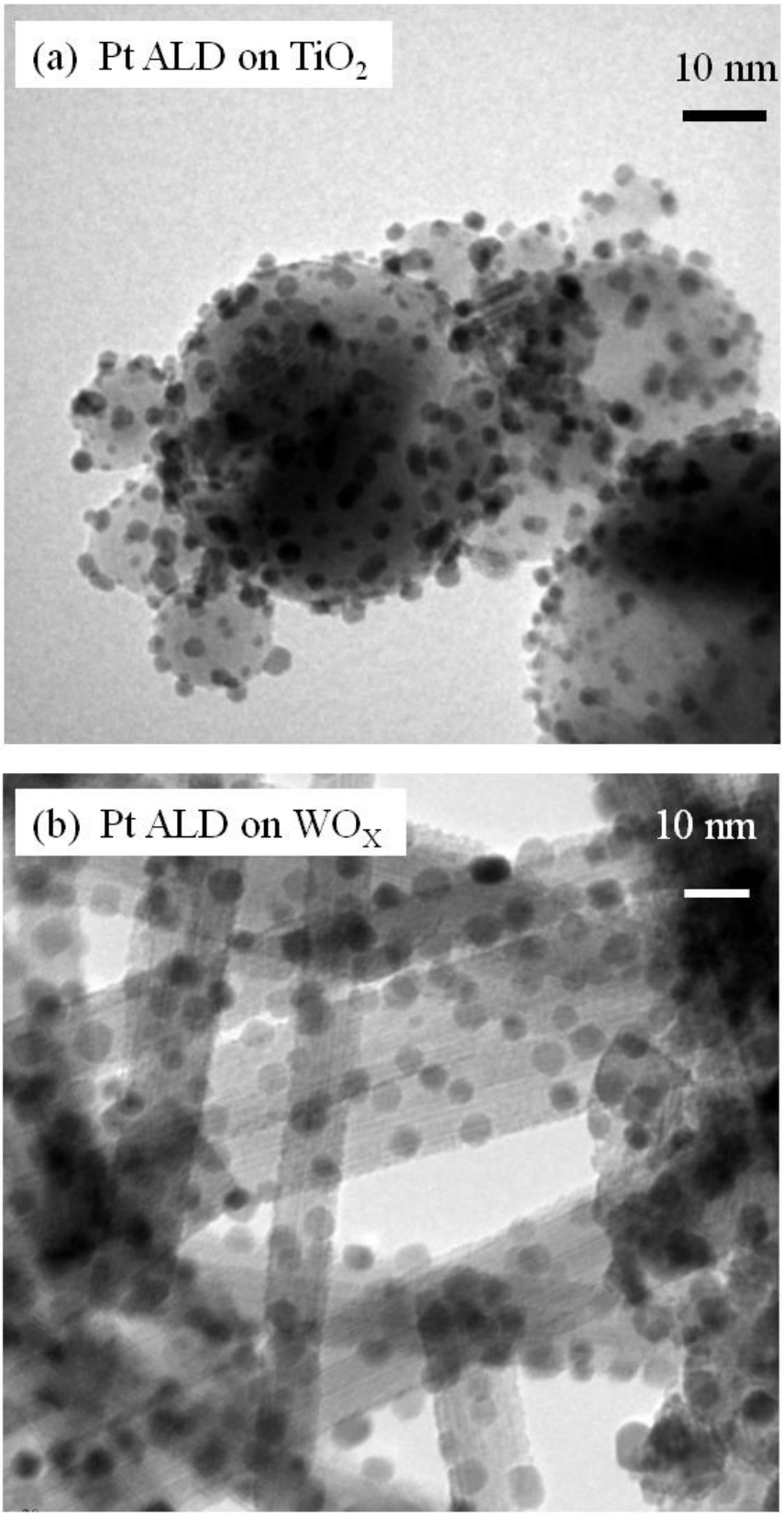

Figure 4.13: TEM image of 150 cycles $Pt(hfac)_2$ and formalin on TiO_2 and WO_x at 200 °C.

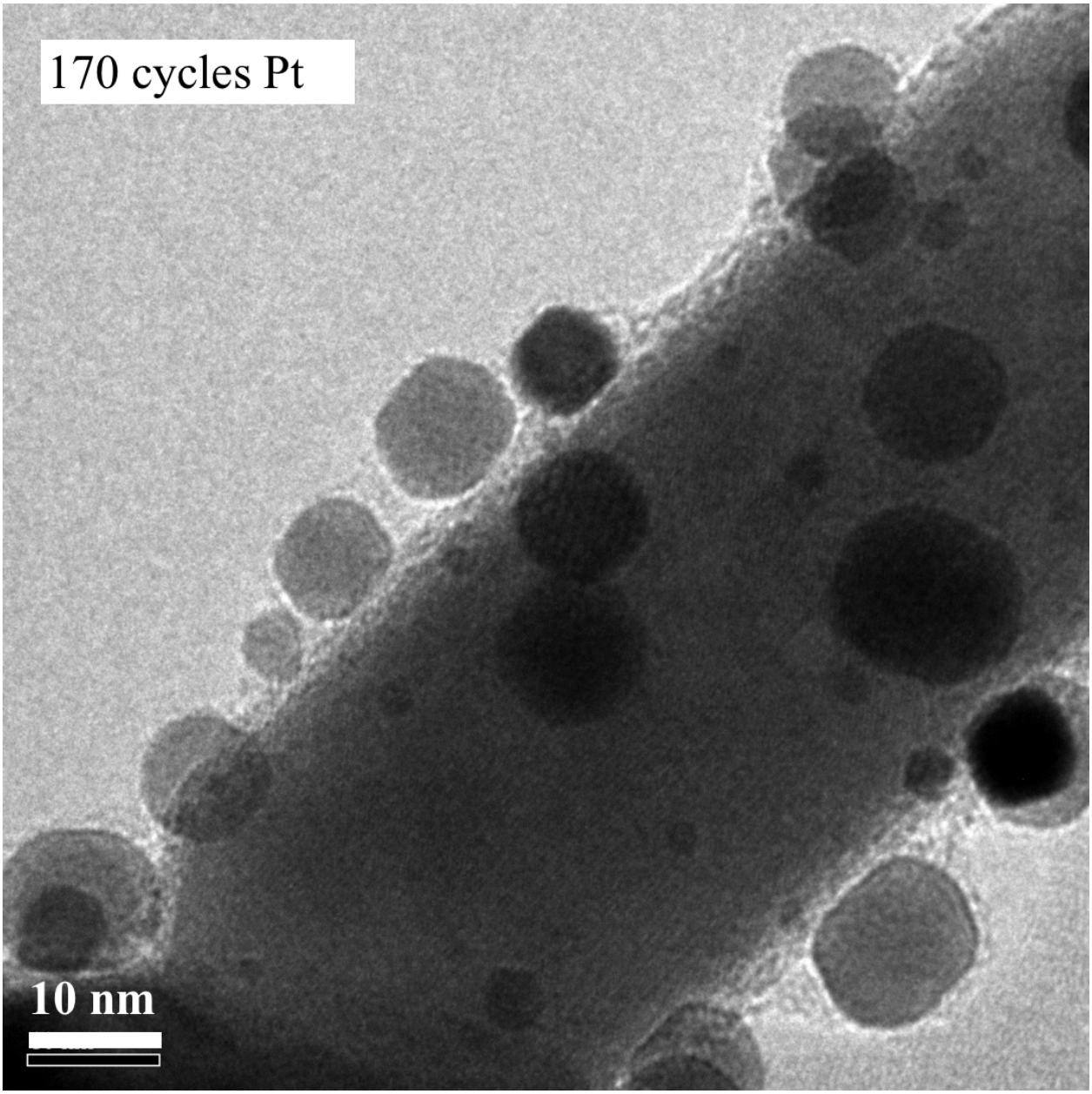

Figure 4.14: TEM image of 170 cycles $Pt(hfac)_2$ and formalin on WO_x, the first 15 cycles of which included TMA after formalin, deposited at 200 °C.

illustrates the highly spherical nature of the Pt nanoparticles. Spherical shapes are consistent with the high surface energy of Pt that fosters the formation of spherical Pt particles to minimize the surface area to minimize the surface energy.

In order to examine the growth in the latter part of the nucleation regime, a series of Pt ALD on WO_X were grown at the same conditions. When examined, monodisperse size distribution was not the outcome. Rather, the diameters of Pt particles varied visibly on the WO_X powder substrates, and the average size increased with cycle number. Since desorption of hfac from a TiO_2 surface at 200 °C appeared significant over the timescale of the reaction in Figure 4.13, the platinum particle sizes could be due to the desorption of the hfac ligand over the course of the reaction, opening surface sites over time and allowing continued nucleation throughout the deposition. It may be limited, since sites already containing platinum might be preferred reaction locations, but would explain the range of sizes seen on each sample. In Figure 4.15, the 130, 140, and 150 cycles Pt on WO_X illustrates the change of the Pt particle sizes. At 130 cycles, the Pt looks barely visible with the microscope, but the relatively rapid change after the next two 10 cycle increments is explained by an exponential take-off in ALD growth for noble metals past a slow nucleation stage.[78] The Pt nanoparticle diameters were 2.0, 2.2, and 4.5 nm after 130, 140 and 150 Pt ALD cycles, respectively. The corresponding Pt nanoparticle coverages were 1, 2-3, and 2-3 nanoparticles/100 nm^2 after 130, 140 and 150 Pt ALD cycles, respectively.

Difficulties with the $Pt(hfac)_2$ precursor were encountered during scale-up, and there are possible ways to address them. In addition, in order to use the site-blocking method, it may be that hfacH treatment could be employed with a more volatile platinum source. The section of scaling the reaction to larger samples starts down the path to this, and includes some of the possible solutions to the sample inconsistency initially seen.

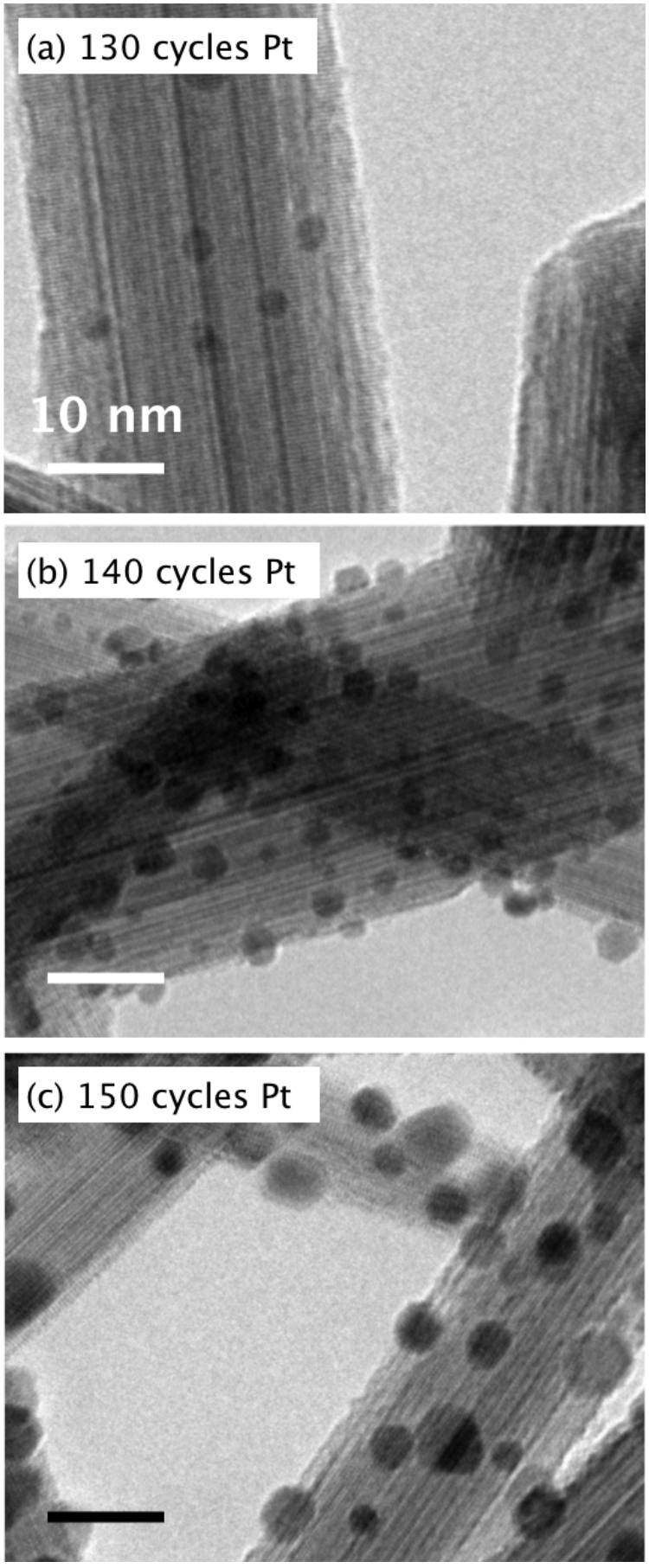

Figure 4.15: TEM images of platinum ALD on WO_X, comparing 130, 140, and 150 cycles at 200 °C.

4.3.2 Static rotary reactor with porous cylinder sample holder

Sample sizes of Pt/WO_X on the order of 10-15 mg could be synthesized with consistency using the viscous flow reactor. However, in order to scale up the $Pt(hfac)_2$ and formalin ALD system to synthesize larger samples of Pt/WO_X, a static rotary ALD reactor was employed). The static rotary reactor is capable of holding powdered samples far larger than the hundreds of milligrams needed for testing. In moving to larger samples, switching to a reactor suitable for sizeable powder substrates caused some adjustments in the dosing methodology, and they are mentioned in the experimental section. The small samples grown in the FTIR reactor showed reproducibility and powder samples evenly coated with platinum particles. In contrast, the initial scaled-up samples were inconsistent, and varied widely depending on minor changes in heating and even apparently on the amount of precursor sitting in the bubbler and giving off vapor to the reactor.

The rotary motion tumbles the substrate powder, discouraging agglomeration during ALD, assisting in the synthesis of large batches of Pt/WO_X in a consistent way. Initial scale-up experiments with the static rotary reactor used the porous steel cylinder as described in the experimental methods section. Samples of Pt/WO_X using the porous cylinder were prepared according to the reaction sequence also detailed in the experimental methods section. A series of depositions consisting of 150, 200, 210, and 230 ALD cycles of $Pt(hfac)_2$ and formalin at 200 °CC showed significant nonlinearity in Pt weight percent versus the number of ALD cycles. Additionally, TEM images from these samples show Pt nanoparticles with a wide range of diameters, with varying morphologies and an uneven distribution.

After growing this series of samples in the rotary reactor, it became clear that the $Pt(hfac)_2$ precursor was challenging to use in a bigger reactor on the larger samples. The small samples grown in the FTIR reactor showed reproducibility and powder samples evenly coated with platinum particles. In contrast, the scaled-up samples were inconsistent, and varied widely depending on minor changes in heating.

The source of this sample inhomogeneity was believed to be the result of long adsorption/desorption

times for the $Pt(hfac)_2$ precursor in the porous cylinder due to its low vapor pressure. The high surface area pores of the porous cylinder provided sites for the $Pt(hfac)_2$ to adsorb and condense. This made effective purging of the $Pt(hfac)_2$ difficult and likely resulted in a CVD reaction with the formalin. Simply increasing the reaction and $Pt(hfac)_2$ precursor temperatures to minimize this undesirable affect however risked decomposition of the precursor as well as Pt atom mobility on the WOx surface. In order to achieve more homogenous depositions, an open-ended cylinder was designed to improve precursor access to the WO_X substrate.

4.3.3 Static rotary reactor with open cylinder sample holder

A series of depositions consisting of 159, 170, 200, and 212 ALD cycles of $Pt(hfac)_2$ and formalin at 200 °C using the open-ended cylinder showed improved linearity between Pt weight percent and the number of ALD cycles. However, TEM images from this series still show Pt nanoparticles with varying sizes and morphologies that are relatively unevenly distributed on the WO_X nanorods. Although switching to the open-ended cylinder improved the linearity between Pt weight percent and number of ALD cycles, the depositions remained inhomogenous. In addition, due to the low volatility of the $Pt(hfac)_2$ precursor, over 200 cycles were required to achieve metal loadings upwards of 19 % Pt by weight in the Pt/WO_X samples. An unrealistically high number of ALD cycles would be required in order to synthesize Pt/WO_X samples with a Pt weight percent of 50 %. From these results, it was apparent that the $Pt(hfac)_2$ and formalin chemistry was not suitable to provide large samples of uniformly distributed monodisperse Pt nanoparticles on WO_X at high weight percent. Though the open cylinder design helped a great deal, some samples still showed internal variability. Large platinum particles led us to believe that some type of CVD had taken place, and that the very large surface area of the sample powder combined with the low vapor pressure of the $Pt(hfac)_2$ would be difficult to overcome without raising the temperature (and therefore increasing the platinum atom mobility, leading to less surface control) or increasing the purge times to lengths that would not be industrially practical. The site-blocking information may be in future put to use if increased spacing seems to be a way to increase cathode durability.

Figure 4.16 shows images of platinum nanoparticles deposited on WO_x using $Me_3PtMeCp$ with O_2. The 130 cycle Pt/WO_x sample has nearly identical weight percent as a sample with 200 cycles $Pt(hfac)_2$ and formalin, when both were synthesized at 200 °C. The image shows WO_x nanorods evenly covered with platinum nanoparticles. A 10 % by weight Pt/WO_x sample required 200 cycles of $Pt(hfac)_2$ and formalin whereas the 9 % by weight Pt/WO_x sample only required 130 cycles of $Me_3PtMeCp$. This indicates that the $Me_3PtMeCp$ and O_2 ALD system produces similar wt% Pt/WO_x samples with fewer ALD cycles compared to the $Pt(hfac)_2$ and formalin system.

The precursor $Me_3PtMeCp$ with O_2 as a co-reactant contrasts with the $Pt(hfac)_2$ and formalin based reaction in part because the $Me_3PtMeCp$ precursor has a higher vapor pressure. Platinum ALD using $Me_3PtMeCp$ and O_2 are more studied than $Pt(hfac)_2$ and formalin, and even though the reaction is not completely understood, the idea is that $Me_3PtMeCp$ reacts with the surface, and may give up a methyl, or a methylcyclopentyldienyl group to attach to the surface. Oxygen then most likely provides an oxidation pathway for any remaining carbonaceous ligand material, and platinum metal remains on the surface.

Figure 4.16 compares two TEM images of platinum ALD on WO_x from 130 (a) and 200 (b) cycles $Me_3PtMeCp$ and O_2 at 200 °C. The Pt/WO_x sample corresponding to image (a) has 9 % Pt by weight and shows reasonably distributed particles with diameters from 3 - 4 nm. The Pt/WO_x sample corresponding to image (b) has 46 % Pt by weight and shows a similar distribution of particles with slightly larger diameters. This indicates that a higher weight percent of Pt can be achieved with increased number of ALD cycles.

In order to determine whether the synthesized Pt/WO_x materials are catalytically active toward the ORR, RDE experiments in 0.1 M $HClO_4$ were conducted. The mass activity of each Pt/WO_x sample was calculated and compared to that of a standard Pt/C catalyst. The mass activity was calculated from the experimentally determined electrochemical surface area and specific activity. The Pt/WO_x sample mass activities were characterized with and without graphitized carbon nanofiber (GCNF) additive. The GCNF is added to the Pt/WO_x material to increase the electrical

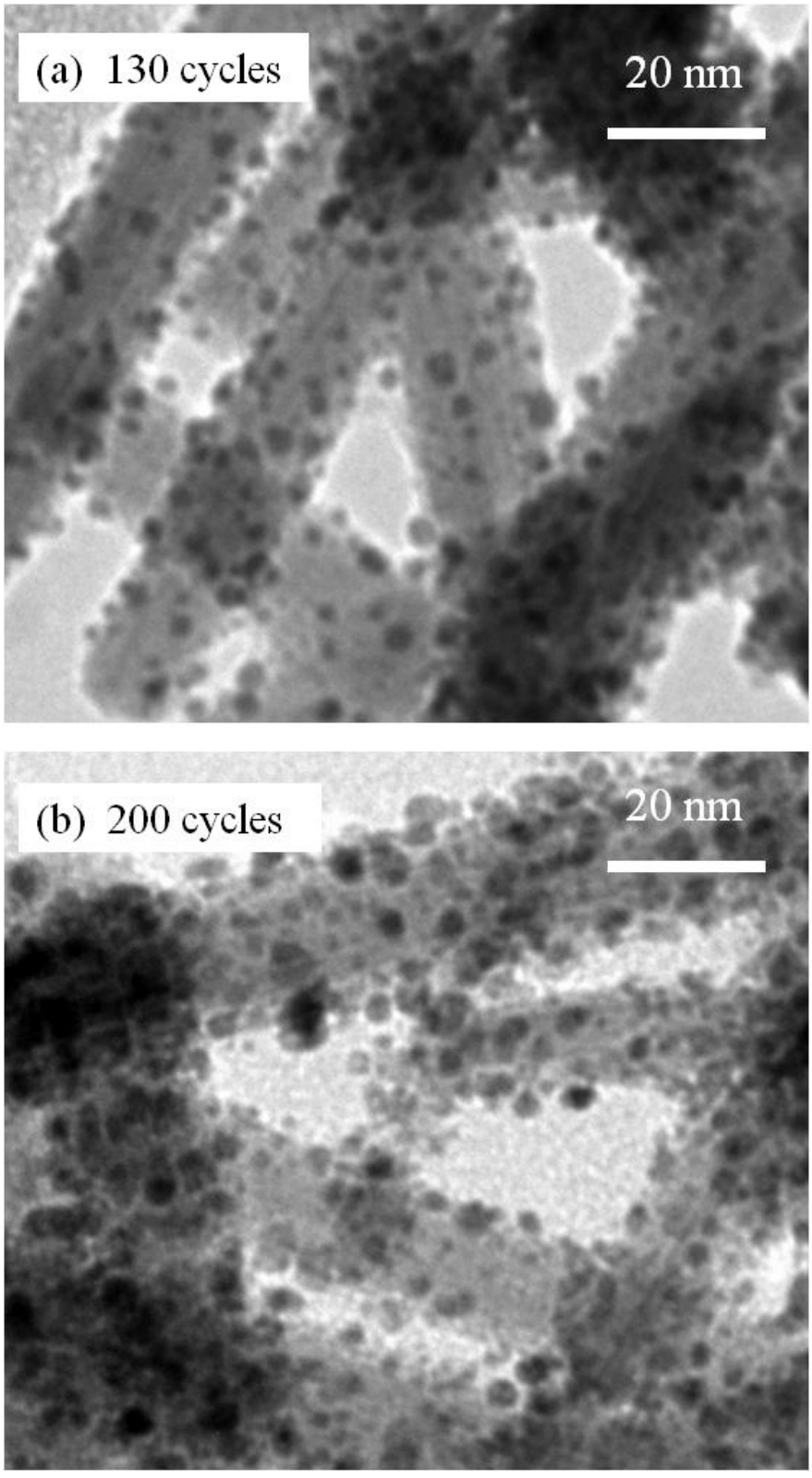

Figure 4.16: Rotary platinum ALD results with $PtMe_3MeCp$ and oxygen at 200 °C on WO_x using an open cylinder.

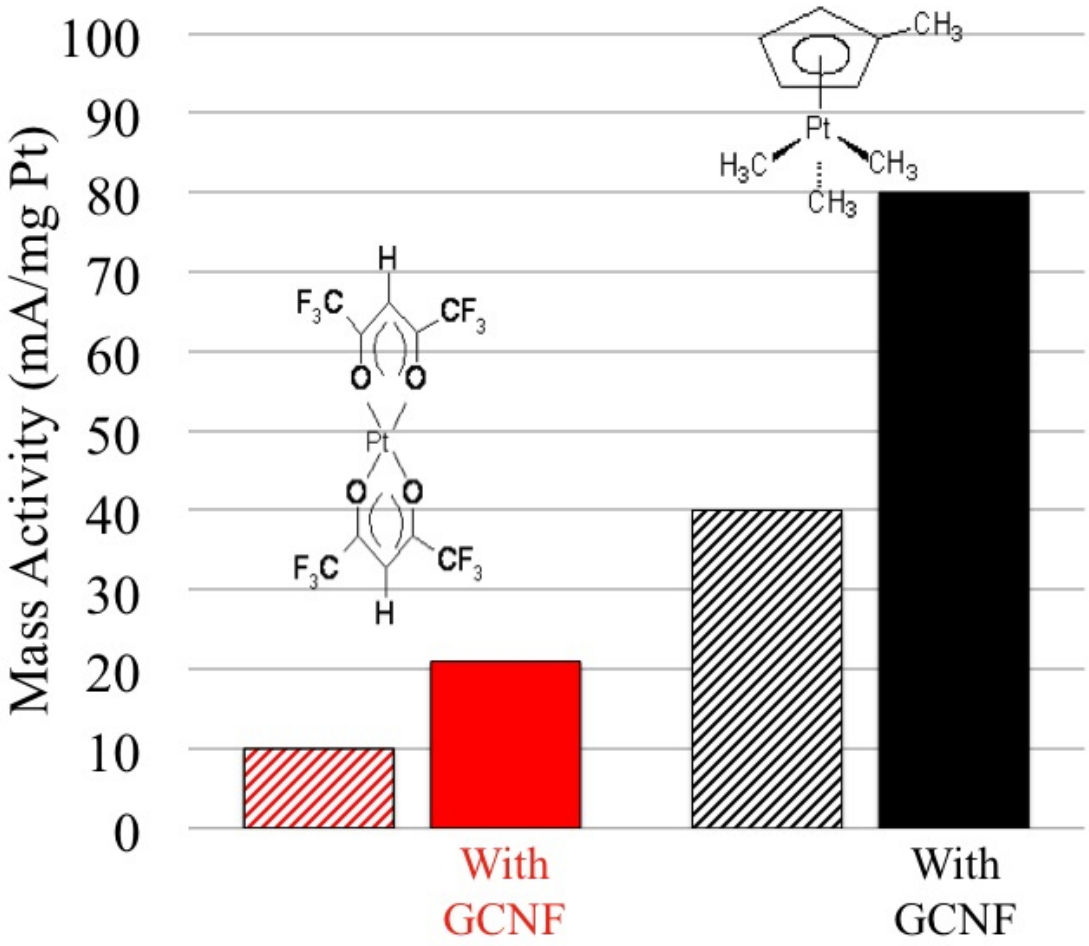

Figure 4.17: Rotating disk electrode activity of as-grown and carbon enhanced Pt/WO_x samples.

conductivity because WO_X has a low electrical conductivity on the order of 0.1-0.4 (ohm cm)$^{-1}$. The mass activity of Pt/WO_X samples synthesized using both Pt(hfac)$_2$ and Me_3PtMeCp was studied both with and without the carbon nanofiber additive. Figure 2.15 compares the mass activity of a 21 % Pt by weight sample from Pt(hfac)$_2$ to a 46 % by weight Pt/WO_X sample from Me_3PtMeCp. The 21 % Pt/WO_X sample from Pt(hfac)$_2$ without GCNF additive had a mass activity of 10 mA/mgPt and increased to 21 mA/mgPt with the addition of GCNF to be 10 % by weight Pt. The 46 % Pt/WO_X sample from Me_3PtMeCp without GCNF additive had a mass activity of 40 mA/mgPt and increased to 80 mA/mgPt with the addition of GCNF to be 23 % by weight Pt. This comparison shows that the addition of GCNF to the Pt/WO_X samples increases the mass activity by a factor of two.

4.4 Conclusion

Platinum nanoparticles were deposited on both titanium oxide and tungsten oxide powders at at 200 °C using platinum II hexafluoracetylacetonate and formalin, as atomic layer deposition (ALD) precursors. Repeated alternating application of Pt(hfac)$_2$ and formalin led to the formation of platinum nanoparticles. A strong infrared feature at 2100 cm^{-1} in the FTIR spectrum after several Pt(hfac)$_2$ and formalin exposures was also consistent for CO (carbon monoxide) on the platinum nanoparticles. The FTIR spectrum of Pt(hfac)$_2$ on TiO_2 was very similar to the FTIR spectrum of hfacH on TiO_2. During growth FTIR probed the platinum surface chemistry during reactions, and afterwards the resulting samples were examined with transmission electron microscopy (TEM). Using ALD allowed a measure of control of the size of the particles based on the number of cycles. As seen by other researchers using Me_3PtMeCp on carbon, TiO_2, and strontium titanate, among others, the average size of the particles increased with number of cycles. The mismatch between the metal oxide surface and the platinum metal, and the resulting preferential bonding among platinum atoms, caused islands of platinum rather than continuous films, and the separation was enhanced using the hfacH. The hfac ligand encouraged particles rather than conformal film, by blocking sites on the metal oxide surface during the reactions. Treating the surface with additional

hfacH resulted in greater distance between the particles. Changes in the hfacH surface coverage with temperature gave a pathway towards controlling the amount of site-blocking possible using a chemical pre-treatment exposure. The FTIR showed that higher temperatures encouraged fewer ligand features.

Scaled-up powder samples deposition results showed that using $Pt(hfac)_2$ led to difficulties when dosed on large samples in a rotary reactor. Greater homogeneity was achieved by changing precursors, and modifying the standard sample holder. Much more consistent results came when samples were grown in an open ended cylinder instead of a porous cylinder in a rotary reactor. In addition, the results in the scaled-up depostions showed more homogeneity in particle size when done with the more volatile $Me_3PtMeCp$ and O_2 rather than $Pt(hfac)_2$ and formalin. Though not yet tried, this could allow for site-blocking to be carried out with hfacH pre-treatment, and then $Me_3PtMeCp$ could be used as the precursor for the platinum deposition. Results using Pt/WO_x as oxygen reduction catalysts do not favorably compare to Pt/C activities, due at least in part to the low conductivity of the tungsten oxide.

4.5 Acknowledgments

This was a very collaborative project with Noemi Leick, Joel W. Clancey, Katherine E. Hurst, Andrew S. Cavanagh, Shyam S. Kocha, and Anne C. Dillon. The Department of Energy provided funding through the National Renewable Energy Laboratory (NREL). The TEM images were taken at NREL by Kim M. Jones. Layton Baker provided useful discussions.

Chapter 5

Sulfur Functionalization

5.1 Introduction

Transportation by car encompasses enough tonnage that decreasing that tonnage to waste less fuel can be achieved by small changes. Here the study of a way to lighten tires involved surface functionalization. For a long time, carbon black filler in rubber increased grip and wear resistance of tires. Explorations of alternate filler for improvements in rubber properties for tires include silica, alumina, and polyamide.[131, 132, 133, 134] In the tire industry, three major performance metrics were considered exclusive of each other: wear resistance, rolling resistance, and grip on wet surfaces. Ideally all of them would be maximized, but grip and ease of rolling, rather naturally, are rarely simultaneously improved. Replacing carbon black with silicon oxide powder as filler, tires improved in both grip and rolling resistance. In order to increase the mixing, another filler bridged the silica and rubber non-mixing tendency: Si-69, shown in figure 5.5, with both sulfur and ethoxysilane in the molecule. On the disadvantage side of this new material additive, volatile organic compounds were released during the processing, leading to more steps to clean the waste gases, and glass is lighter than carbon black but still denser than desirable. The less mass added to tires as filler/strengthening agent, the more fuel efficient cars could be, and Kevlar could be better than SiO_2, if it mixed well with the rubber.[135, 136]

Since the goal of this study was making tires lighter and more fuel efficient, a strong and light material was desired. Goodyear funded this study, and their focus on Kevlar filler, in the form of chopped fibers, stems from Kevlar being a low density but strong polymer. Kevlar mixed only

very poorly with tire rubber, leading to zones of rubber with no filler, and other zones with more filler than desired. The processing of rubber for tires involves many complicated steps, including the use of additives that are not all known to us, being disclosed by Goodyear on a need-to-know basis. Despite not knowing some parts of the process, the strategy for making the Kevlar more likely to mix with rubber requires knowledge of the intermolecular bond types of the Kevlar and the rubber. In order to mix rubber with Kevlar fibers, miscibility changes were attempted through gas phase self-limiting reactions to modify the interface contact area. Atomic Layer Depostion (ALD) offered some advantages. For one thing, it required no solution chemistry, merely the exposure of the fibers to small amounts of vapors. The gas phase technique allowed modifying only the surface with well known engineering, with something that could drastically change the misciblity with very little extra chemical. Vulcanized rubber is made up of hydrocarbon chains with both single and double bonds, connected by sulfur linkages.

More broadly than the tire story, a wide range of materials would play greater roles in more applications if their usefulness were not limited by their lack of affinity for other materials. Miscibility and the mixing of two or more chemicals play a crucial part in many industries. In general, a very small amount of chemical used in the appropriate manner could lead to enormous changes in the mixing properties of a wide selection of materials. Mixing properties depend on the attraction between the components. The thermodynamic expression for mixing would be the Gibbs free energy change at constant pressure. The change in the Gibbs free energy of mixing depends on the enthalpy and entropy changes of mixing. The entropy depends on mole fractions of the components and the temperature. In order to mix Kevlar with rubber, the enthalpic intermolecular bond energy changes are important. Kevlar moieties include phenyl rings and amide links with hydrogen bonds between the polymer chains.

The intermolecular bond strength of Kevlar relies on the very polar hydrogen bonds along with induced dipole forces. Disrupting even a meter of a single strand of Kevlar fiber, assuming a hydrogen bond strength of 25 kJ/mol, would be difficult when the opportunities for dipole-dipole

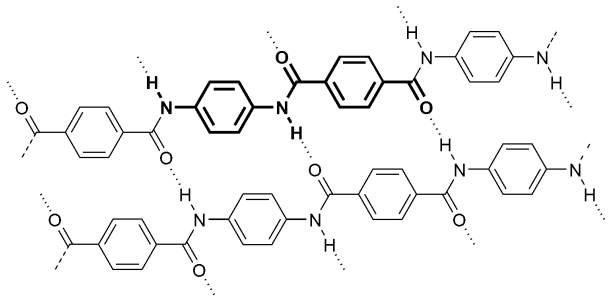

Figure 5.1: Kevlar, image from http://en.wikipedia.org/wiki/Kevlar

interactions meant perhaps 4 kJ/mol for dipole-dipole interactions and the induced dipole interactions remained similar. Unlike what would happen on silica, it is not expected that Si-69 would be easily directly bound to Kevlar. Aluminum oxide is one of the best-characterized and straightforward reactions in the atomic layer deposition, and frequently serves as an intermediate layer between substrate and the desired layer, because it adds little extra chemical, and is relatively cheap, abundant, and nontoxic. Then, instead of using large quantities of Si-69 in the tire mix, but using gas phase chemistry, only tiny amounts of Si-69 would be enough to coat the surface, if the reactions went as expected. It would make sense that the strands would be much more amenable to separation once the hydrogen bonding regular structure got disrupted by the trimethyl aluminum, and less likely to agglomerate if the hydroxyl groups were reacted with Si-69. The attractions between sulfurs on different molecules would only encourage mixing rather than separation of Kevlar and rubber.

Kevlar is an amido linked polyer with phenyl rings in the backbone, and is very strong and very light. The chopped fibers have much greater affinity with their own kind than with the rubber. Rubber, on the other hand, seems relatively simple, but is taken through extremely complex processing to be used for tires. The type of molecules used to coat Kevlar all included sulfur in order to interact favorably with the Vulcanized rubber. The ideal functionality for the Kevlar interface molecule might be a thiol, or the tetrasulfide chain of Si-69, but with so many agents involved at

so many different stages of temperature and time, testing samples with different functionalized surfaces was preferable to predicting the best molecule type. The clearest answer to which molecule to use would be gained by including functionalized Kevlar with different molecules attached, in separate tire making runs. The main change in the rubber backbone, at least, is well known. Vulcanization strengthens the rubber using sulfur crosslinks. Thus, adding sulfur functionality to the Kevlar surface would be bound to increase the miscibility.

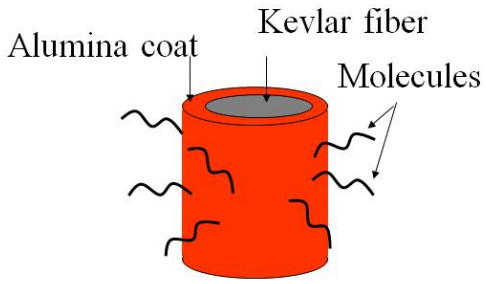

Figure 5.2: Cartoon of fiber coated with Al_2O_3 and silane molecules.

The cartoon represents the coated Kevlar fiber. Not drawn to scale, the inner fiber would remain the majority component, and the added Al_2O_3 and silane molecules would make up so little of the mass as to be close to negligible. Three different but related molecules were attached to the priming surface. The chosen molecules beta-mercaptotriethoxysilane, bis(3-triethoxysilylpropyl) disulfide, and bis(3-triethoxysilylpropyl) tetrasulfide, all have sulfur. The S-H bond of the thiol contrasted with S-S bonds in the other two, along with the larger size, since the silane was otherwise mirrored. The bis(3-triethoxysilylpropyl) tetrasulfide molecule mentioned is a common industry compound, with the short name Si-69. The expected mechanism, based on siloxane solution reactions, involved reaction of the silicon center with the oxygen of a surface hydroxyl, and the formation of ethanol, which is unfortunately a volatile organic compound, but one that is commonly

dealt with and would be expected to be present in minor amounts relative to the current usage.[137]

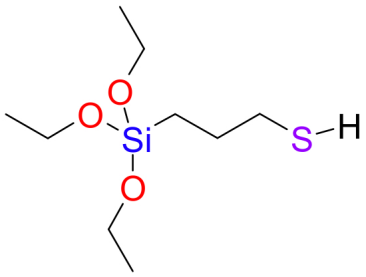

Figure 5.3: β-mercaptotriethoxysilane (thiol).

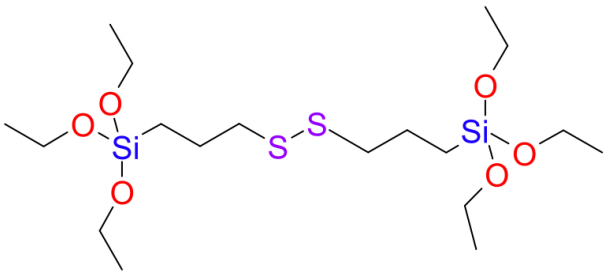

Figure 5.4: Bis(3-triethoxysilylpropyl) disulfide (disulfide).

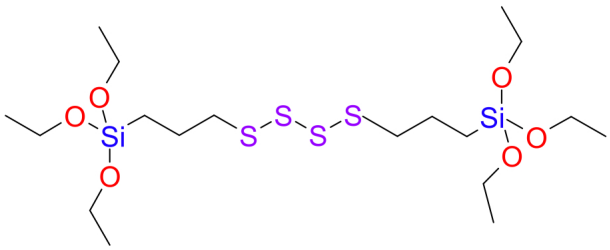

Figure 5.5: Bis(3-triethoxysilylpropyl) tetrasulfide (Si-69).

The thiol molecule is related to the other two, but is the most distinct. It is smaller, and is the only one with the S-H functionality, which is the at the end of the hydrocarbon chain instead of in the middle as the sulfurs in the other molecules are. The disulfide term provides the relevant information without requiring the long chemical name in writing. The other two molecules are very

similar. The three molecules have replaceable ethoxy groups on the silane, and the hydrocarbon and sulfur components would be similar to rubber, making the miscibility plausible.

5.2 Experimental Methods

The *in situ* FTIR reactor details of chapter three remain the same, and ZrO_2 (Sigma-Aldrich powder with less than 50 nm diameter) powder pressed into titanium grids was used as the substrate. The reactions were carried out in a viscous nitrogen gas flow, with the reactants controllably dosed in on top of the carrier gas base pressure of 1.25 Torr. Goodyear supplied chopped Kevlar fibers for coating, which were yellow and tended to cling together. The initial look at the chopped Kevlar fiber sample assured us that the fibers could be coated with aluminum oxide. Once that had been determined, the Kevlar was replaced with zirconium oxide coated with aluminum oxide for the rest of the functionalization experiments. For that brief examination, the Kevlar hung suspended between two grids, since pressing the sample into the grid would not have worked. Also, offsite testing took place in a fluidized bed reactor at ALD NanoSolutions. The trimethyl aluminum was 97 % pure from Sigma-Aldrich, and the other three molecules are (90 % pure or better from Sigma Aldrich). The carrier nitrogen was ultra-high purity grade, and the liquids were freeze-pump-thawed to remove extraneous volatile chemicals.

5.3 Results and Discussion

5.3.1 *in situ* FTIR characterization of surface changes

Once it was determined that aluminum oxide would deposit on the Kevlar by our collaborators at ALD Nanosolutions, and by examination with FTIR, a model substrate of zirconium oxide powder coated in situ with ALD aluminum oxide was substituted during the functionalization studies. Zirconium oxide powder is easily made into samples suitable for transmission FTIR study, the primary *in situ* analysis technique carried out during these experiments.

High surface area zirconium oxide powder coated with ALD alumina to provided a reactive surface

equivalent to Kevlar coated with ALD alumina. In situ FTIR showed the expected peaks of the well characterized Al_2O_3 chemistry. Then the alumina surface was dosed with the three different molecules during separate experiments. The resulting infrared spectrum is shown in figure 5.6 as difference spectra between the 3-mercaptotriethoxysilane, disulfide, or Si-69 and the fresh ALD alumina surface, so that the zirconium oxide and aluminum oxide stretches are not shown. This allows the focus on the addition and subtraction of chemical features due solely to the precursor functionalization of the surface. In figure 5.6, the absorbance versus frequency shows that the hydrogen-oxygen bonds in hydroxyl groups decreased, and that stretches due to C-H, C-O, Si-O were then present, as well as Si-O-Si and C-O-Si bends.

According to previous studies on siloxanes in sol gel chemistry, the reaction of the silicon with a hydroxyl group, replacing the ethoxide with a different oxygen, is quite likely. The loss of hydroxyl group stretches indicate that either the hydrogen was replaced, possibly with silicon, or that the entire functionality was removed. The presumption of the sol-gel chemistry is that the hydrogen on the oxygen was replaced with the silicon of the silane. The surface siloxane assignments are from Puomi.[138] Looking at rest of the transition energies, the C-H stretch locations are typical of symmetric (2853 cm^{-1}), and asymmetric ethylene (2912, 2930 cm^{-1}), and CH_2 bend at 1440 cm^{-1}. In addition, the peak at 1170 cm^{-1} corresponds to C-O stretch, probably from the ethoxide groups attached to silicon. This points to unreacted groups that remained on the silicon atom. Since there are three on each, that could mean that one or two stay with their parent molecule, and are present at the surface. Further evidence is provided by the peak at 1080 cm^{-1}, which is indicative of a bending motion of silicon and carbon with an oxygen between them. Interestingly, a peak due to Si-O-Si bend is present in significant portion, so the parent molecules must get close enough to interact through oxygen. The cross section of infrared absorption for S-H is very low, and though it was expected at 2600 cm^{-1}, its absence does not prove that the bond is absent. It might still be present and not absorbing enough to provide signal compared to the noise. Previous surface work in the reactor with H_2S did not result in FTIR visible H-S stretching either, and and we conclude that the peak is very hard to observe. Soft self-limiting behavior was observed, leading

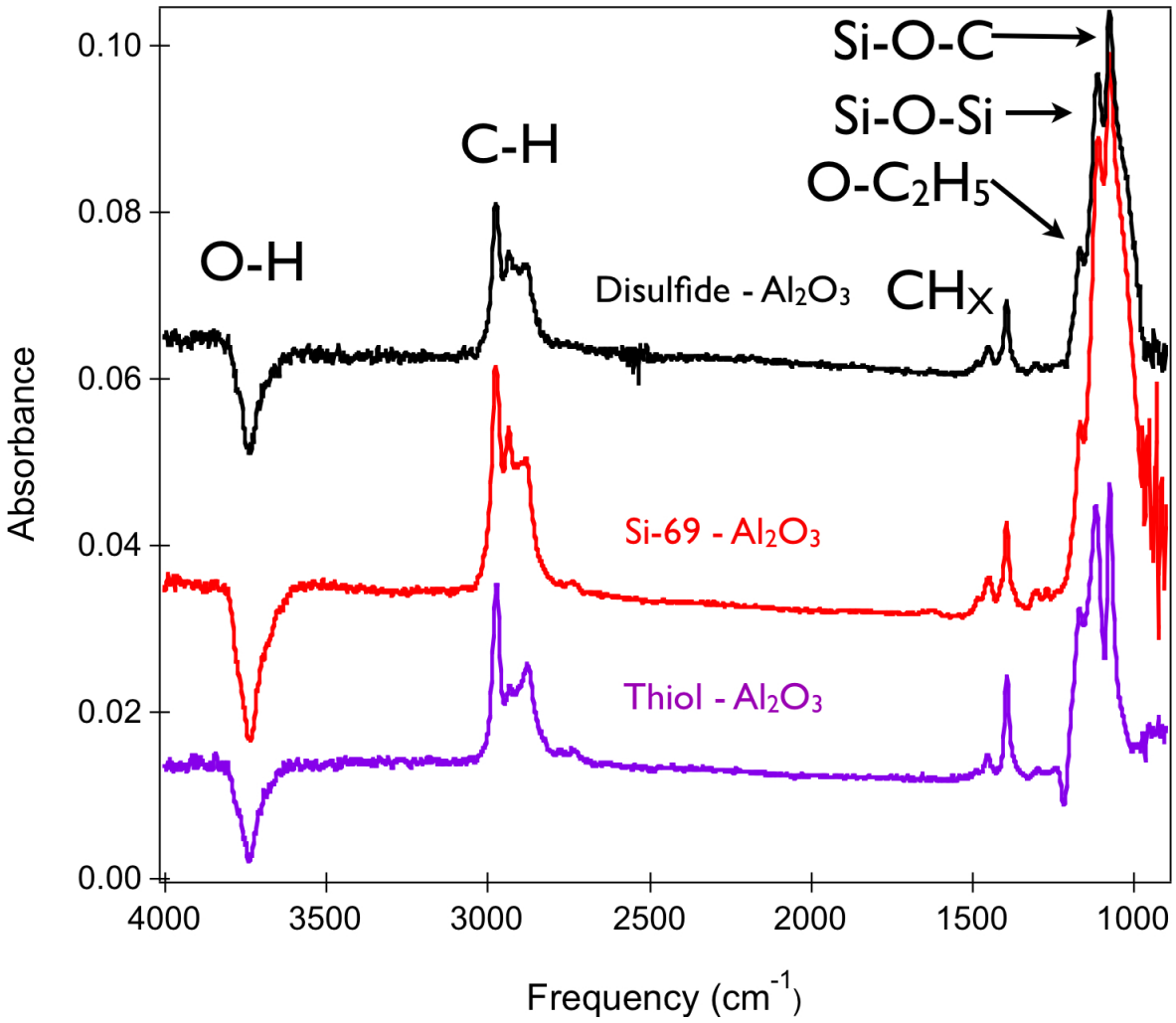

Figure 5.6: Thiol, Si-69, and Disulfide difference spectra on alumina at 150 °C

to the likelihood that once sites with more facile reactions had mostly reacted, some secondary, less easily reacted sites were still present, but the reaction was less efficient. By probability arguments, the reaction will slow as sites become less available.

The reaction of the thiol was examined at 125, 150, and 175 °C, and appeared similar at all three temperatures. The other two molecules were reacted at 150, 175, and 200 °C, and also appeared similar. The higher temperature was partly from curiosity, and partly because the heavier molecules were harder to vaporize, and therefore the higher temperatures helped avoid condensation. For comparison's sake, the three molecules are shown at 175 °CC in figure 5.7.

The area under the peaks gives information on the relative amounts of present, according to Beer-Lambert Law, but the different samples need normalization for a quantitative comparison. The amount of surface area in the IR beam path varies between grids because the ZrO_2 powder amount, while similar, does not stay constant. Therefore, the efficiency of the reaction was examined by comparing the free hydroxyls lost to the initial free hydroxyls on the surface. "Free" hydroxyl groups are those that show up in a narrow band at higher frequency, and are not hydrogen bonded to one another. These more isolated reactive sites tend to react more readily than their hydrogen-bonded counterparts. Hydrogen-bound hydroxyls on metal oxides, by contrast, stretch at lower frequencies, and over a broader range. Higher electron density between nuclei keep the vibration at a higher frequency, while a hydrogen bonded hydroxyl donates some electron density probability away from the primary bond, weakening the attractive forces and lowering the energy and oscillation speed of the nuclei, changing the transition energies in the potential well, and meaning that the strength of the bond and the frequency of the stretch is lower. In addition, the range of bond strengths widens depending on the environment, since the intermolecular bonds influence the hydrogen-oxygen bond strength to different degrees. The reactions would need repeating to allow firm quantitative conclusions, but do give suggestive information. The thiol coverage did not change greatly with temperature in the tested window, according to the ratio of hydroxyls lost to starting free hydroxyl groups.

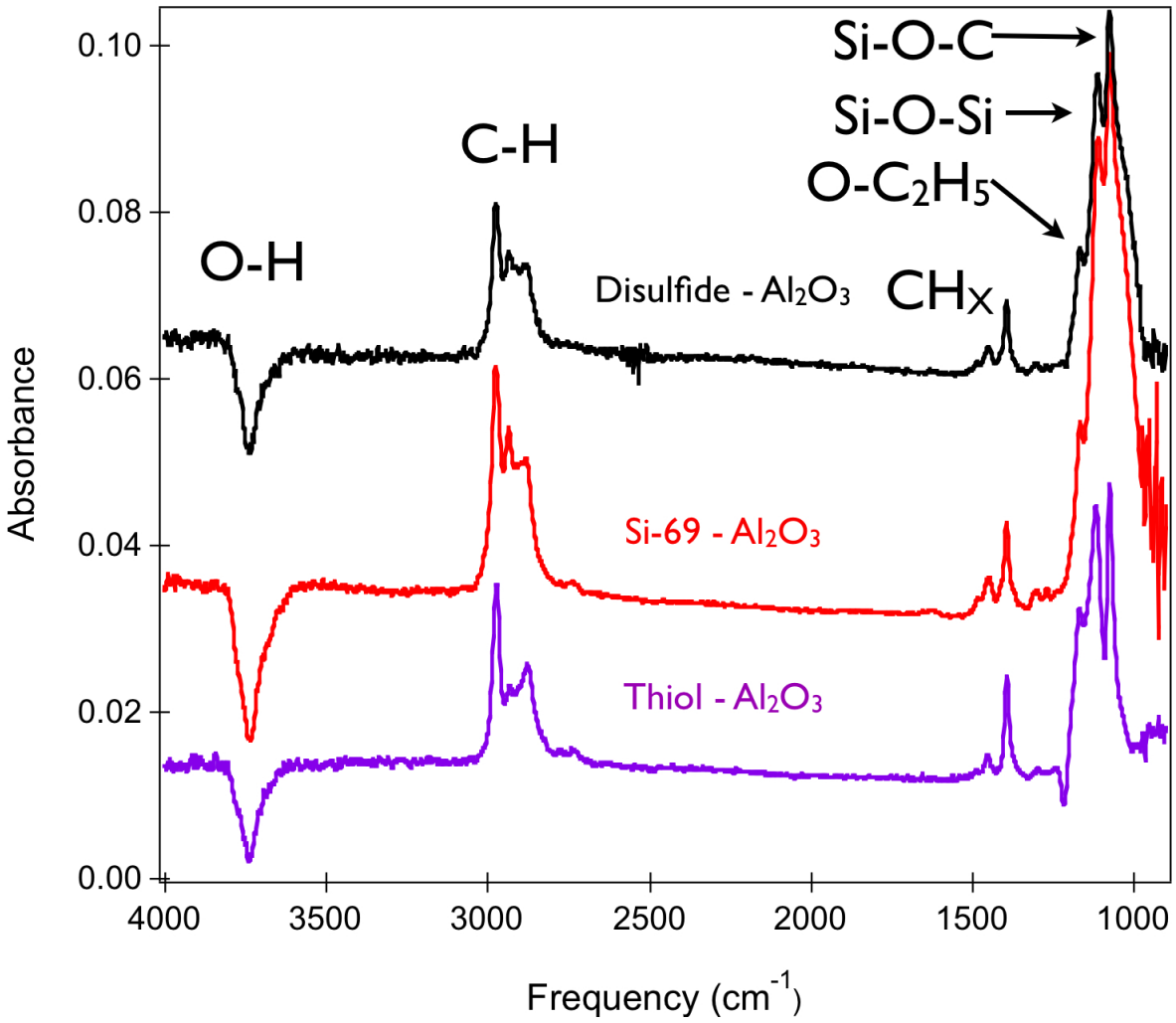

Figure 5.7: Thiol, Si-69, and Disulfide difference spectra on alumina at 175 °C.

Temperature	125	150	175	200 °C
Thiol	0.44	0.40	0.31	NA
Disulfide	NA	0.29	0.63	0.44
Si-69	NA	0.73	0.78	0.55

Table 5.1: Ratio of hydroxyls removed to starting hydroxyls.

As mentioned, the thiol ratio did not change much. At lower temperatures, the hydroxyls on the surface packed more densely, but looking at the ratio is more about checking the efficiency of the reaction by examining the proportion of easily accessible surface sites that react. For the other two less volatile precursors, the temperature was elevated to about 60 °C, and to make sure that condensation was not a factor in the reaction, the reaction temperature was not done as low as 125 °C. Rather, the disulfide and tetrasulfide molecules were examined at 150, 175, and 200 °C. The higher reacted hydroxyl ratio reached by the bi-functional molecules is interesting. The disulfide molecules demonstrated what seems to be an outlier at 150 °C, where the ratio is 0.3, meaning less than a third of the hydroxyls reacted. Otherwise the disulfide numbers are in line with Si-69, which shows no big difference between 150 and 175, and a drop at 200 °C. The speculative explanation includes some assumptions. As sites are reacted, nearby sites are less likely to react, whether because approaching gaseous molecules encounter sterically hindered hydroxyl molecules, or because the surface silicon causes the hydroxyl groups to become less reactive. When the molecules are singly reactive, once a molecule is attached it makes further attachment less likely. If a molecule is bi-reactive, the same arguments apply, but though it may take time for the other end of the molecule to react, it is bound through carbons and sulfurs to the surface, and will eventually find and react with a nearby site. Whether the amount of sulfur in the molecule has any effect beyond changing the molecular dimensions is unknown. If the disulfide point at 150 °C was really more in line with the thiol than the tetrasulfide containing Si-69, one could speculate that some molecules split into thiols when exposed to the surface.

Once the molecules were on the surface, they seemed stable in the reactor over time. To check the

stability under conditions more relevant than an inert atmosphere, the functionalized surface was exposed to water and examined with FTIR. The included Figures 5.8 and 5.9 represent the typical results of dosing water onto a saturated surface. Following the water, the surface was re-exposed to the sulfurous silane of the experiment, to see if it was possible to increase the coverage density.

Whether coated with thiol, disulfide, or tetrasulfide, exposing the functionalized Kevlar to atmospheric water levels removed many of the molecules added during dosing. All three molecules exhibited similar behavior when exposed to water. In each case, it made little difference whether the temperature was 150 or 175 °C. When the surface that had been functionalized and then exposed to water, was dosed again with the functional molecules, the surface appeared to return to a coverage level similar to the one during the initial exposure. The proportions changed slightly, with relatively fewer C-H stretches and C-O-Si bends compared to Si-O-Si bends. There is a possibility that more ethyl alcohol groups were removed, and the water encouraged surface bound silicons to form silicon-oxygen-silicon links. The loss of coverage on the surface during water exposure meant that under the processing conditions that tire rubber undergoes, there was a chance that many bonds would be severed, and this would limit the molecule density on the surface to some low number based on stability rather than initial loading. Preferably, the molecules would be attached to the surface at the density level determined to be ideal to enhance mixing with the rubber, and would then be stable during processing. The fact that water was able to displace a significant number of bonds was not ideal.

The amorphous alumina grown by ALD has been known to be susceptible to hydrolysis reactions, and since it is being used as the adhesion layer, it may be the cause of the problem. One of the solutions, in that case, is to use a different or additional adhesion layer. Titanium oxide is another well studied ALD material that can be deposited at a range of temperatures, all within the 125 to 200 °C window, and is likely to have the surface hydroxyl moieties attached to allow surface functionalization similar to alumina. In addition, ALD titania has been found to be less susceptible to dissolving in water.

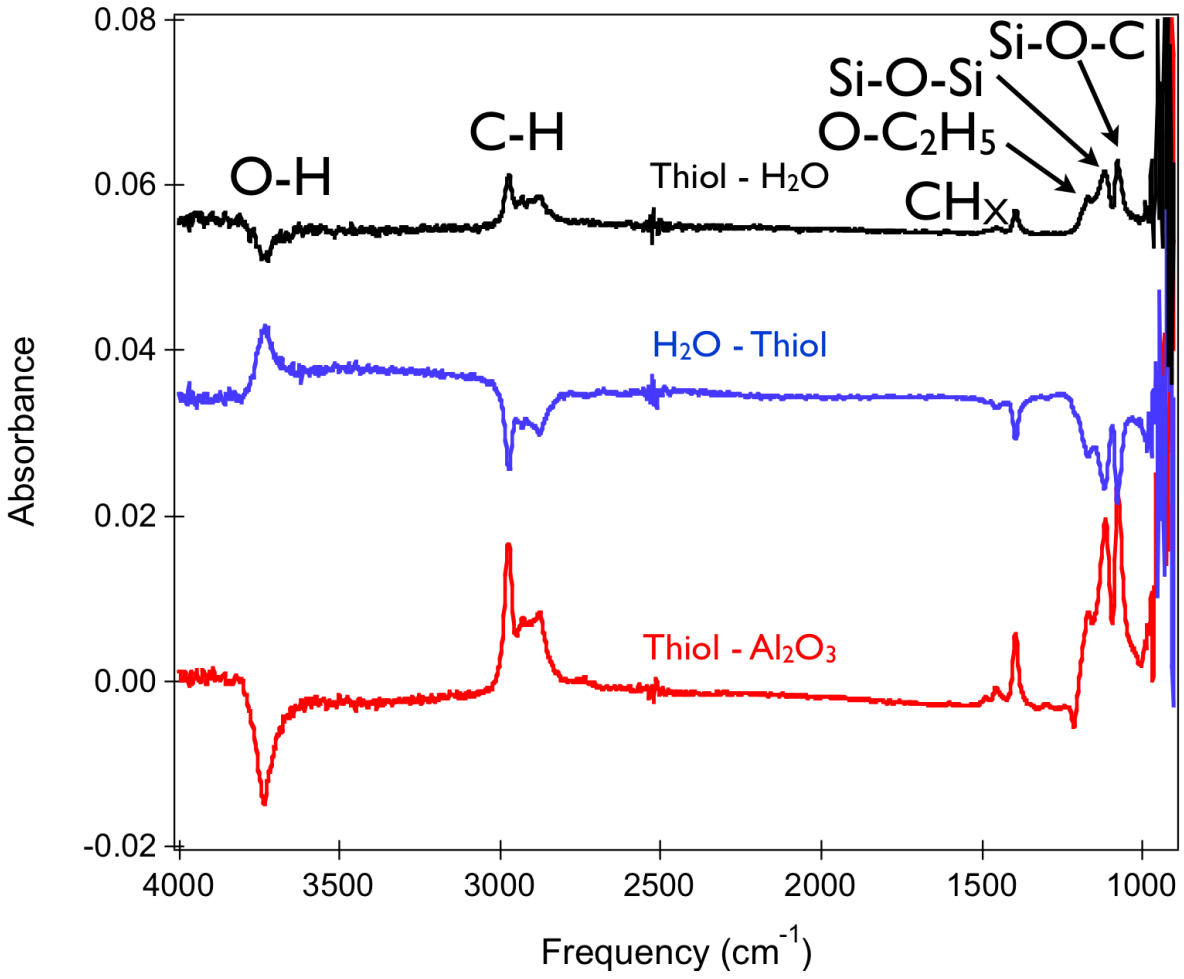

Figure 5.8: Difference spectra of a thiol, water, thiol dosing sequence on alumina at 175 °C.

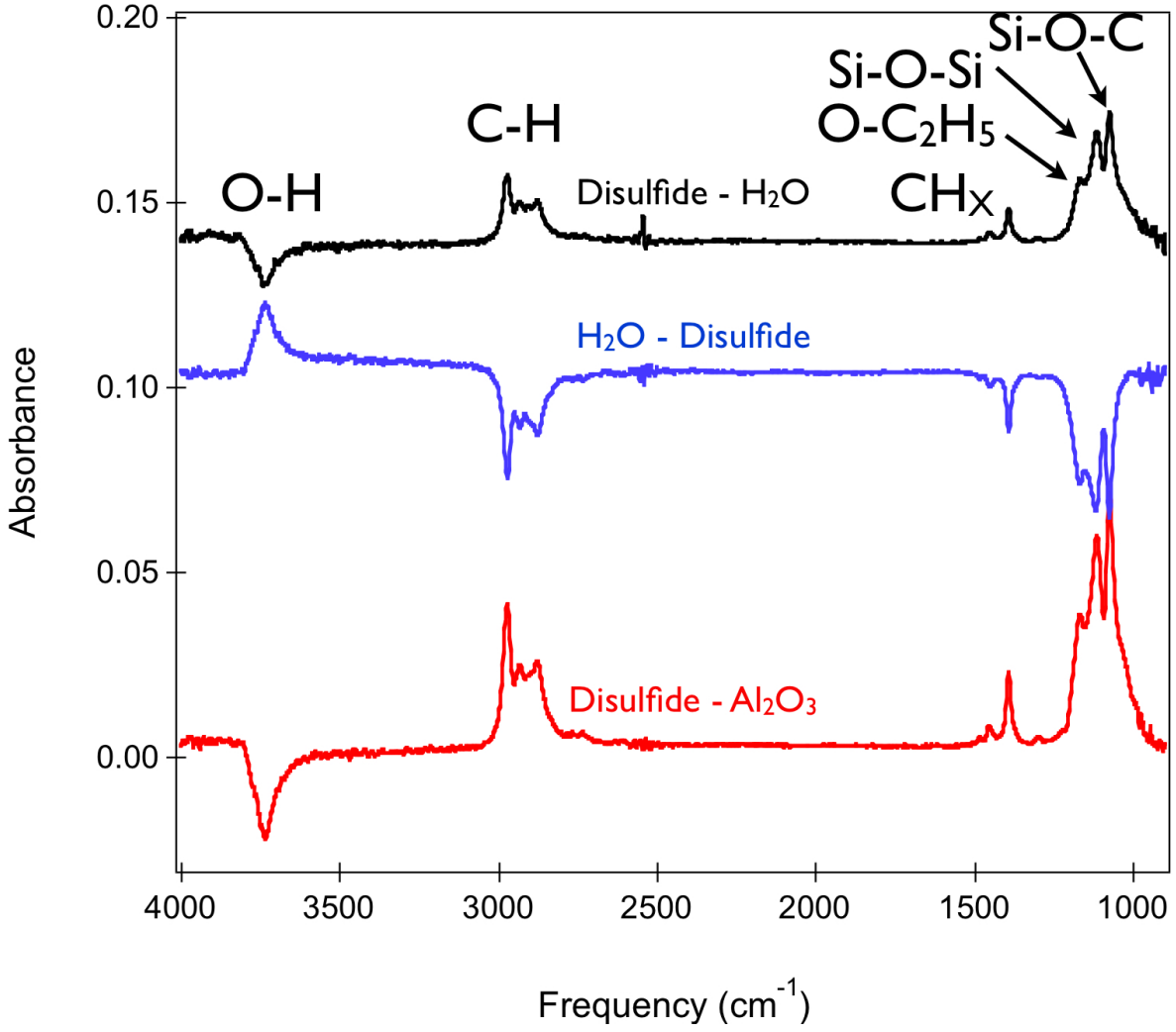

Figure 5.9: Difference spectra of a disulfide, water, disulfide dosing sequence on alumina at 175 °C

For testing this, a very thin layer of ALD titania was grown on fresh ALD alumina on zirconia particles. Then the hydroxyl terminated surface was exposed to disulfide molecules at the same three temperatures as in the experiment before. The disulfide molecules attached to the surface with very similar exchanges taking place. When the disulfide coated surface was exposed to water, very little change was observed. Proportionally, on TiO_2, less of the ligand stretches were removed on exposure than on Al_2O_3, and interestingly, upon dosing the disulfide after that, the densification of the surface was enhanced, since more molecules attached than had been seen under the initial saturation conditions.

The results at 150 and 175 °C looked very similar. In order to compare the removal of molecules from both TiO_2 and Al_2O_3, the ratio of C-H stretch lost under water dosing was related to the initial C-H stretch for disulfide molecules.

Temperature	TiO_2	Al_2O_3
150 °C	0.17	0.52
175 °C	0.19	0.63

Table 5.2: Ratio of C-H removed to starting C-H for disulfide.

This means that by using water, a wider range of surface coverage is attainable. The saturation mark changed when water was employed as a dosing agent. This is probably because the water exposure encourages silicon-oxygen-silicon linkages by displacing the ethoxy groups of the disulfide while bound to the surface, and creating new sites for additional molecules to bind. This allows more opportunity for optimization of the miscibility of the Kevlar with rubber.

The change in solubility of the previously immiscible Kevlar and vulcanized rubber under one set of temperature would be a more straitforward question than the actual question for tire performance. For tires, rubber is taken through many stages of temperatures and chemical additives, in a complex recipe that is determined phenominalogically, because it would be very difficult to predict. The mixture therefore would need to be compatible under a range of conditions, and probably only by full processing would the end homogeneity be knowable. This makes characterizing the success of

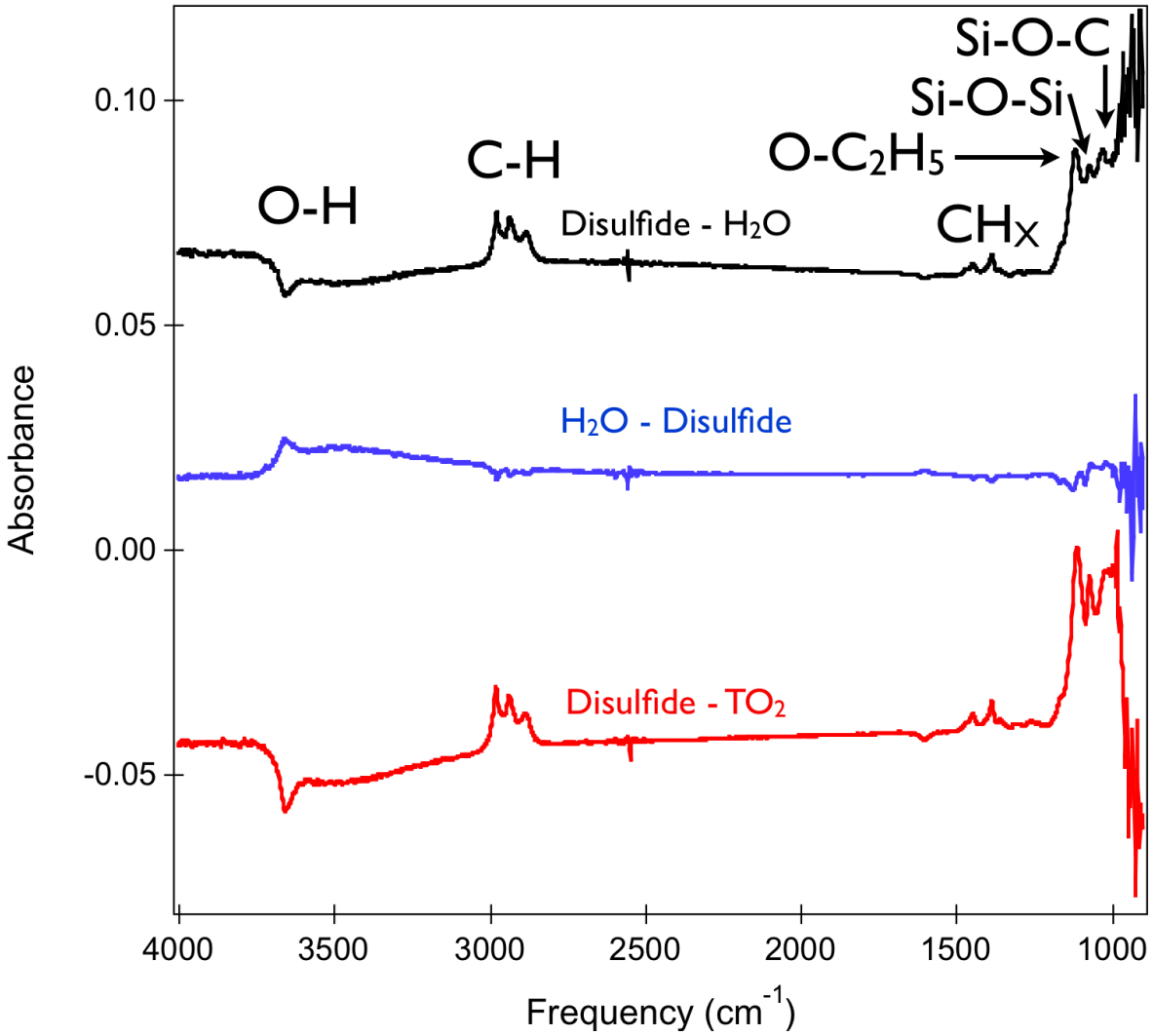

Figure 5.10: Difference spectra of a disulfide, water, disulfide dosing sequence on titania at 150 °C

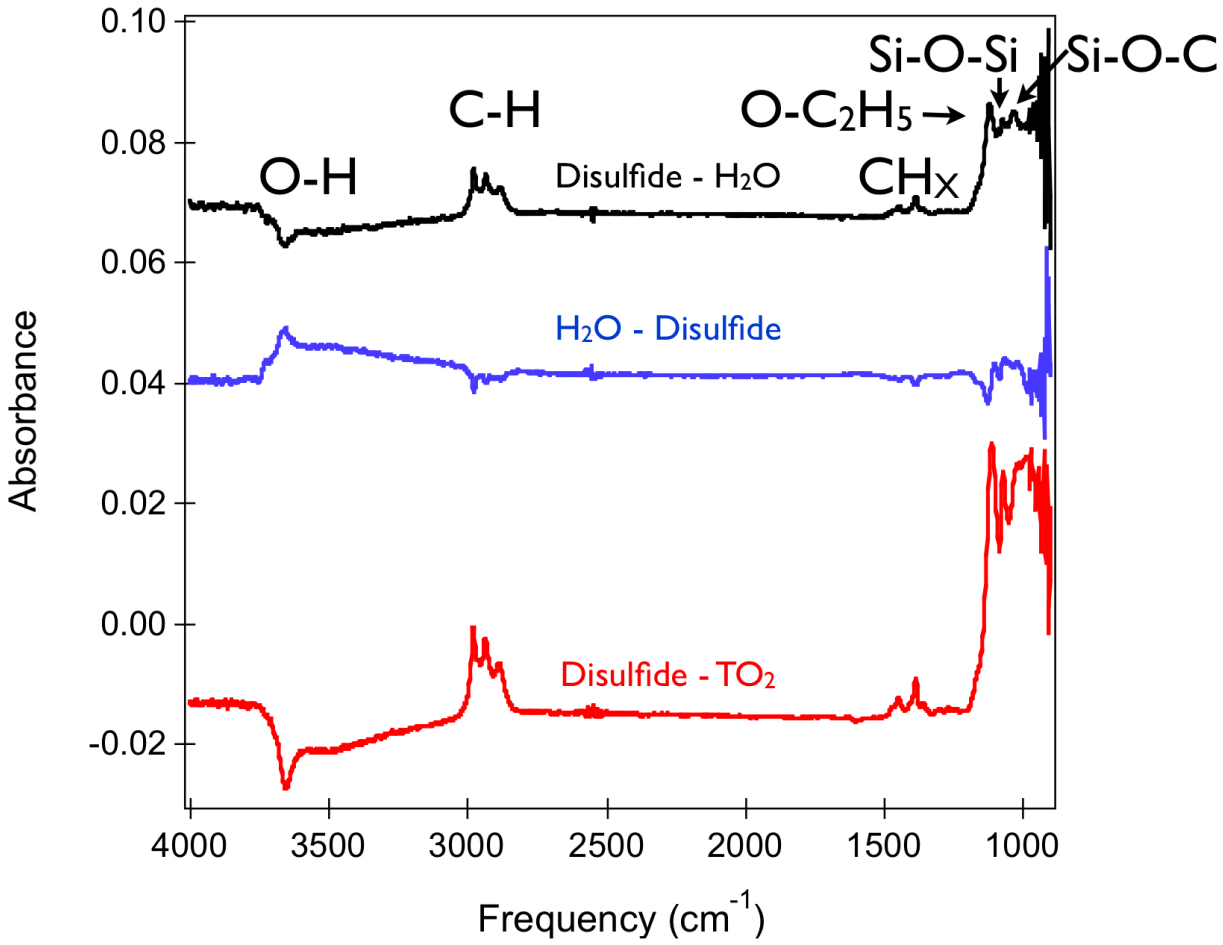

Figure 5.11: Difference spectra of a disulfide, water, disulfide dosing sequence on titania at 175 °C

the surface functionality more complicated, because it would require the full process rather than simply determining the initial homogeneity/heterogeneity.

Scaling up the deposition would be likely to need a fluidized bed system, so the volatility of the precursor would be important. Disulfide and Si-69 take a similar temperature to vaporize, and the thiol molecule requires less heat. The presumption is that the majority of the thiol S-H bonds would be intact on the functionalized Kevlar, which would cause different interactions with the sulfurs of the rubber, and may have an affect on the dispersion.

5.4 Conclusion

In order to make tires lighter, a high strength low density rubber filler would be important. Some high strength, low density materials do not mix well with rubber. In order to increase the miscibility of Kevlar and tire rubber, this project focused on modifying the surface functionality of the Kevlar using atomic layer deposition. Because aluminum oxide can be deposited on polymers, the primary interest was reacting heterofunctional molecules with Al_2O_3 and checking their coverage and stability on the surface. In the future the miscibility of the functionalized substrate could be checked for miscibility with the rubber mixture, even when taken through the tire forming process. In order to enhance the attraction between of the particles for rubber, the molecules used to functionalize the surface were similar to rubber, in that they were alkane chains and included sulfur. It is well known that siloxane based molecules react with metal oxides. There were three siloxane based molecules tried, a thiol (β-mercaptotriethoxysilane), a disulfide (bis(3-triethoxysilylpropyl) disulfide), and a tetrasulfide (bis(3-triethoxysilylpropyl) tetrasulfide or Si-69, an industrially used molecule). All three molecules attached to aluminum oxide. When exposed to water vapor, however, many of the molecules were replaced with hydroxyl groups on the surface, meaning that under typical atmospheric conditions the surface would be expected to lose the freshly attached functionalization. The primer layer was very important for stability of the molecular attachments, with TiO_2 bettering Al_2O_3 during water exposure. When the siloxanes attached to TiO_2, in fact,

very little hydroxyl replacement happened during water dosing. Not only that, but FTIR data indicated that silicon oxygen-silicon links became more prevalent, and what had previously been apparently siloxane saturated had more sites for more siloxane to react with, leading to higher coverage possibilities, and making it unlikely that the surface would change significantly upon exposure to ambient conditions. The change in the Kevlar fiber surface could lead to improved mixing with rubber, allowing it to be used as tire filler. With the low density and strong polymer replacing carbon black or silica as the strengthening agents in tires, the weight of the tires could decrease, causing increases in fuel efficiency in cars.

5.5 Acknowledgments

This work was funded by Goodyear, done in collaboration with ALD Nanosolutions, and greatly aided by ideas from Younghee Lee.

Bibliography

[1] Mikko Ritala, Kaupo Kukli, Antti Rahtu, Petri I. Raisanen, Markku Leskela, Timo Sajvaara, and Juhani Keinonen. Atomic Layer Deposition of Oxide Thin Films with Metal Alkoxides as Oxygen Sources. Science, 288(5464):319–321, April 2000.

[2] D N Goldstein, J A McCormick, and S M George. Al_2O_3 Atomic Layer Deposition with Trimethylaluminum and Ozone Studied by in Situ Transmission FTIR Spectroscopy and Quadrupole Mass Spectrometry. Journal of Physical Chemistry C, 112(49):19530–19539, 2008.

[3] M Ahonen, M Pessa, T Suntola, and Oy Lohja Ab. A Study of ZnTe Films Grown on Glass Substrates Using an Atomic Layer Evaporation Method. Thin Solid Films, 65:301–307, 1980.

[4] Ville Miikkulainen, Markku Leskela, Mikko Ritala, and Riikka L. Puurunen. Crystallinity of Inorganic Films Grown by Atomic Layer Deposition: Overview and General Trends. Journal of Applied Physics, 113(2):021301, 2013.

[5] Jinhee Kwon, Min Dai, Mathew D. Halls, Erik Langereis, Yves J. Chabal, and Roy G. Gordon. In Situ Infrared Characterization during Atomic Layer Deposition of Lanthanum Oxide. The Journal of Physical Chemistry C, 113(2):654–660, January 2009.

[6] Vikrant R Rai and Sumit Agarwal. Surface Reaction Mechanisms during Ozone-Based Atomic Layer Deposition of Titanium Dioxide. The Journal of Physical Chemistry C Letters, 112:9552–9554, 2008.

[7] W. M. M. Kessels, H. C. M. Knoops, S. A. F. Dielissen, A. J. M. Mackus, and M. C. M. van de Sanden. Surface Reactions During Atomic Layer Deposition of Pt Derived from Gas Phase Infrared Spectroscopy. Applied Physics Letters, 95(1):013114, 2009.

[8] P Bernhard, C Ziethen, R Ohr, H Hilgers, and G Schonhense. Investigations of the corrosion protection of ultrathin a-C and a-C : N overcoats for magnetic storage devices. Surface & Coatings Technology, 180:621–626, 2004.

[9] V Novotny, G Itnyre, A Homola, and L Franco. Corrosion of Thin-Film Cobalt Based Magnetic Recording Media. Ieee Transactions on Magnetics, 23(5):3645–3647, 1987.

[10] J Robertson. High Dielectric Constant Gate Oxides for Metal Oxide Si Transistors. Reports on Progress in Physics, 69(2):327–396, 2006.

[11] T Oikawa, M Nakamura, H Uwazumi, T Shimatsu, H Muraoka, and Y Nakamura. Microstructure and Magnetic Properties of CoPtCr-SiO_2 Perpendicular Recording Media. IEEE Transactions on Magnetics, 38(5):3, 2002.

[12] Qing Dai, Bing K Yen, Richard L White, Phillip J Peterson, and Bruno Marchon. Toward an Understanding of Overcoat Corrosion Protection. IEEE Transactions on Magnetics, 39(5):3, 2003.

[13] Kyoung-Ho Ahn, Young-Bae Park, and Dong-Wha Park. Kinetic and mechanistic study on the chemical vapor deposition of titanium dioxide thin films by in situ FT-IR using TTIP. Surface and Coatings Technology, 171(1-3):198–204, July 2002.

[14] M Ritala, M Leskela, E Nykanen, P Soininen, and L Niinisto. Growth of Titanium-Dioxide Thin-Films by Atomic Layer Epitaxy. Thin Solid Films, 225(1-2):288–295, 1993.

[15] M Ritala, M Leskela, L Niinisto, and P Haussalo. Titanium Isopropoxide as a Precursor in Atomic Layer Epitaxy of Titanium-Dioxide Thin-Films. Chemistry of Materials, 5(8):1174–1181, 1993.

[16] Q Xie, Y L Jiang, C Detavernier, D Deduytsche, R L Van Meirhaeghe, G P Ru, B Z Li, and X P Qu. Atomic Layer Deposition of TiO_2 from Tetrakis-dimethyl-amido Titanium or Ti Isopropoxide Precursors and H_2O. Journal of Applied Physics, 102(8):83521–83526, 2007.

[17] Stephen E. Potts, Gijs Dingemans, Christophe Lachaud, and W. M. M. Kessels. Plasma-Enhanced and Thermal Atomic Layer Deposition of Al_2O_3 Using Dimethylaluminum Isopropoxide, $[Al(CH_3)_2(\mu\text{-OiPr})]_2$, as an Alternative Aluminum Precursor. Journal of Vacuum Science & Technology A: Vacuum, Surfaces, and Films, 30(2):021505, 2012.

[18] J Aarik, A Aidla, T Uustare, M Ritala, and M Leskela. Titanium isopropoxide as a precursor for atomic layer deposition: characterization of titanium dioxide growth process. Applied Surface Science, 161(3-4):385–395, 2000.

[19] K B Ramos, G Clavel, C Marichy, W Cabrera, N Pinna, and Y J Chabal. In Situ Infrared Spectroscopic Study of Atomic Layer-Deposited TiO_2 Thin Films by Nonaqueous Routes. Chemistry of Materials, 25(9):1706–1712, 2013.

[20] Y W Kim and D H Kim. Atomic layer deposition of TiO_2 from Tetrakis-Dimethylamido-Titanium and Ozone. Korean Journal of Chemical Engineering, 29(7):969–973, 2012.

[21] M Rose, J Niinisto, P Michalowski, L Gerlich, L Wilde, I Endler, and J W Bartha. Atomic Layer Deposition of Titanium Dioxide Thin Films from Cp*$Ti(OMe)_3$ and Ozone. Journal of Physical Chemistry C, 113(52):21825–21830, 2009.

[22] S E Potts, W Keuning, E Langereis, G Dingemans, M C M van de Sanden, and W M M Kessels. Low Temperature Plasma-Enhanced Atomic Layer Deposition of Metal Oxide Thin Films. Journal of the Electrochemical Society, 157(7):P66–P74, 2010.

[23] M Schuisky, K Kukli, J Aarik, J Lu, and A Harsta. Epitaxial Growth of TiO_2 Films in a Hydroxyl-Free Atomic Layer Deposition Process. Journal of Crystal Growth, 235(1-4):293–299, 2002.

[24] P Gupta, A C Dillon, A S Bracker, and S M George. FTIR Studies of H_2O and D_2O Decomposition on Porous Silicon Surfaces. Surface Science, 245(3):360–372, 1991.

[25] M K Weldon, B B Stefanov, K Raghavachari, and Y J Chabal. Initial H_2O-Induced Oxidation of Si(100)-(2x1). Physical Review Letters, 79(15):2851–2854, 1997.

[26] P H Mutin and A Vioux. Nonhydrolytic Processing of Oxide-Based Materials: Simple Routes to Control Homogeneity, Morphology, and Nanostructure. Chemistry of Materials, 21(4):582–596, 2009.

[27] R J P Corriu, D Leclercq, P Lefevre, P H Mutin, and A Vioux. Preparation of Monolithic Metal-Oxide Gels by a Non-Hydrolytic Sol-Gel Process. Journal of Materials Chemistry, 2(6):673–674, 1992.

[28] Guylhaine Clavel, Erwan Rauwel, Marc-Georg Willinger, and Nicola Pinna. Non-aqueous Sol-gel Routes Applied to Atomic Layer Deposition of Oxides. Journal of Materials Chemistry, 19(4):454, 2009.

[29] P I Raisanen, M Ritala, and M Leskela. Atomic Layer Deposition of Al_2O_3 Films Using $AlCl_3$ and Al((OPr)-Pr-i)$_3$ as Precursors. Journal of Materials Chemistry, 12(5):1415–1418, 2002.

[30] K Kukli, M Ritala, and M Leskela. Atomic layer deposition and chemical vapor deposition of tantalum oxide by successive and simultaneous pulsing of tantalum ethoxide and tantalum chloride. Chemistry of Materials, 12(7):1914–1920, 2000.

[31] W K Kim, S W Rhee, N I Lee, JH Lee, and HK Kang. Atomic layer deposition of hafnium silicate thin films using hafnium tetrachloride and tetra-n-butyl orthosilicate. Journal of Vacuum Science & Technology A, 22(4):1285–1289, 2004.

[32] W K Kim, S W Kang, S W Rhee, N I Lee, J H Lee, and H K Kang. Atomic layer deposition of Zirconium Silicate Films Using Zirconium Tetrachloride and Tetra-n-Butyl Orthosilicate. Journal of Vacuum Science & Technology A-Vacuum Surfaces and Films, 20(6):2096–2100, 2002.

[33] Antti Rahtu, Mikko Ritala, and Markku Leskela. Atomic Layer Deposition of Zirconium Titanium Oxide from Titanium Isopropoxide and Zirconium Chloride. Chemistry of Materials, 13(2):1528–1532, 2001.

[34] P Arnal, R J P Corriu, D Leclercq, P H Mutin, and A Vioux. A Solution Chemistry Study of Nonhydrolytic Sol-Gel Routes to Titania. Chemistry of Materials, 9(3):694–698, 1997.

[35] Virginia R. Anderson, Andrew S. Cavanagh, Aziz I. Abdulagatov, and Zachary M. Gibbs. AVS 57th International Symposium & Exhibition, Albuquerque, NM. In Waterless TiO_2 Atomic Layer Deposition using Titanium Tetrachloride and Titanium Tetraisopropoxide, 2010.

[36] R P Chaukulkar and S Agarwal. Atomic layer deposition of titanium dioxide using titanium tetrachloride and titanium tetraisopropoxide as precursors. Journal of Vacuum Science & Technology A, 31(3), 2013.

[37] Titta Aaltonen, Antti Rahtu, Mikko Ritala, and Markku Leskela. Reaction Mechanism Studies on Atomic Layer Deposition of Ruthenium and Platinum. Electrochemical and Solid-State Letters, 6(9):C130, 2003.

[38] Frank Wallrapp and Peter Fromherz. TiO_2 and HfO_2 in electrolyte-oxide-silicon configuration for applications in bioelectronics. Journal of Applied Physics, 99(11):114103, 2006.

[39] Martin Frank. Atomic Layer Deposition for CMOS Scaling: High-k Gate Dielectrics on Si, Ge, and III-V Semiconductors. ECS Transactions, 11(7):187–200, 2007.

[40] Simon D Elliott. Atomic-scale Simulation of ALD. Semiconductor Science and Technology, 27:074008, 2012.

[41] Ulrike Diebold. The Surface Science of Titanium Dioxide. Surface Science Preports, 48:53–229, 2003.

[42] S Sankar and K G Gopchandran. Effect of Annealing on the Structural, Electrical and Optical Properties of Nanostructured TiO_2 Thin Films. Crystal Research and Technology, 44(9):989–994, 2009.

[43] Markku Leskelä and Mikko Ritala. Atomic Layer Deposition Chemistry: Recent Developments and Future Challenges. Angewandte Chemie (International ed. in English), 42(45):5548–54, November 2003.

[44] M Horprathum, P Chindaudom, P Limnonthakul, P Eiamchai, N Nuntawong, V Patthanasettakul, A Pokaipisit, and P Limsuwan. Fabrication and Characterization of Hydrophilic TiO_2 Thin Films on Unheated Substrates Prepared by Pulsed DC Reactive Magnetron Sputtering. Journal of Nanomaterials, 2010, 2010.

[45] Jolien Dendooven, Sreeprasanth Pulinthanathu Sree, Koen De Keyser, Davy Deduytsche, Johan A Martens, Karl F Ludwig, and Christophe Detavernier. In Situ X-ray Fluorescence Measurements During Atomic Layer Deposition : Nucleation and Growth of TiO_2 on Planar Substrates and in Nanoporous Films. Journal of Physical Chemistry C, 115(14):6605–6610, 2011.

[46] David N. Goldstein, Jarod A. McCormick, and Steven M. George. Al_2O_3 Atomic Layer Deposition with Trimethylaluminum and Ozone Studied by in Situ Transmission FTIR Spectroscopy and Quadrupole Mass Spectrometry. The Journal of Physical Chemistry C, 112(49):19530–19539, December 2008.

[47] J. W. Elam, M. D. Groner, and S. M. George. Viscous Flow Reactor with Quartz Crystal Microbalance for Thin Film Growth by Atomic Layer Deposition. Review of Scientific Instruments, 73(8):2981, 2002.

[48] W Hertl. Surface Chemistry of Zirconia Polymorphs. Langmuir, 5:96–100, 1989.

[49] M Sibeijn, R Spronk, J A R van Veen, and J C Mol. IR Studies of Re_2O_7 Metathesis Catalysts Supported on Alumina and Phosphated Alumina. Catalysis Letters, 8:201–208, 1991.

[50] Paul D Moran, Graham A Bowmaker, Ralph P Cooney, Kim S Finnie, Rohn R Bartlett, and James L Woolfrey. Vibrational Spectra and Molecular Association of Titanium Tetraisopropoxide. Inorganic Chemistry, 37:8, 1998.

[51] Vikrant R Rai and Sumit Agarwal. Surface Reaction Mechanisms during Ozone-Based Atomic Layer Deposition of Titanium Dioxide. Journal of Physical Chemistry C, 112:3, 2008.

[52] J D Ferguson, A R Yoder, A W Weimer, and S M George. TiO_2 Atomic Layer Deposition on ZrO_2 Particles Using Alternating Exposures of $TiCl_4$ and H_2O. Applied Surface Science, 226(4):393–404, 2004.

[53] A Gomezcarrera, M Mena, P Royo, and R Serrano. Halo(Alkoxo) and Monocylopentadienyl(Halo)Alkoxo Derivatives of Titanium, Zirconium and Hafnium. Journal of Organometallic Chemistry, 315(3):329–335, 1986.

[54] W B Person and W B Maier. Absolute Integrated-Intensities of Infrared-Absorption Bands of $TiCl_4$. Journal of Chemical Physics, 69(1):297–299, 1978.

[55] P A Coon, M L Wise, A C Dillon, M B Robinson, and S M George. Diethylsilane on Silicon Surfaces: Adsorption and Decomposition Kinetics. Journal of Vacuum Science and Technology B, 10(1):221–227, 1992.

[56] T Busani and R A B Devine. Dielectric and infrared properties of TiO_2 films containing anatase and rutile. Semiconductor Science and Technology, 20(8):870–875, 2005.

[57] T Nakayama. Structure of TiO_2/SiO_2 Multilayer Films. Journal of the Electrochemical Society, 141(1):237–241, 1994.

[58] Titta Aaltonen, Mikko Ritala, Yung-Liang Tung, Yun Chi, Kai Arstila, Kristoffer Meinander, and Markku Leskelä. Atomic Layer Deposition of Noble Metals: Exploration of the Low Limit of the Deposition Temperature. Journal of Materials Research, 19(11):3353–3358, March 2011.

[59] Junling Lu and Peter C Stair. Nano/Subnanometer Pd Nanoparticles on Oxide Supports Synthesized by AB-Type and Low-Temperature ABC-Type Atomic Layer Deposition: Growth and Morphology. Langmuir : the ACS journal of surfaces and colloids, 26(21):16486–95, November 2010.

[60] Arie J. Plomp, Heli Vuori, A. Outi I. Krause, Krijn P. de Jong, and Johannes H. Bitter. Particle Size Effects for Carbon Nanofiber Supported Platinum and Ruthenium Catalysts for the Selective Hydrogenation of Cinnamaldehyde. Applied Catalysis A: General, 351(1):9–15, December 2008.

[61] Steven T Christensen, Jeffrey W Elam, Federico A Rabuffetti, Qing Ma, Steven J Weigand, Byeongdu Lee, Soenke Seifert, Peter C Stair, Kenneth R Poeppelmeier, Mark C Hersam, and Michael J Bedzyk. Controlled Growth of Platinum Nanoparticles on Strontium Titanate Nanocubes by Atomic Layer Deposition. Small (Weinheim an der Bergstrasse, Germany), 5(6):750–757, March 2009.

[62] Titta Aaltonen, Mikko Ritala, Timo Sajavaara, and Juhani Keinonen. Atomic Layer Deposition of Platinum Thin Films. Chemistry of Materials, 15(17):1924–1928, 2003.

[63] Junling Lu and Peter C Stair. Low-Temperature ABC-Type Atomic Layer Deposition: Synthesis of Highly Uniform Ultrafine Supported Metal Nanoparticles. Angewandte Chemie (International ed. in English), 49(14):2547–51, March 2010.

[64] Arrelaine A. Dameron, Svitlana Pylypenko, Justin B. Bult, K.C. Neyerlin, Chaiwat Engtrakul, Christopher Bochert, G. Jeremy Leong, Sarah L. Frisco, Lin Simpson, Huyen N. Dinh, and Bryan Pivovar. Aligned Carbon Nanotube Array Functionalization for Enhanced Atomic Layer Deposition of Platinum Electrocatalysts. Applied Surface Science, 258(13):5212–5221, April 2012.

[65] Jihwan An, Young-Beom Kim, and Fritz B Prinz. Ultra-thin platinum catalytic electrodes fabricated by atomic layer deposition. Physical chemistry chemical physics : PCCP, 15(20):7520–5, May 2013.

[66] K Tammeveski, T Tenno, and J Niinisto. Thermal Preparation of Thin Platinum Coatings and their Electrochemical and Atomic Force Microscopic Characterization. Applied Surface Science156, 156:135–142, 2000.

[67] Aicheng Chen and Peter Holt-Hindle. Platinum-based nanostructured materials: synthesis, properties, and applications. Chemical reviews, 110(6):3767–804, June 2010.

[68] Jani Hämäläinen, Esa Puukilainen, Timo Sajavaara, Mikko Ritala, and Markku Leskelä. Low Temperature Atomic Layer Deposition of Noble Metals Using Ozone and Molecular Hydrogen as Reactants. Thin Solid Films, 531:243–250, March 2013.

[69] Jani Hämäläinen, Frans Munnik, Mikko Ritala, and Markku Leskela. Atomic Layer Deposition of Platinum Oxide and Metallic Platinum Thin Films from $Pt(acac)_2$ and Ozone. Chemistry of Materials, 20(9):6840–6846, 2008.

[70] L. Baker, A. S. Cavanagh, J. Yin, S. M. George, A. Kongkanand, and F. T. Wagner. Growth of continuous and ultrathin platinum films on tungsten adhesion layers using atomic layer deposition techniques. Applied Physics Letters, 101(11):111601, 2012.

[71] Xirong Jiang and Stacey F. Bent. Area-Selective Atomic Layer Deposition of Platinum on YSZ Substrates Using Microcontact Printed SAMs. Journal of The Electrochemical Society, 154(12):D648, 2007.

[72] M. Lashdaf, J. Lahtinen, M. Lindblad, T. Venäläinen, and A.O.I. Krause. Platinum Catalysts on Alumina and Silica Prepared by Gas- and Liquid- Phase Deposition in Cinnamaldehyde Hydrogenation. Applied Catalysis A: General, 276(1-2):129–137, November 2004.

[73] Yun Zhou, David M. King, Xinhua Liang, Jianhua Li, and Alan W. Weimer. Optimal Preparation of Pt/TiO_2 Photocatalysts Using Atomic Layer Deposition. Applied Catalysis B: Environmental, 101(1-2):54–60, November 2010.

[74] Constantin Vahlas and Mathieu Delmas. Platinum Protective Coatings Processed by Organometallic CVD. Chemical Vapor Deposition, 14(56):103–106, June 2008.

[75] Robert R. Hoover and Yuriy V. Tolmachev. Electrochemical Properties of Pt Coatings on Ni Prepared by Atomic Layer Deposition. Journal of The Electrochemical Society, 156(1):A37, 2009.

[76] Aarne Kasikov, Alar Gerst, Arvo Kikas, Leonard Matisen, Agu Saar, Aivar Tarre, and Arnold Rosental. Pt Coated Cr_2O_3 thin Films for Resistive Gas Sensors. Central European Journal of Physics, 7(2):356–362, April 2009.

[77] D.N. Goldstein and S.M. George. Surface Poisoning in the Nucleation and Growth of Palladium Atomic Layer Deposition with $Pd(hfac)_2$ and Formalin. Thin Solid Films, 519(16):5339–5347, June 2011.

[78] J.W. Elam, A. Zinovev, C.Y. Han, H.H. Wang, U. Welp, J.N. Hryn, and M.J. Pellin. Atomic Layer Deposition of Palladium Films on Al_2O_3 Surfaces. Thin Solid Films, 515(4):1664–1673, December 2006.

[79] Adriaan J. M. Mackus, Noémi Leick, Layton Baker, and Wilhelmus M. M. Kessels. Catalytic Combustion and Dehydrogenation Reactions during Atomic Layer Deposition of Platinum. Chemistry of Materials, 24(10):1752–1761, May 2012.

[80] Gabor A Somorjai and Anderson L Marsh. Active Sites and States in the Heterogeneous Catalysis of Carbon-Hydrogen Bonds. Philosophical transactions. Series A, Mathematical, physical, and engineering sciences, 363(1829):879–900; discussion 1035–40, April 2005.

[81] Steven T. Christensen and Jeffrey W. Elam. Atomic Layer Deposition of IrPt Alloy Films. Chemistry of Materials, 22(8):2517–2525, April 2010.

[82] Mark K Debe. Electrocatalyst Approaches and Challenges for Automotive Fuel Cells. Nature, 486(7401):43–51, June 2012.

[83] Yannick Garsany, Olga A Baturina, Karen E Swider-Lyons, and Shyam S Kocha. Experimental Methods for Quantifying the Activity of Platinum Electrocatalysts for the Oxygen Reduction Reaction. Analytical chemistry, 82(15):6321–8, August 2010.

[84] Michel Cassir, Armelle Ringuedé, and Lauri Niinistö. Input of atomic layer deposition for solid oxide fuel cell applications. Journal of Materials Chemistry, 20(41):8987, 2010.

[85] Frederick T. Wagner, Balasubramanian Lakshmanan, and Mark F. Mathias. Electrochemistry and the Future of the Automobile. The Journal of Physical Chemistry Letters, 1(14):2204–2219, July 2010.

[86] Jeffrey S King, Arne Wittstock, Juergen Biener, Sergei O Kucheyev, Yinmin M Wang, Theodore F Baumann, Sandeep K Giri, Alex V Hamza, Marcus Baeumer, and Stacey F Bent. Ultralow Loading Pt Nanocatalysts Prepared by Atomic Layer Deposition on Carbon Aerogels. Nano Letters, 8(8):2405–2409, 2008.

[87] L. Tamašauskait-Tamašinait, A. Balčinait, A. Vaiciukevičien, A. Selskis, and E. Norkus. Investigation of Electrocatalytic Activity of Titania Nanotube Supported Nanostructured PtNi Catalyst Towards Methanol Oxidation. Journal of Power Sources, 225:20–26, March 2013.

[88] Zaoxue Yan, Wei Wei, Jimin Xie, Suci Meng, Xiaomeng Lü, and Jianjun Zhu. An Ion Exchange Route to Produce WO_3 Nanobars as Pt Electrocatalyst Promoter for Oxygen Reduction Reaction. Journal of Power Sources, 222:218–224, 2013.

[89] Xirong Jiang, Hong Huang, Friedrich B Prinz, and Stacey F Bent. Application of Atomic Layer Deposition of Platinum to Solid Oxide Fuel Cells. Chemistry of Materials, 20(10):3897–3905, 2008.

[90] M. Perchthaler, T. Ossiander, V. Juhart, J. Mitzel, C. Heinzl, C. Scheu, and V. Hacker. Tungsten Materials as Durable Catalyst Supports for Fuel Cell Electrodes. Journal of Power Sources, 243:472–480, December 2013.

[91] Saskia Feast, Martin Englisch, Andreas Jentys, and Johannes A Lercher. Preparation and Characterization of Pt Particles in Unidimensional Microporous Supports. Applied Catalysis A: General, 174(1-2):155–162, November 1998.

[92] Nadja C Bigall and Alexander Eychmüller. Synthesis of noble metal nanoparticles and their non-ordered superstructures. Philosophical transactions. Series A, Mathematical, physical, and engineering sciences, 368(1915):1385–404, March 2010.

[93] You Han, Chang-Jun Liu, and Qingfeng Ge. Interaction of Pt Clusters with the Anatase TiO_2(101) Surface: A First Principles Study. The journal of physical chemistry. B, 110(14):7463–72, April 2006.

[94] James A Enterkin, Kenneth R Poeppelmeier, and Laurence D Marks. Oriented Catalytic Platinum Nanoparticles on High Surface Area. Nano Letters, 11:993–997, 2011.

[95] James A Enterkin, Worajit Setthapun, W Elam, Steven T Christensen, Federico A Rabu, Laurence D Marks, Peter C Stair, Kenneth R Poeppelmeier, and Christopher L Marshall. Propane Oxidation over $Pt/SrTiO_3$ Nanocuboids. ACS Catalysis, 1:629–635, 2011.

[96] Sergio Tosoni, Oriol Lamiel-garcia, Daniel Fernandez Hevia, Jose Miguel, and Francesc Illas. Electronic Structure of F-Doped Bulk Rutile, Anatase, and Brookite Polymorphs of TiO_2. The Journal of Physical Chemistry C, 116(23):12738–12746, 2012.

[97] Meredith C.K. Sellers and Edmund G. Seebauer. Measurement Method for Carrier Concentration in TiO_2 via the MottSchottky Approach. Thin Solid Films, 519(7):2103–2110, January 2011.

[98] J.-K. Lee, H.S. Jung, J.A. Valdez, M.F. Hundley, J.D. Thompson, K.E. Sickafus, M. Nastasi, D.W. Hamby, and D.A. Lucca. Room Temperature Ferromagnetism of Co Doped TiO_2 Using Ion Implantation and Defect Engineering. Nuclear Instruments and Methods in Physics Research Section B: Beam Interactions with Materials and Atoms, 250(1-2):279–282, September 2006.

[99] A.H. Mahan, P.A. Parilla, K.M. Jones, and A.C. Dillon. Hot-Wire Chemical Vapor Deposition of Crystalline Tungsten Oxide Nanoparticles at High Density. Chemical Physics Letters, 413(1-3):88–94, September 2005.

[100] James A Anderson. Infrared Study of the Oxidation of Carbon Monoxide over Pt/Al_2O_3. Journal of the Chemical Society, Faraday Transactions, 88(8):1197–1201, 1992.

[101] Robert K Brandt, M R Hughes, L P Bourget, K Truszkowska, and Robert G Greenler. The Interpretation of CO Adsorbed on Pt/SiO_2 of Two Different Particle-Size Distributions. Surface Science, 286:15–25, 1993.

[102] Alison Crossley and David A King. Infrared Spectra for CO Isotopes Chemisorbed on Pt (111): Evidence for Strong Absorbate Coupling Interactions. Surface Science, 68:528–538, 1977.

[103] B. E. Hayden and A. M. Bradshaw. The Adsorption of CO on Pt(lll) Studied by Inrared Reflection-Absorption Spectroscopy. Surface Science, 125:787–802, 1983.

[104] Xiaodong Wu, Li Zhang, Duan Weng, Shuang Liu, Zhichun Si, and Jun Fan. Total Oxidation of Propane on $Pt/WO_x/Al_2O_3$ Catalysts by Formation of Metastable $Pt\delta+$ Species Interacted with WO_x Clusters. Journal of hazardous materials, 225-226:146–154, July 2012.

[105] J Farkas, M. J. Hampden-Smith, and T. T. Kodas. FTIR Studies of the Adsorption/Desorption Behavior of Copper Chemical Vapor Deposition Precursors on Silica. 1. Bis(1,1,1,5,5,5-hexafluoroacetylacetonato)copper(II). Journal of Physical Chemistry, 98:6753–6762, 1994.

[106] Elizabeth L Crane, Yujian You, Ralph G Nuzzo, and Gregory S Girolami. Mechanistic Studies of CVD Metallization Processes : Reactions of Rhodium and Platinum beta-Diketonate Complexes on Copper Surfaces. Journal of the American Chemical Society, 122(13):3422–3435, 2000.

[107] Wenbin Lin, Benjamin C Wiegand, Ralph G Nuzzo, and Gregory S Girolami. Mechanistic Studies of Palladium Thin Film Growth from Palladium (II) beta-Diketonates . 1 . Spectroscopic Studies of the Reactions of Bis (hexafluoroacetylacetonato) palladium (II) on Copper Surfaces. Journal of the American Chemical Society, 118:5977–5987, 1996.

[108] S. Pinchas, Brian L. Silver, and I. Laulicht. Infrared Absorption Spectra of the 18O Labeled Acetylacetonates of Cr(III) and Mn(III). The Journal of Chemical Physics, 46(4):1506–1510, 1967.

[109] Melvin L. Morris, Ross W. Moshier, and Robert E. Sievers. Infrared Spectra of Metal Chelate Compounds of Hexafluoroacetylacetone. Notes in Inorganic Chemistry, pages 411–412, 1963.

[110] T. Kecskés, J. Raskó, and J. Kiss. FTIR and Mass Spectrometric Studies on the Interaction of Formaldehyde with TiO_2 Supported Pt and Au Catalysts. Applied Catalysis A: General, 273(1-2):55–62, October 2004.

[111] G Busca and V Lorenzelli. Infrared Spectroscopic Identification of Species Arising from Reactive Adsorption of Carbon Oxides on Metal Oxide Surfaces. Materials Chemistry, 7:89–126, 1982.

[112] Brian E. Hayden, Alex King, and Mark A. Newton. Fourier Transform ReflectionAbsorption IR Spectroscopy Study of Formate Adsorption on TiO_2 (110). The Journal of Physical Chemistry B, 103(1):203–208, January 1999.

[113] Yoon Seok Jung, Andrew S. Cavanagh, Anne C. Dillon, Markus D. Groner, Steven M. George, and Se-Hee Lee. Enhanced Stability of $LiCoO_2$ Cathodes in Lithium-Ion Batteries Using Surface Modification by Atomic Layer Deposition. Journal of The Electrochemical Society, 157(1):A75, 2010.

[114] Lucila P Mendez de Leo, Laurent Pirolli, and Andrew V Teplyakov. Chemistry of 1,1,1,5,5,5-Hexafluoro-2,4-pentaneione on Si(100)-2X1. Journal of Physical Chemistry B, 110(100):14337–14344, 2006.

[115] Gregory S Girolami, Patrick M Jeffries, and Lawrence H Dubois. Mechanistic Studies of Copper Thin-Film Growth from Cu (I) and Cu (II) beta-Diketonates. Journal of the American Chemical Society, 115:1015–1024, 1993.

[116] Augusta M. Hofstead-Duffy, De-Jun Chen, Shi-Gang Sun, and YuYe J. Tong. Origin of the current peak of negative scan in the cyclic voltammetry of methanol electro-oxidation on Pt-based electrocatalysts: a revisit to the current ratio criterion. Journal of Materials Chemistry, 22(11):5205, 2012.

[117] Mathias Van Thiel, Edwin D. Becker, and George C. Pimentel. Infrared Studies of Hydrogen Bonding of Water by the Matrix Isolation Technique. The Journal of Chemical Physics, 27(2):486, 1957.

[118] John E Parmeter. Copper CVD Chemistry on a Reactive Substrate : $Cu(hfac)_2$ and hfacH on Pt(111). Journal of Physical Chemistry, 97:11530–11541, 1993.

[119] Sariwan Tjandra, Hansheng Guo, and Francisco Zaera. Varied Thermal Chemistry of Hydrocarbons on Nickel Single-Crystal Surfaces. Topics in Catalysis, 54(1-4):26–33, January 2011.

[120] G Ya Popova, T V Andrushkevich, Yu A Chesalov, and E S Stoyanov. In situ FTIR Study of the Adsorption of Formaldehyde, Formic Acid, and Methyl Formiate at the Surface of TiO_2 (Anatase). Kinetics and Catalysis, 41(6):885–891, 2000.

[121] Changbin Zhang, Hong He, and Ken-ichi Tanaka. Catalytic Performance and Mechanism of a Pt/TiO_2 Catalyst for the Oxidation of Formaldehyde at Room Temperature. Applied Catalysis B: Environmental, 65(1-2):37–43, May 2006.

[122] Aaron S. Eppler, Günther Rupprechter, Erik A. Anderson, and Gabor A. Somorjai. Thermal and Chemical Stability and Adhesion Strength of Pt Nanoparticle Arrays Supported on Silica Studied by Transmission Electron Microscopy and Atomic Force Microscopy. The Journal of Physical Chemistry B, 104(31):7286–7292, August 2000.

[123] C Klünker, M Balden, S. Lehwald, and W. Daum. CO Stretching Vibrations On Pt (111) and Pt (110) Studied By Sum- Frequency Generation. Surface Science, 360:104–111, 1996.

[124] Jiazhan Xu and John T. Yates Jr. Terrace Width Effect on Adsorbate Vibrations : a Comparison of Pt(335) and Pt(112) for Chemisorption of CO. Surface Science, 327:193–201, 1995.

[125] Philipp Gruene, André Fielicke, Gerard Meijer, and David M Rayner. The Adsorption of CO on Group 10 (Ni, Pd, Pt) Transition-Metal Clusters. Physical chemistry chemical physics : PCCP, 10(40):6144–9, October 2008.

[126] Sungho Park, Sally a. Wasileski, and Michael J. Weaver. Electrochemical Infrared Characterization of Carbon-Supported Platinum Nanoparticles: A Benchmark Structural Comparison with Single-Crystal Electrodes and High-Nuclearity Carbonyl Clusters. The Journal of Physical Chemistry B, 105(40):9719–9725, October 2001.

[127] Xiangzhi Cui, Limin Guo, Fangming Cui, Qianjun He, and Jianlin Shi. Electrocatalytic Activity and CO Tolerance Properties of Mesostructured Pt/WO_3 Composite as an Anode Catalyst for PEMFCs. Journal of Physical Chemistry C, 113:4134–4138, 2009.

[128] Marie-Isabelle Baraton and Lhadi Merhari. Determination of the Gas Sensing Potentiality of Nanosized Powders by FTIR Spectrometry. Scripta Materialia, 44(8-9):1643–1648, May 2001.

[129] A. H. Kahn. Theory of the Infrared Absorption of Carriers in Germanium and Silicon. Physical Review, 97:1647, 1955.

[130] D. N. Goldstein and S. M. George. Enhancing the Nucleation of Palladium Atomic Layer Deposition on Al_2O_3 Using Trimethylaluminum to Prevent Surface Poisoning by Reaction Products. Applied Physics Letters, 95(14):143106, 2009.

[131] Ji-Fang Fu, Wen-Qi Yu, Xing Dong, Li-Ya Chen, Hai-Sen Jia, Li-Yi Shi, Qing-Dong Zhong, and Wei Deng. Mechanical and Tribological Properties of Natural Rubber Reinforced with Carbon Blacks and Al_2O_3 Nanoparticles. Materials & Design, 49:336–346, August 2013.

[132] Debapriya De, Prabir Kr Panda, Madhusudan Roy, Satyaban Bhunia, and Abu Ismail Jaman. Reinforcing Effect of Nanosilica on the Properties of Natural Rubber / Reclaimed Ground Rubber Tire Vulcanizates. Polymer Engineering and Science, pages 227–237, 2013.

[133] Mir Hamid Reza Ghoreishy, Mohammad Alimardani, Ramin Zafar Mehrabian, and Saeed Taghvaei Gangali. Modeling the Hyperviscoelastic Behavior of a Tire Tread Compound Reinforced by Silica and Carbon Black. Journal of Applied Polymer Science, pages 1725–1731, July 2012.

[134] R. Mujal-Rohas, J. Orrit-Prat, and M. Marin-Genesca. Dielectric, Thermal and Mechanical Properties of Polyamide (PA) Reinforced Tires (GTR). AFINIDAD, 70(561):13–23, 2013.

[135] Oliver Klockmann. Fuel-Saving and Environmentally Safe: Silane VPSi363 - the Formula for Innovative Tire Technology. degussa ScienceNewsletter, 16:4–11, 2006.

[136] M. Shirazi, A. G. Talma, and J. W. M. Noordermeer. Viscoelastic Properties of Short Aramid Fibers-Reinforced Rubbers. Journal of Applied Polymer Science, 128(4):2255–2261, May 2013.

[137] F. D. Osterholtz and E. R. Pohl. Kinetics of the Hydrolysis and Condensation of Organofunctional Alkoxysilanes: a Review. Journal of Adhesion Science and Technology, 6(1):127–149, 1992.

[138] Paula Puomi and Heidi M Fagerholm. Characterization of Hot-Dip Galvanized (HDG) Steel Treated with gamma-UPS , VS, and Tetrasulfide. Journal of Adhesion Science and Technology, 15(5):509–533, 2001.